MODELING AND SIMULATION OF THE FLIGHT DYNAMICS OF MORPHING WING AIRCRAFT

by

BORNA OBRADOVIC

Presented to the Faculty of the Graduate School of

The University of Texas at Arlington in Partial Fulfillment

of the Requirements

for the Degree of

MASTER OF SCIENCE IN AEROSPACE ENGINEERING

THE UNIVERSITY OF TEXAS AT ARLINGTON

December 2009

To my wife Ashie, without whose love and support the realization of this dream would not have been possible.

ACKNOWLEDGEMENTS

I would like to thank my Advisor, Prof. Kamesh Subbarao, for his support and guidance, and very useful discussions. I would also like to thank my wife Ashie for her infinite patience and care in editing this manuscript, as well as the much appreciated support and encouragement.

November 3, 2009

ABSTRACT

MODELING AND SIMULATION OF THE FLIGHT DYNAMICS OF MORPHING WING AIRCRAFT

BORNA OBRADOVIC, M.S.

The University of Texas at Arlington, 2009

Supervising Professor: Kamesh Subbarao

Aircraft with variable wing geometry (morphable wings) are of considerable interest, not only for mission-specific optimization, but for enhanced maneuverability as well. In the nascent field of mini- or micro-Unmanned Aerial Vehicles (UAVs), large and rapid changes in wing geometry are achievable, resulting in significant changes of the dynamics of the vehicle. In this thesis, we present a simulation methodology suitable for such aircraft, accounting for the changes in both the aerodynamic and inertial properties. Due to the complexity of the possible wing configurations, the aerodynamics are simulated using an unsteady Vortex-Lattice approach, solved concurrently with six(+) degrees of freedom (DOF) nonlinear equations of motion. The time dependence of the inertia tensor and motion of mass within the body frame are explicitly taken into account, resulting in additional body frame forces and moments. The simulation methodology is applied to several morphing wing configurations. The aerodynamic loads of each configuration are obtained and the flight dynamics analyzed through non-linear simulation.

TABLE OF CONTENTS

LIST OF FIGURES

LIST OF TABLES

NOMENCLATURE

$\mathbf{F}$	Net force acting on aircraft
$\mathbf{F_{acm}}$	Morphing force associated with CM acceleration
$\mathbf{F_{vcm}}$	Morphing force associated with Coriolis force
$\mathbf{F}_{\dot{\omega}}$	Morphing force associated with transverse
$\mathbf{F}_{\omega\omega}$	Morphing force associated with centrifugal force
Φ	Total velocity potential
Φ_∞	Freestream velocity potential
ϕ_i	Velocity potential induced by i-th panel
Γ_i	Induced vorticity of i-th vortex lattice element
$[\mathbf{H_i}]$	Hessian matrix of i-th panel center w.r.t. morphing variables
$\mathbf{h}$	Angular momentum of aircraft
$[\boldsymbol{J}]$	Moment of inertia tensor
$\boldsymbol{\tau_{ext}}$	Total external moment acting on aircraft
m	Mass of aircraft
$\mathbf{M}_j$	Morphing moment j ($j \in \{1, 4\}$)
$\hat{\mathbf{n}}_i$	Normal vector of the i-th panel
$\boldsymbol{\omega}$	Angular velocity of body frame w.r.t the inertial frame
$[\tilde{\boldsymbol{\omega}}]$	Skew-symmetric matrix representation of $\boldsymbol{\omega}$
P^j	Generalized momentum associated with j-th actuator
Q_{CM}	Gnerealized actuator moment associated with CM motion
Q_{Panels}	Generalized actuator moment associated with panel motion
$Q_{CM-Rate}$	Generalized actuator moment associated with rate of CM motion

$Q_{Panels-Rate}$	Generalized actuator moment associated with rate of panel motion
q_i	Morphing variable associated with the i-th actuator
Q^j	Generalized force associated with j-th actuator
$\mathbf{r}$	Position of a mass element within the body frame
$\tilde{\boldsymbol{r}}$	Skew-symmetric matrix representation of r
$\mathbf{r_{cm}}$	Position of aircraft CM within body frame
$\mathbf{R_f}$	Position of body-frame origin w.r.t. inertial frame
$\mathbf{R_{cm}}$	Position of aircraft CM w.r.t. inertial frame
ρ	Mass density (of air, or aircraft, depending on context)
$\boldsymbol{\Delta r_{cm}}$	Displacement of aircraft center of mass from body frame origin
$\mathbf{V_f}$	Velocity of origin of aircraft body frame
$\mathbf{v}'$	Velocity of a mass element in the body frame (body-frame derivative of r)
$\mathbf{x}_i$	Position of center of i-th aircraft panel in body frame

CHAPTER 1

INTRODUCTION

Variable wing geometry aircraft have been in regular use since the 1970s, and examples of attempts at morphable wings go back to the pre-WWII era [1]. The goal of wing morphing was primarily mission-specific optimization of aerodynamic performance. "Swing-wings" were used to provide high L/D ratio in the unswept position for low-speed takeoff and landing and to reduce drag at high speed cruise in the swept-back position. More recently, there has been considerable interest in the use of rapidly morphing wings for the purpose of enhanced maneuverability. This implies rapid motion of large sections of the wing. While this may be difficult to achieve for large aircraft, it is quite feasible for mini- or micro-Unmanned Aerial Vehicles (UAVs). Greatly enhanced maneuverability has been demonstrated for morphable wing UAVs [2, 3], and roll rates in excess of 360 deg/s have been achieved. [2] Furthermore, research is being conducted into the utility of bio-mimetic flight for micro-UAVs [4].

1.1 Technical Detail

From a theoretical and computational analysis standpoint, large and rapid changes of the wing geometry present some unique challenges. Firstly, the number of Degrees Of Freedom (DOF) which strongly influence the aerodynamics is increased, possibly greatly (depending on the complexity of the wing). This in turn implies that pre-computing aerodynamic derivatives becomes combinatorially prohibitive; the dimensionality of the configuration space is potentially high (must take into account deflections of all parts of the wing), and interactions cannot be a priori neglected

due to large deflections. The full lookup-table of derivatives would need to be recomputed for any change in the aircraft structure. This suggests that computing the aerodynamic forces during the flight simulation itself may be preferable.

Secondly, the large motions of the wing segments make the rigid-body approximation of the aircraft inadequate. In a frame fixed to a predetermined point on the aircraft, both the inertia tensor and center of mass (CM) will be functions of time. This must be taken into account in the equations of motion. Furthermore, the standard Newton-Euler equations of motion for a rigid body require modification for a morphing body. Alternatively, the aircraft can be treated as a multi-body system, with each movable segment being represented by a rigid body [5, 6]. Such approaches, while more detailed, add significant computational cost and complexity.

Lastly, since high maneuverability is the goal, unsteady aerodynamic effects must also be addressed. Specifically, the within-body frame motion of the wings, as well as the rotational velocity of the body frame itself, must be modeled [7].

In this paper, a simulation methodology well suited to handle the aforementioned challenges is presented. A general-purpose, unsteady Vortex-Lattice aerodynamics simulator is developed and coupled to the transient simulation of a six(+) DOF aircraft. Equations of motion fully taking morphing into account are developed. Simulations are then performed with several different morphable-wing aircraft configurations, and results are analyzed.

1.2 Literature Survey

The subject of dynamics and control of morphing aircraft has received considerable attention in the literature. This is particularly true in the last several years, as the notion of morphing has been applied to UAVs. The effect of morphing on the dynamics is studied in [8, 9, 10, 11]. Simplified flight dynamics are used, ignoring terms

deemed to be of 2^{nd} order (but shown in this work to be quite significant under certain conditions). The additional terms introduced in the literature are typically just the time derivatives of the inertia tensor components. In [9, 11] the morphing inputs are assumed to directly modify the inertia tensor. Linearization of the dynamics then results in an LTV system, the stability properties of which are further examined in [8]. A more complete dynamical model is formulated by [12]; the equations of motion are re-derived with the assumption of morphing, resulting in additional terms (beyond the time derivatives of the inertia tensor). However, the development is restricted to symmetric and/or purely longitudinal morphing, which allows the authors to omit otherwise significant terms. A subset of morphing strategies confined (primarily) to airfoil shape is also studied by [13]. The morphing flight dynamics are limited to the time derivatives of the inertia tensor. The dynamics of morphing is also studied in the context of multi-body dynamics [14]. Using constrained-dynamics software ADAMS [15], a rigorous simulation of symmetric (and slow) gull-wing morphing is obtained. While accurate, the multi-body approach does not result in particularly insightful analytic expressions describing morphing.

The subject of aerodynamics and airflow for morphing aircraft has also been studied by several groups. Various panel approaches have been used [13, 16, 17], demonstrating the applicability of the method. Also shown [16] is that there is relatively little improvement in accuracy to be had by utilizing fully unsteady lattice methods (as opposed to using a quasi-stationary vortex lattice our doublet lattice), except for in special circumstances (such as helicopter rotors). Lattice methods are shown to be significantly more predictive than lifting-line theory, however. This has important implications on the choice of method when attempting to balance accuracy and computational efficiency. Efforts to leverage full Navier-Stokes CFD for morph-

ing aircraft simulation are far more limited, due to the obvious computational effort involved. Nevertheless, the unsteady aerodynamics of morphing are studied by [18].

Finally, the subject of morphing actuator power consumption seems to have received relatively little attention. Notable exceptions are [19] and [20]. The discussion is limited to airfoil morphing and the associated power, however.

1.3 Contributions

The major contributions of this work can be summarized as follows:

1. **Formulation of Extended Rigid-Body Dynamics:** An approach is developed for modeling the dynamics of arbitrarily morphing structures, without having to resort to the full machinery of one of the flavors of Multi-Body Dynamics. No constraints are placed on the type of morphing. While a number of authors have made similar contributions, the published approaches have been either specialized to a particular aircraft configuration or limited to single morphing degree of freedom, to longitudinal morphing, or purely symmetric morphing. The general treatment incurs some implementation challenges that are elaborated upon in this thesis, but the result is computationally efficient and generally applicable.
2. **Formulation of a general approach for computing the dynamic loads and power associated with morphing actuation:** A formulation is presented of the moments and power required of the actuators in order to execute desired morphing maneuvers. The formulation takes into account aerodynamic, inertial, and morphing loads on the aircraft joints. Moreover, the formulation can be used for determining dynamic joint moments of non-morphing aircraft as well.

3. **Vortex-Lattice Aerodynamics C++ Implementation suitable for morphing aircraft:** A Vortex-Lattice code has been developed for efficient computation of aerodynamic forces and moments on a morphing aircraft. In addition to the usual wind-frame variables, the code takes into account the angular velocity of the aircraft (resulting in aerodynamic damping), as well as the velocities of the various panels which comprise the aircraft. Careful attention is paid to computational efficiency, enabling the re-evaluation of the flow-field at every timestep of non-linear simulation.
4. **MATLAB Class Library for creation and simulation of arbitrary morphing aircraft:** A MATLAB class library has been developed, including classes for the creation and manipulation of morphing aircraft models, MEX-interface to Vortex-Lattice Aerodynamics, non-linear solvers and post-processing. The library is structured for maximum flexibility, allowing the creation of nearly arbitrary aircraft models. The models consist of planforms and three-dimensional bodies, interconnected by actuated joints.
5. **Full non-linear simulation of morphing-induced turn maneuvers**. Using a morphing gull-wing aircraft as the test vehicle, the possibility of asymmetric morphing-induced maneuvering is investigated through simulation. The effect of rapid morphing is investigated, as well as the power requirements for the various morphing actuators

CHAPTER 2

SIMULATION STRUCTURE AND MODEL COMPONENTS

2.1 Goal and Scope of Morphing Aircraft Simulation

The overall goal of this work is to create a simulation framework for morphing aircraft, useful for studying the flight dynamics of various configurations, as well as for the design of suitable control systems. Specifically, the simulation framework needs to satisfy the following set of requirements:

1. **Straightforward creation of arbitrary morphing aircraft structures**, as defined by a set of planforms and additional objects characterized by their inertia tensor and spatial placement.
2. **Automatic calculation of aerodynamic forces** for any given morphing configuration and flight condition, with reasonable accuracy.
3. **Accurate flight dynamics, including morphing dynamics effects**. Morphing is not assumed to be small (perturbation), nor is it assumed to be quasi-static.
4. **Non-linear flight simulation capability.** Equations of motions need to be integrated with controlled precision and best possible CPU efficiency.
5. **Calculation of actuator joint moments and power.** The moments and power required for each actuator must be computed automatically, accounting for aerodynamic, inertial, and morphing forces.
6. **Automated trimming and creation of linearized system around trim point.** The A, B, and C system matrices should be generated at an arbitrary

trim point. The required control inputs for establishing the trim point must be computed automatically.

7. **Integration with MATLAB** for aircraft definition input, control system definition, and post-processing.
8. **Reasonable CPU efficiency.** Non-linear flight simulation should take place in near real-time or faster.
9. **Simple extensibility and customizability.** Adding a new aircraft type should not require any modifications in the core code.

The requirements are somewhat self-contradictory, with simultaneous goals of accuracy, generality, and CPU efficiency. Meeting all the criteria requires careful tradeoffs which are discussed in subsequent sections.

2.2 Simulation Software Structure

The simulation software structure is illustrated in Fig. 2.1. The simulation framework is implemented as a MATLAB class library, with Vortex-Lattice Aerodynamics and geometry morphing implemented in C++ for CPU efficiency. The class library is set up to (as much as possible) simplify the creation of new, user-defined components. Specifically, users will frequently define a new aircraft or a new set of control inputs or observed outputs. Thus, base classes are provided for objects of type Aircraft, inputControl, and outputFunctor. Creating a new implementation simply requires the derivation of a new class from the base class, which provides the required interface to the overall class library. It is therefore not required that the user be familiar with the details of the overall code implementation. The overall class hierarchy is illustrated in Fig. 2.1. The dark blue boxes represent modules which need to be created by the user. This includes a custom aircraft definition (derived

from an Aircraft base-class), and the top-level driver script, which invokes the desired simulations. The implementation is a combination of compiled C++ and MATLAB.

An aircraft model is defined by a set of planforms, additional (non-planform) masses, and morphing joints. The inertia properties of planforms are computed automatically. Additional masses require explicit input regarding the inertia tensor, CM, and placement. All coordinates are w.r.t. a conventional body frame coordinate system [21, 22], with the x-axis aligned with the nose of the aircraft, the y-axis pointing to the right, and the z-axis pointing downward. The morphing actuators are each defined by the axis of rotation, an anchor point, and the panels (or other bodies) that they are attached to. Additionally, the actuator frequency and damping ratio must be defined (described in more detail in section 4.2). Each actuator induces two state variables (the displacement and rate of displacement) and one control variable (commanded displacement). The definition of an aircraft model is illustrated next on the gull-wing aircraft example.

2.3 Gull-wing Aircraft Example

A simple aircraft model with gull-wing morphing is used for testing and validation of the simulation code. The aircraft (in different wing configurations) is illustrated in Figs. **??** through 2.4. An "exploded" view, depicting the individual planforms and actuators, is depicted in Fig. 2.5. In Fig. 2.5, the blue rotational arrows denote actuators (inducing state and control variables), whereas the red rotational arrows denote one-time rotations only. Additionally, shift and mirror operations are provided in order to simplify model creation.

The aircraft has two rotating joints per wing; the first attaches the wing root to the fuselage, while the second allows the wing to bend at the half-span point. As is discussed in sections 5.2.1 and 5.3.1, wing morphing can modulate both lift and

Table 2.1. Gull-wing aircraft basic properties

Length	$2\ m$
Wingspan	$2\ m$
Area	$0.87\ cm^2$
Mass	$50\ kg$
I_{xx}	$10\ kg\ m^2$
I_{yy}	$17\ kg\ m^2$
I_{zz}	$11\ kg\ m^2$
I_{xz}	$-1.8\ kg\ m^2$
Mach Number (cruise)	$0.2 - 0.25$

the roll moment, replacing the more traditional flaps and ailerons. Pitch and yaw moments are mostly generated by the ruddervons located at the back of the aircraft. The rotation of the ruddervons is treated as morphing, even though it has only minor impact on the inertia properties. The basic properties of the aircraft are summarized in Table 2.1.

The gull-wing aircraft will be used for most of the subsequent simulation test-cases (except where comparing to known data or simulation results in section 3.2.4).

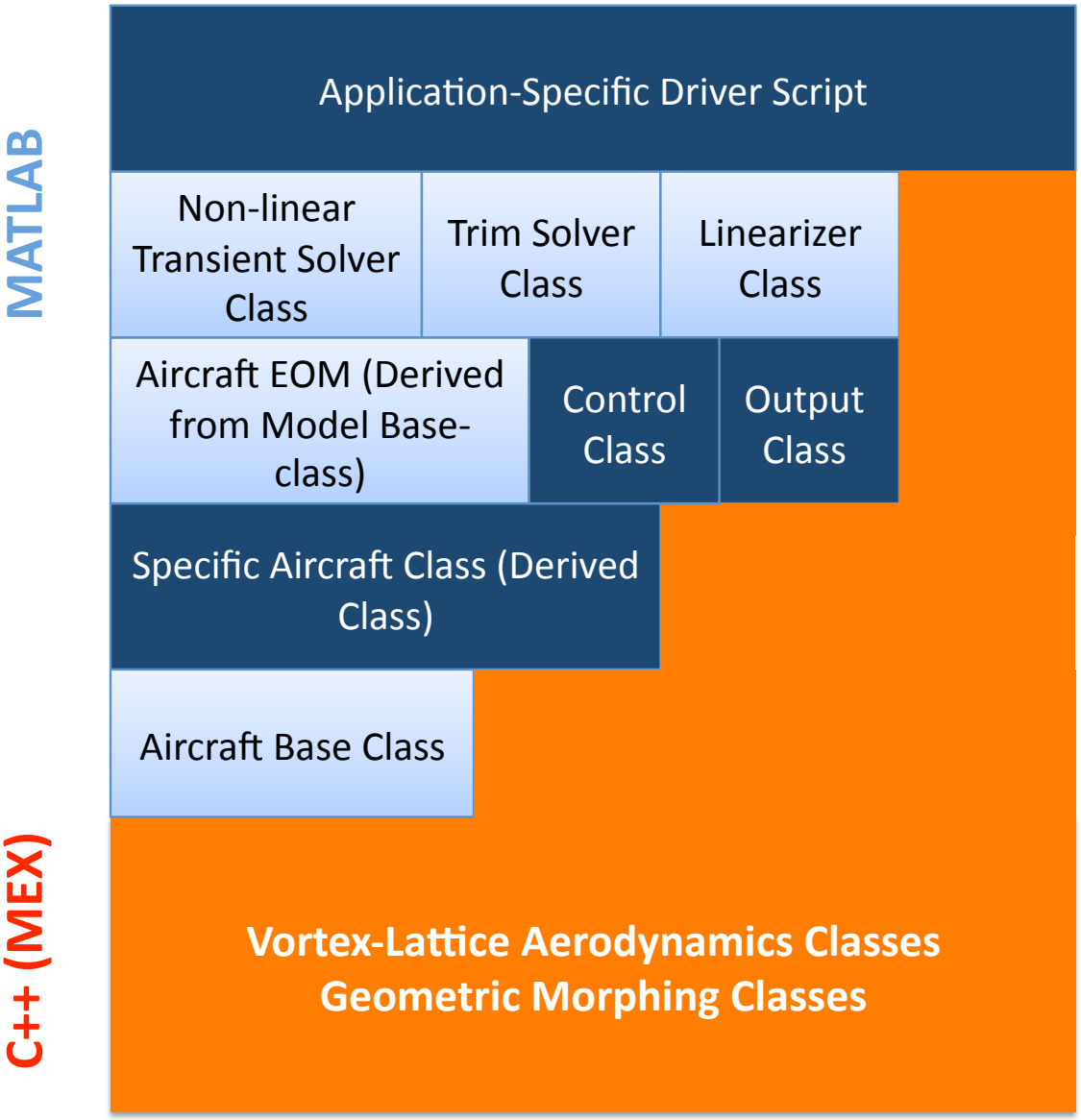

Figure 2.1. Software structure of the morphing aircraft simulation code.

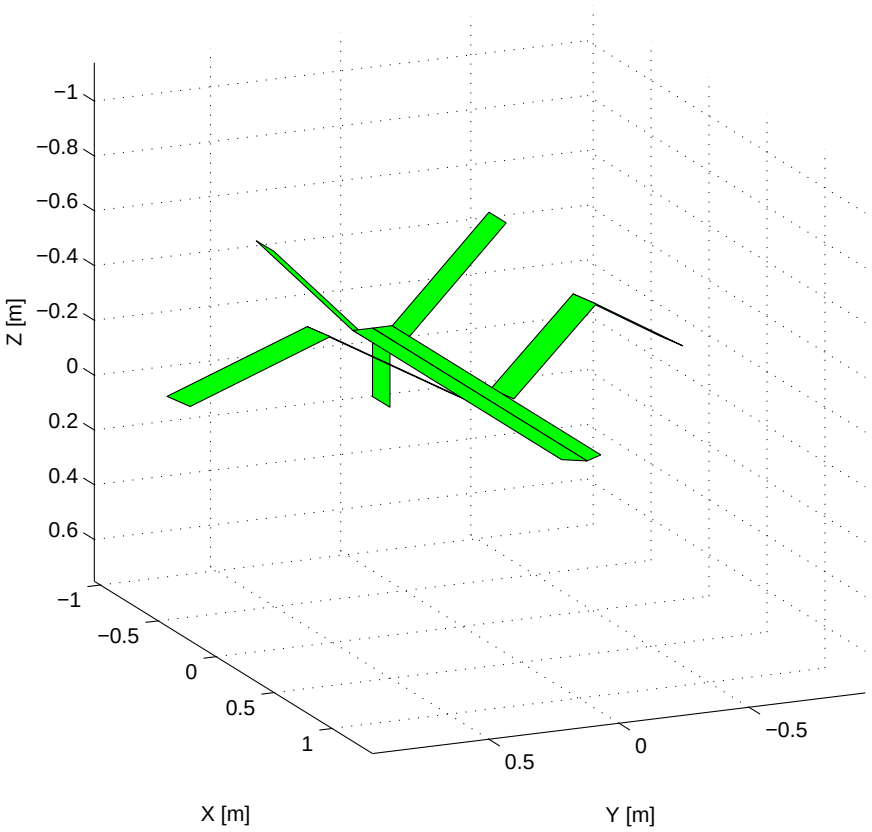

Figure 2.2. Test aircraft in the symmetric gull-wing configuration.

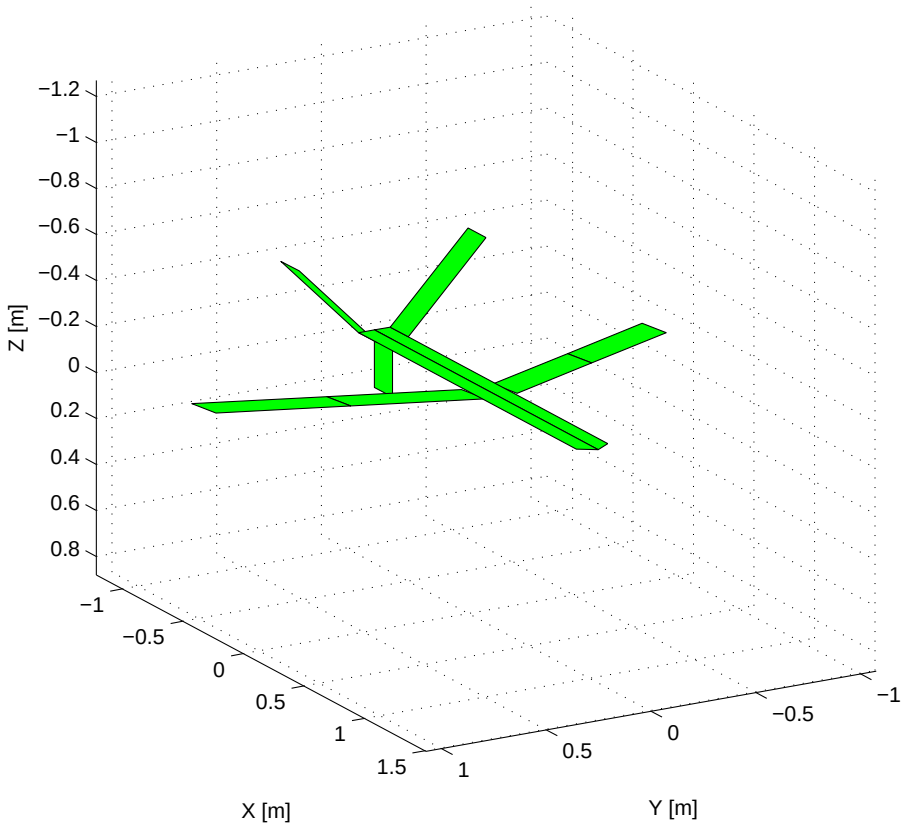

Figure 2.3. Test aircraft in the flat-wing configuration.

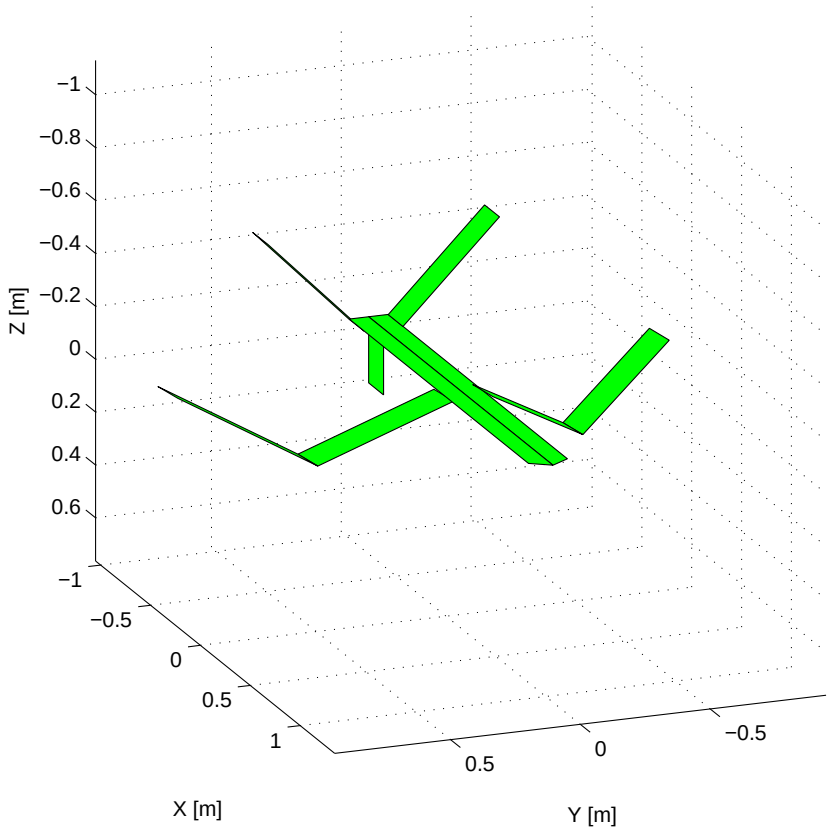

Figure 2.4. Test aircraft in the inverted gull-wing configuration.

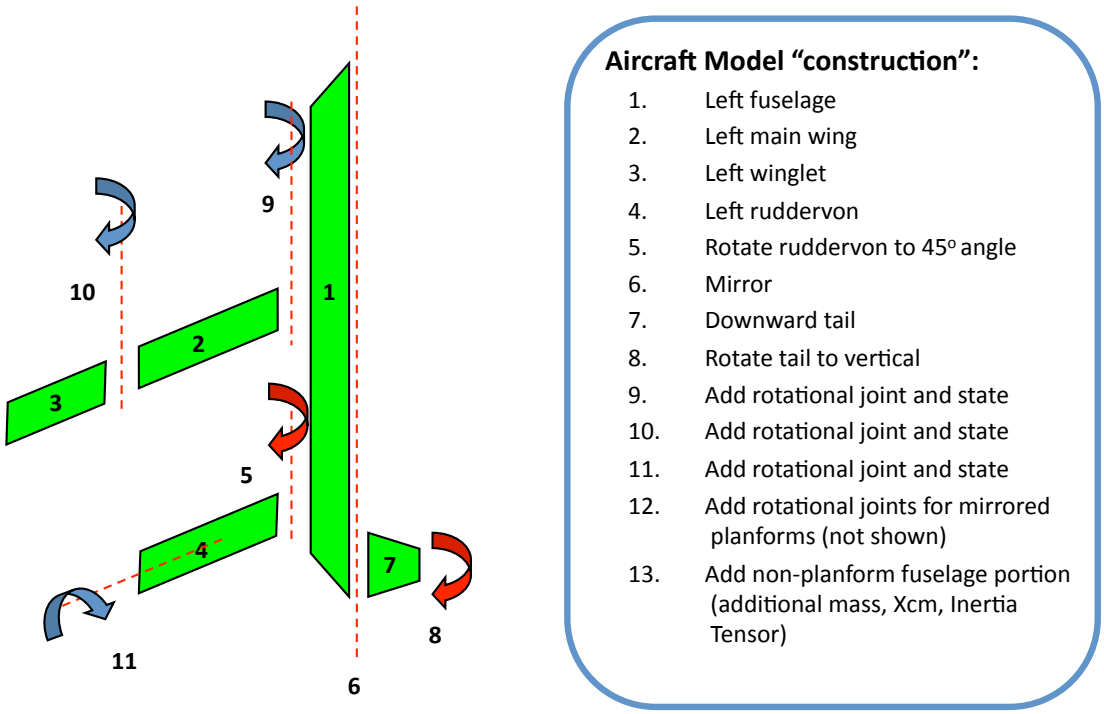

Figure 2.5. Components and "construction" of an aircraft model.

CHAPTER 3

MODELING OF AERODYNAMICS

An accurate aerodynamic model is an essential component for successful flight simulation. This is particularly true for a morphing aircraft, for which the aerodynamic forces are unexplored and may vary significantly from configuration to configuration. Thus, the method of choice must be as predictive as possible. A high degree of fidelity in aerodynamic computation is contrary to the requirement of efficient simulation, however. Since we are interested in simulating the full, non-linear dynamics of an aircraft in flight, the aerodynamic calculations will be repeated at each timestep of the simulation, possibly resulting in unacceptable simulation times. The various options must be carefully considered.

3.1 Modeling Approaches

The simplest modeling approach is to construct an analytical model of the aircraft, utilizing lift, drag, and moment coefficients to describe the aerodynamic forces and moments. This approach results in the shortest possible simulation times, since model evaluation is quite straightforward. However, we are still faced with the task of determining the correct values of the various coefficients. These can be obtained either from wind-tunnel simulation, or from a solution to the Navier-Stokes fluid flow equations, using the methods of Computational Fluid Dynamics (CFD). If we are interested in non-linear simulation (i.e., the aircraft state departs significantly from the trim point), it will be necessary to construct a lookup table of the coefficients to represent all anticipated flight conditions. This is the commonly

adopted approach for the simulation of rigid aircraft. The required lookup tables are large, but manageable.

For morphing aircraft, however, the lookup table tends to be considerably larger. This is because of the required inclusion of additional variables which describe the morphing state of the aircraft. The number of morphing variables may be large (depending on the aircraft), and the aerodynamic forces may be quite sensitive to the morphing state. This requires the tabulation to be quite fine w.r.t. the morphing variables, resulting in a "combinatorial explosion" of the size of the lookup table. The particular aircraft used as an example in this work has six morphing variables, each of which must be discretized to approximately ten levels. These states are in addition to any that the rigid aircraft would have; thus, the size of the table increases by a factor of $\approx 10^6$ relative to the rigid body case.

The task of generating such a table is daunting and quite wasteful, since it results in the computation of a large number of states which are never actually visited by any one simulation. It is therefore attractive to compute the aerodynamic forces "on-the-fly," rather than pre-computing and tabulating all possible configurations. Time constraints then rule out the use of CFD (unless very significant computing resources are available). This leaves the possibility of using a lattice method (such as the Vortex-Lattice Method, or the Doublet-Lattice method) for modeling potential flow. Lattice methods are computationally efficient (relative to full CFD) and yield reasonably accurate solutions for a restricted class of flows. The primary restrictions are those of incompressibility and low viscosity. In this work, the Vortex-Lattice Method [7, 23] is adopted for computing the flow-field and the aerodynamic forces and moments.

3.2 Vortex-Lattice Model

The Vortex-Lattice model is a numerical solution to the laminar flow problem, i.e., a flow described by a potential function. The flow is assumed to be incompressible, irrotational (except at singular points on the surface of the aircraft), and non-viscous. As such, it is applicable to low Mach number ($M < 0.3$) flows at small angles of attack. Since the flow is irrotational, it can be described by a potential function as follows:

$$\mathbf{V} = \nabla\Phi \tag{3.1}$$

Applying Eq. (3.1) to the steady-state continuity equation (with constant density) yields the equation for steady potential flow:

$$\nabla^2\Phi = 0 \tag{3.2}$$

The flow equation (Eq. (3.2)) itself does not completely describe the flow; the boundary conditions of the problem must also be specified. For an aircraft flow problem, the required boundary condition is obtained by stipulating the "no-penetration-condition" of Eq. (3.3), i.e., the air must flow around, and not through, the aircraft. Far from the aircraft, the freestream conditions are assumed to persist.

$$\hat{\mathbf{n}} \cdot \nabla\Phi = 0 \tag{3.3}$$

The symbol $\hat{n}$ in Eq. (3.3) signifies the local surface normal vector on the aircraft. Thus, Eq. (3.3) requires that the flow immediately adjacent to the aircraft be parallel to the surface.

The basic idea of lattice methods is to obtain a solution to Eq. (3.2) while satisfying the non-penetration condition of Eq. (3.3) by composing the solution as a superposition of the unperturbed free-stream potential and the potential arising from a finite set of discrete source. The sources are chosen to satisfy the Laplace equation (Eq. (3.2)), and are typically singularity elements, such as vortices or doublets.

The overall solution is then a superposition of the free-stream potential and a linear combination of the discrete source potentials. The values of the coefficients in the linear combination can then be determined by asserting the condition of Eq. (3.3) on a finite set of collocation points (typically referred to as control points) on the surface of the aircraft, and solving the resulting system of equations. The form of the solution is then given by:

$$\Phi(\mathbf{x}) = \sum_i \Gamma_i \phi_i(\mathbf{x}, \mathbf{x_i}) + \Phi_\infty \tag{3.4}$$

where Φ represents the computed flow potential, and ϕ is the potential of the i-th singlarity element. Also, x represents the evaluation point for the potential, while x_i is the location of the i-th singularity element. The weighting coefficients to be determined are represented by Γ_i. Inserting Eq. (3.4) into Eq. (3.3), a system of linear equations is obtained:

$$\sum_j \left(\hat{\mathbf{n}}_i \cdot \nabla \phi_j\right) \Gamma_j = -\hat{\mathbf{n}}_i \cdot \nabla \Phi_\infty \tag{3.5}$$

As it stands, Eq. (3.5) is useful for quasi-static flows only. The flow velocity terms do not take into account the fact that the freestream velocity is different at different control points of the aircraft. These differences arise due to the rotational and morphing motions. For example, as the aircraft rolls, the freestream velocity experienced by the falling wing will be higher than that experienced by the rising wing. Likewise, the local angle of attack will shift. Similarly, if the aircraft morphs, and the planforms move within the body frame, the moving planforms will experience a modified freestream velocity. This can be taken into account by modifying the non-penetration condition as follows:

$$\hat{\mathbf{n}}_i \cdot \left(\nabla \Phi + \nabla \Phi_\infty + [\tilde{\boldsymbol{\omega}}] \boldsymbol{r_i} + \mathbf{v}_i\right) = 0 \tag{3.6}$$

The value of ω in Eq. (3.6) is assumed to be an input to the vortex-lattice code. The positions and velocities of the panels $\mathbf{r}_i$ and $\mathbf{v}_i$ are also assumed to be computed elsewhere (discussed in Section 4.2) and provided as input to the vortex-lattice module. The complete system of equations used for Vortex-Lattice calculations in this work is then:

$$\sum_j \left(\hat{\mathbf{n}}_i \cdot \nabla\phi_j\right)\Gamma_j = -\hat{\mathbf{n}}_i \cdot \left(\nabla\Phi_\infty + [\boldsymbol{\omega}]\boldsymbol{r_i} + \mathbf{v}_i\right) \tag{3.7}$$

For a given set of singularity functions $\{\phi\}$, a given set of control points $\{x\}$, and specific freestream conditions, the only unknowns in Eq. (3.7) are the weighting coefficients $\{\Gamma\}$. Equation (3.7) can then be solved for the weighting coefficients. Clearly, the number of control points must be equal to the number of singularity elements for the system to be solvable. It is also clear that the choice and placement of the singularity elements is a matter of modeling. In addition to the surface of the aircraft, the singularity elements are also placed on the vortex wake trailing the aircraft. The vortex wake would not have been predicted by Eq. (3.2), but it is known to exist, and can be modeled reasonably well by a sheet of singular source.

The various lattice methods differ in the choice of singularity elements and the details of the treatment of the vortex wake. The particular choices made in this work are described next.

3.2.1 Singularity Elements

The singularity elements chosen for this work are the horseshoe-vortex elements, illustrated in Fig. 3.1. Each horseshoe element consists of three vortex-line segments: the "head," and two "tails" [7].

The elements are placed on the surface of the aircraft as shown in Fig. 3.2. Each horseshoe vortex contributes one control point and a single undetermined vortex

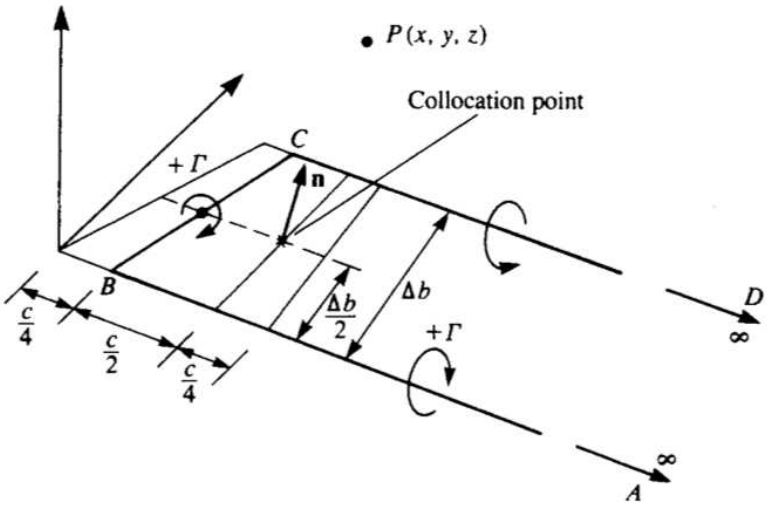

Figure 3.1. Single "horseshoe" vortex element.

strength. The vortex wake is automatically constructed from the tails of the horseshoe vortices.

The velocity (gradient of flow potential, in Eq. (3.5)) induced by each differential element can be computed using the Biot-Savart Law:

$$\mathbf{dV} = -\frac{\Gamma[\tilde{\mathbf{r}}]\mathbf{dl}}{4\pi||\mathbf{r}||^3} \tag{3.8}$$

The contribution of a finite-length vortex line is obtained by integration, as shown in [7, 23]. If the vector representing the vortex line is labelled as $\mathbf{r}_o$, and the vectors from the ends of the vortex line to the evaluation point are labelled as $\mathbf{r}_1$ and $\mathbf{r}_2$ (illustrated in Fig. 3.1), the flow velocity contribution of the vortex line can be expressed as [7, 23]:

$$\mathbf{V} = \frac{\Gamma}{4\pi}\frac{[\tilde{\mathbf{r}}_1]\mathbf{r}_2}{||[\tilde{\mathbf{r}}_1]\mathbf{r}_2||^2}\left[\mathbf{r}_o \cdot \left(\frac{\mathbf{r}_1}{||\mathbf{r}_1||} - \frac{\mathbf{r}_2}{||\mathbf{r}_2||}\right)\right] \tag{3.9}$$

Finally, the velocity contribution of the complete horseshoe element in Eq. (3.5) is obtained by superposition of the head and the two tail elements. The length of the

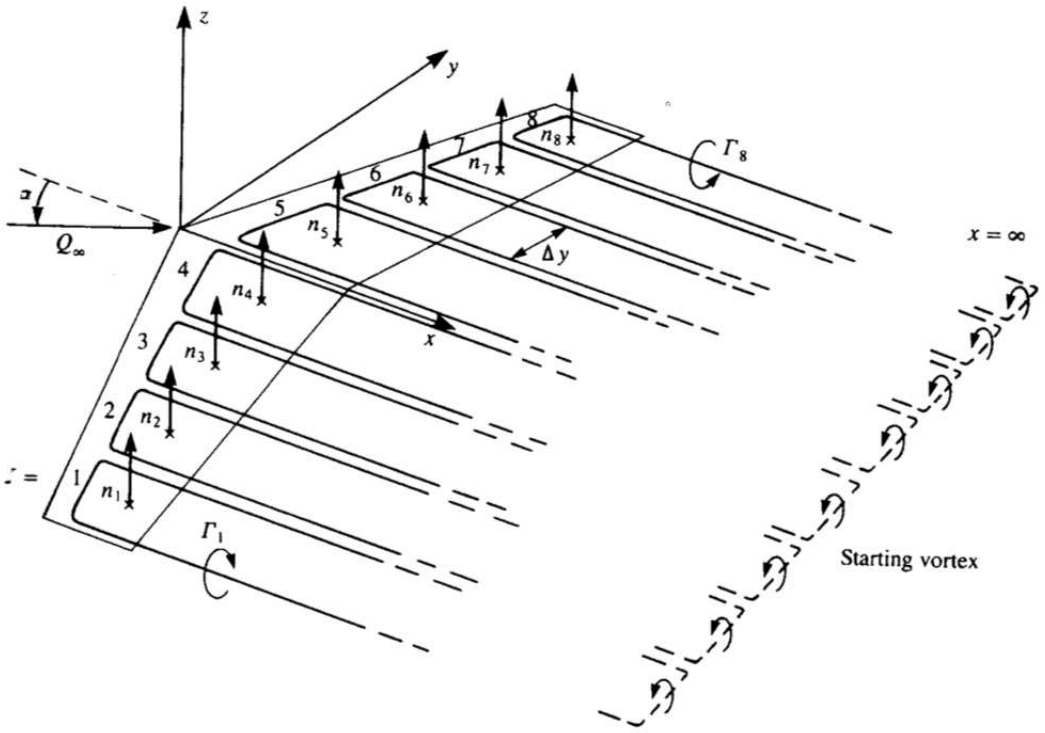

Figure 3.2. Example of "horseshoe" element lattice.

tail is theoretically infinite, but as a practical choice, a tail length equal to $20x$ of the largest aircraft dimension is used.

3.2.2 Calculation of Forces and Moments

Forces and moments on the panels, planforms, and complete aircraft are computed by a summation of the Lorentz force across all the panels. Thus, we have:

$$\mathbf{F} = \sum_i \rho[\tilde{\mathbf{V}}_\mathbf{i}]\mathbf{\Gamma}_i \tag{3.10}$$

$$\tau_{\mathbf{aero}} = \sum_i \rho[\tilde{\mathbf{r}}_i]\big([\tilde{\mathbf{r}}_\mathbf{i}]\mathbf{\Gamma}_i\big) \tag{3.11}$$

where $\vec{r_i}$ is the position vector of the i-th panel (relative to the origin of the body coordinate system), and $\vec{V_i}$ is the airstream velocity at the i-th control point. The

direct method used here requires more computation than methods based on vorticity or flowfield alone, but it provides more detailed information about the distribution of the aerodynamic loads and three-dimensional forces and moments.

3.2.3 Computational Considerations

Since the computation of forces and moments by the Vortex-Lattice method is to be performed at every timestep of the simulation, it is to be expected that a significant computational overhead may be incurred. Several opportunities present themselves to minimize this expense. The first is to simply minimize the required number of re-computations of the linear system in Eq. (3.7). It can be seen in Eq. (3.7) that the influence coefficient matrix $[\mathbf{C}]_{ij} = (\hat{\mathbf{n}}_i \cdot \nabla\phi_j)$ depends only on the geometric placement of the singularity elements and not on the flight conditions. Thus, if the aircraft is not morphing, the matrix does not need to be re-computed. Furthermore, the linear system is solved using LU factorization; if the matrix is not changing, the LU factorization can be preserved. Thus, re-solving the system with a new RHS is performed through simple back-substitution. Given that the majority of the CPU time required to solve a linear system is LU factorization, being able to use back-substitution only provides significant time savings. Under the non-morphing assumption then, only the RHS of Eq. (3.7) must be computed at each timestep, since it explicitly depends on the flight variables. The bulk of the computational cost is due to the assembly of the coefficient matrix and linear solve, however, with the computation time increasing with the square of the number of elements (unlike the RHS, for which assembly time scales linearly with the number of elements). Thus, very significant CPU-time savings are obtained by re-computing the coefficient matrix only when necessary. Since the goal is to simulate a morphing aircraft, however, it is occasionally necessary to re-compute and re-factor the coefficient matrix. A

cumulative "morphing magnitude" criterion is used to determine when the structure has changed sufficiently to require re-assembly of the influence matrix. A suitable criterion is established using a least-squares index of the form:

$$E_{morph} = \sum_i (q_i - q_i')^2 \tag{3.12}$$

In Eq. (3.12), q_i and q_i' represent the i-th morphing state variable and its reference value, respectively. The reference value is simply the value of the state variable the last time that the coefficient matrix was assembled. When the morphing index M exceeds a user-defined tolerance, the matrix is re-assembled, and the reference state is set to the current morphing state. A timing analysis is presented in Chapter 5.

Another key determinant of the required CPU time is the number of lattice elements. As previously mentioned, the influence matrix assembly time scales with the square of the number of elements, while a number of other calculations scale linearly. Thus, minimizing the number of lattice elements will clearly have a significant impact on the simulation time. On the other hand, the accuracy of the solution will likewise depend strongly on the spacing in the lattice mesh. In order to satisfy the contradictory requirements of minimal CPU time and accuracy, the vortex distribution is discretized on a non-uniform tensor mesh, with a mesh assigned to each planform. The use of the non-uniform mesh is particularly important for the induced drag, which is very sensitive to the vorticity distribution near the leading edge of a wing. The non-uniform meshing algorithm begins by partitioning polygonal planforms into trapezoids. The spanwise-direction of the mesh is uniform, whereas the chordwise-direction is highly non-uniform. The trailing half of the wing, where the vorticity is expected to be weak and slowly varying, has a uniform and sparse mesh. A geometrically contracting mesh with a constant ratio is used in the leading half of the planform. The smallest and largest mesh spacing is user-defined. In order

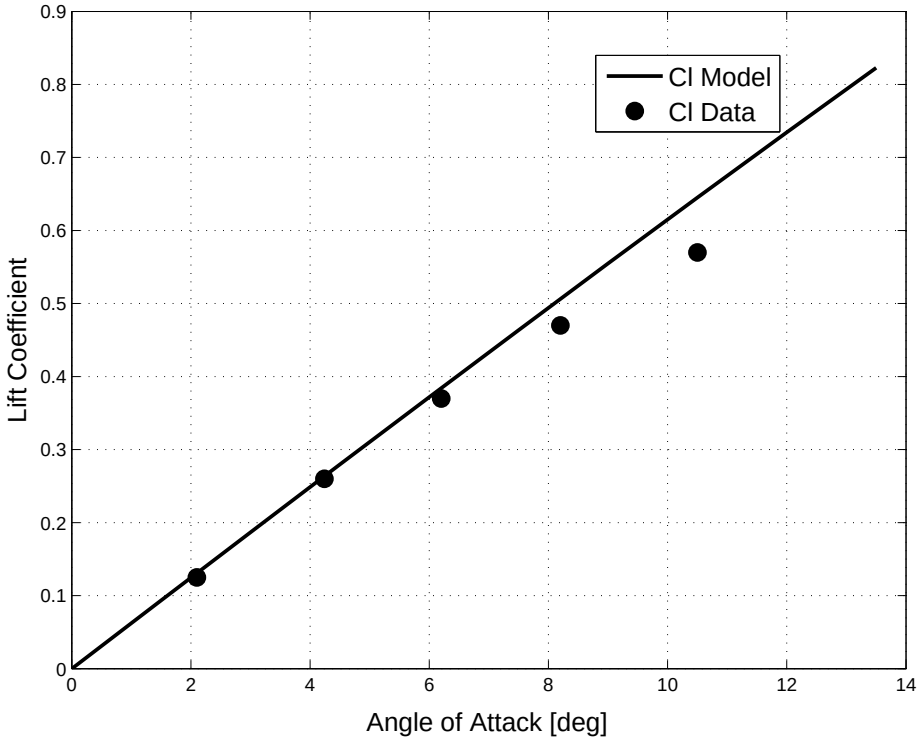

Figure 3.3. VLM-computed lift coefficient for swept wing.

to prevent the VLM system from becoming ill-conditioned, the geometric contraction ratio is not allowed to exceed 1.4.

3.2.4 Validation

Numerous studies of Vortex-Lattice validity under various flight conditions and planform shapes have been published [7, 23, 24, 25, 16, 17]. We have compared the Vortex-Lattice code developed for our work to a number of published results, both experimental and Vortex-Lattice based. In general, excellent agreement is found in comparisons to other codes. Very good agreement is also found w.r.t available data. The data is usually in terms of lift and drag coefficients (C_L and C_D), plotted for a range of angles of attack (α). Some of the comparisons are shown in Figs. 3.3 and 3.4.

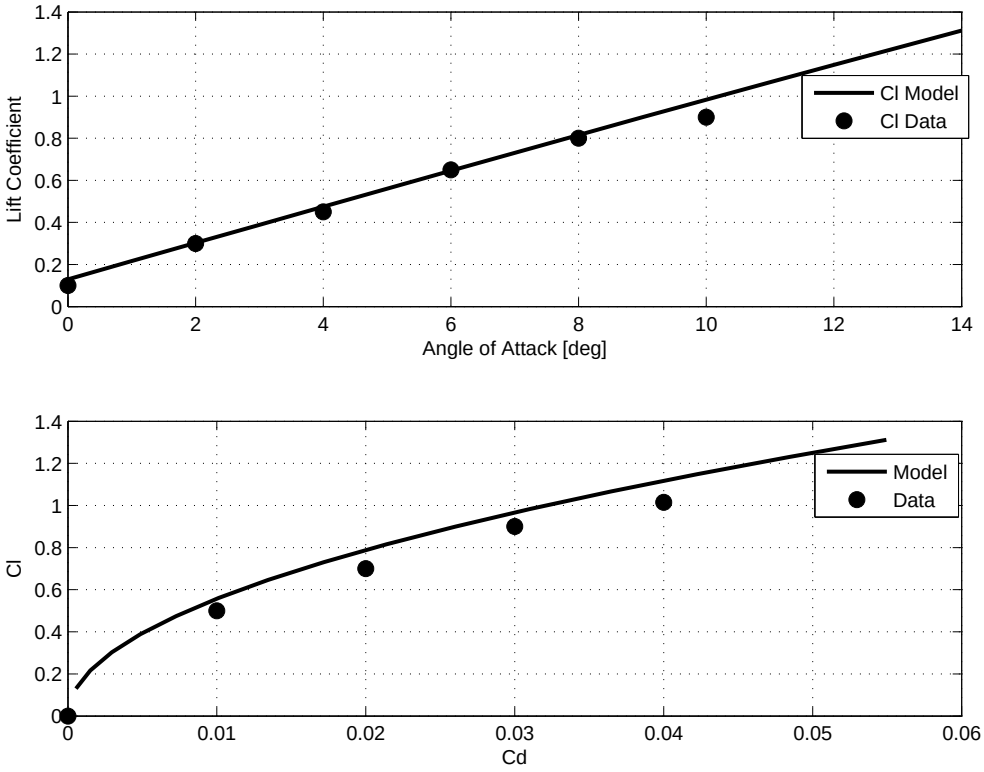

Figure 3.4. VLM-computed lift coefficient for straight wing.

As can be seen in Fig. 3.3, the Vortex-Lattice method provides reasonable results for the lift coefficient at small α. As α grows beyond $\approx 8°$, deviations begin to become apparent. The Vortex-Lattice model predicts a continued increase in the lift coefficient, which is obviously not the case in the measured data. The reason for this is well known; at high α, flow separation begins to occur, with a corresponding reduction in the lift coefficient. Since the Vortex-Lattice model ultimately models potential flow, the viscosity-induced flow separation effect is not captured. Thus, it is important to verify for full flight simulations that α has not exceeded a few degrees, or the aerodynamics must be considered questionable.

A further deficiency of the Vortex-Lattice model is seen in Fig. 3.4. While the general behavior of the C_L and C_D coefficients is seen to be in reasonably good agreement with the measured data, it is apparent that the C_D coefficient is slightly

under-predicted. This is not surprising; only induced drag is computed by the Vortex-Lattice method. Viscous drag must be added explicitly.

The above-described deficiencies notwithstanding, the Vortex-Lattice method does produce reasonable results and has been shown to be useful even in the case of unsteady flows [16].

3.2.5 Vortex-Lattice Example: Gull-Wing Aircraft

The Vortex-Lattice method can be applied to a wide variety of aircraft. The application to the gull-wing aircraft defined in section 2.3 is described next. The aerodynamic properties are investigated under static (or "wind-tunnel") conditions. The lift, drag, and moment coefficients are investigated as a function of the α and β angles. It should be noted that the moments (and hence moment coefficients) are computed with respect to the CM of the aircraft and not the aerodynamic center of the wings.

The expected results are obtained (Fig. 3.5) for trimmed flight, with varying α and 0° β. The Lift-Drag polar is slightly offset from the $C_L = 0$ line. The 0-Lift condition is attained at a negative α (as seen in Fig 3.5), which results in a non-zero induced drag. As a consequence, induced drag is non-zero for all flight conditions. Viscous drag is not included in Fig. 3.5, since it is not computed by the Vortex-Lattice method (a model for viscous drag is included for full flight simulation, however). As expected, increased α results in increased lift and drag, with a non-zero lift coefficient at $\alpha = 0$ due to wing curvature and angle. The aircraft is seen to be statically stable in pitch, with increasing α resulting in a negative pitching moment.

The aerodynamic response of the aircraft to sideslip angle variation is illustrated in Fig. 3.6. As expected for a swept-wing aircraft, β variations tend to increase lift, due to the more favorable angle of incidence of one of the wings. The other wing

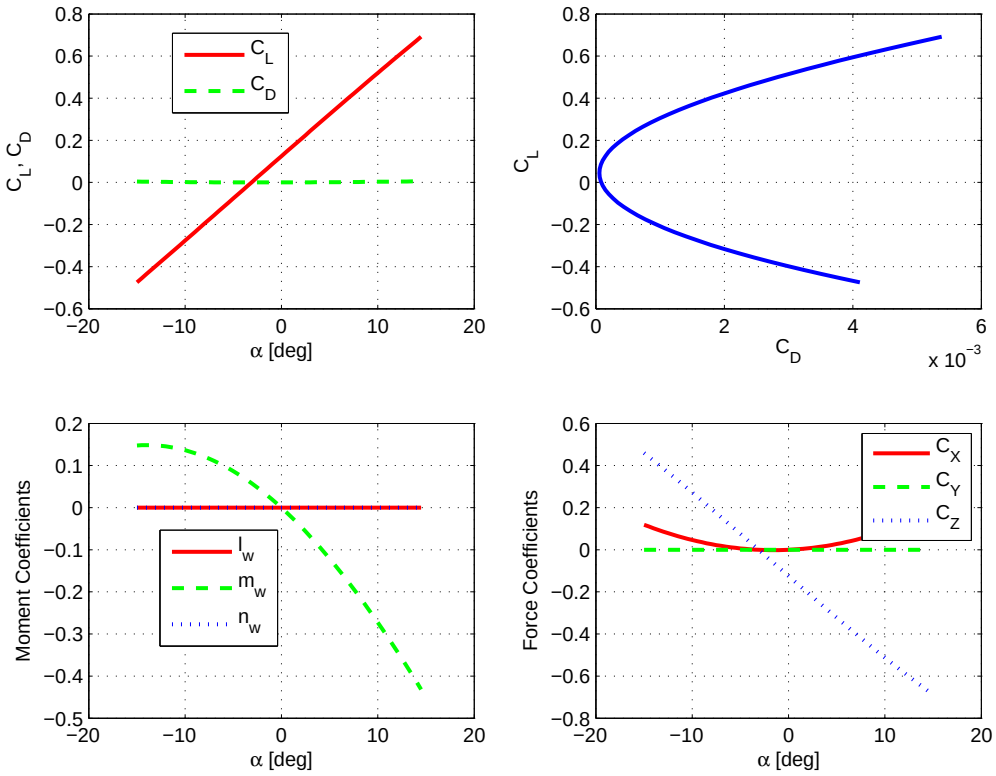

Figure 3.5. Basic α-sweep aerodynamic characteristics of a gull-wing aircraft.

has reduced lift. To first order, the two effects cancel out, but a 2^{nd} order increase is seen at high sideslip angles (though it must be questioned whether the Vortex-Lattice approach is suitable for the high sideslip angles illustrated in Fig. 3.6). The moment coefficients indicate that the aircraft is statically stable in yaw (simply a result of the sufficiently large ruddervons), and it experiences a sideslip-induced roll moment. The roll moment is a consequence of the asymmetry in lift, as previously described. Finally, a side-force is apparent, caused by the increasing Y-projection of drag with increasing sideslip angle.

The inclusion of the angular velocity and morphing terms in Eq. (3.7) results in angular damping moments. Thus, important effects such as pitch and roll damping can be simulated. This is illustrated in Figs. 3.7 through 3.9. At the zero-angular

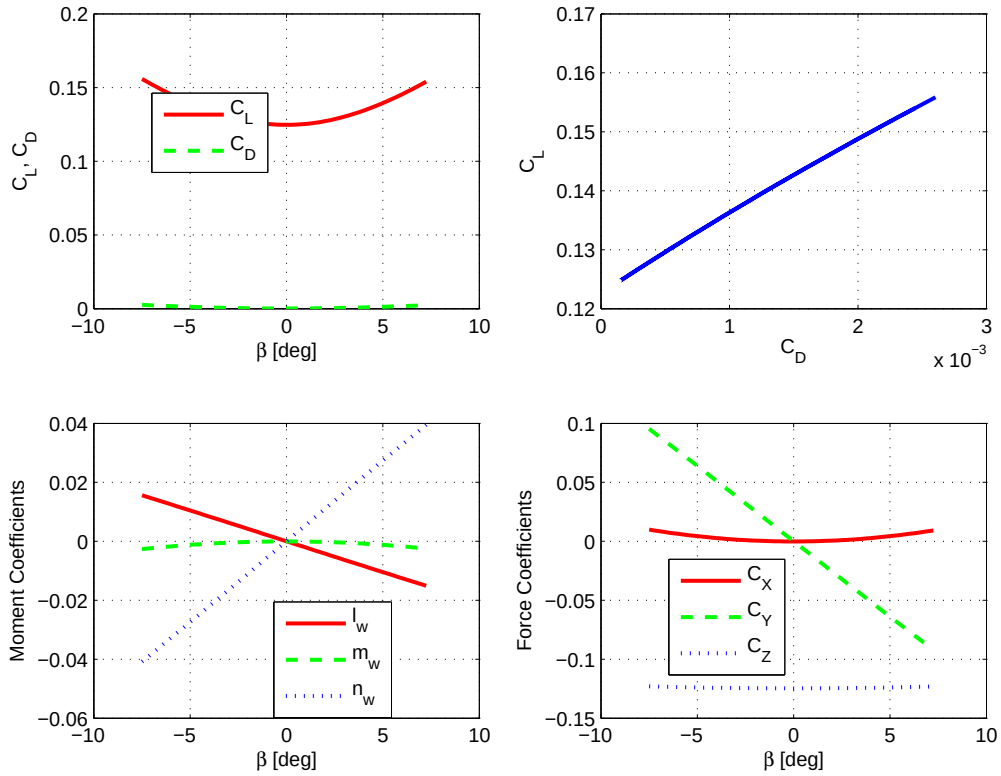

Figure 3.6. Basic β-sweep aerodynamic characteristics of a gull-wing aircraft.

velocity point on each of the Figs. 3.7 through 3.9, the aircraft is trimmed for level flight. The moments are then evaluated as functions of angular velocities directed along the x, y, and z body axes. In each case, a nearly linearly varying damping moment is obtained (resulting in nearly constant damping coefficients). Note that in each case, the sign of the moments opposes the asserted angular velocity, helping to stabilize the aircraft. This is to be expected.

In addition to the behavior w.r.t. the wind-frame variables (as described above), the behavior of the aerodynamic forces and moments as functions of the gull angle is crucial to the flight dynamics of the aircraft. This is illustrated in Fig. 3.10. As expected, the maximum in lift and drag is obtained in the flat-wing configuration, while both the gull-wing and the inverted gull-wing configuration show reduced lift

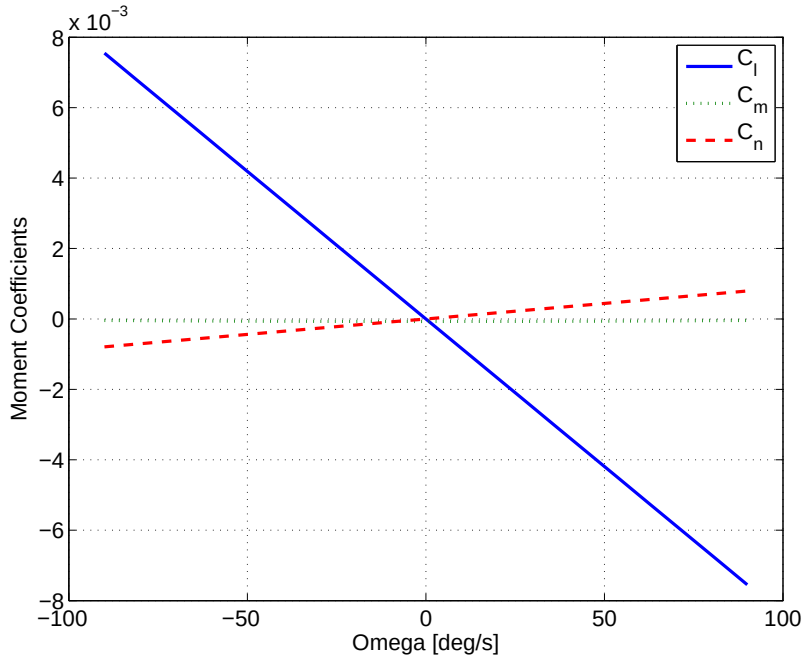

Figure 3.7. Moment coefficients as functions of the x-directed angular velocity.

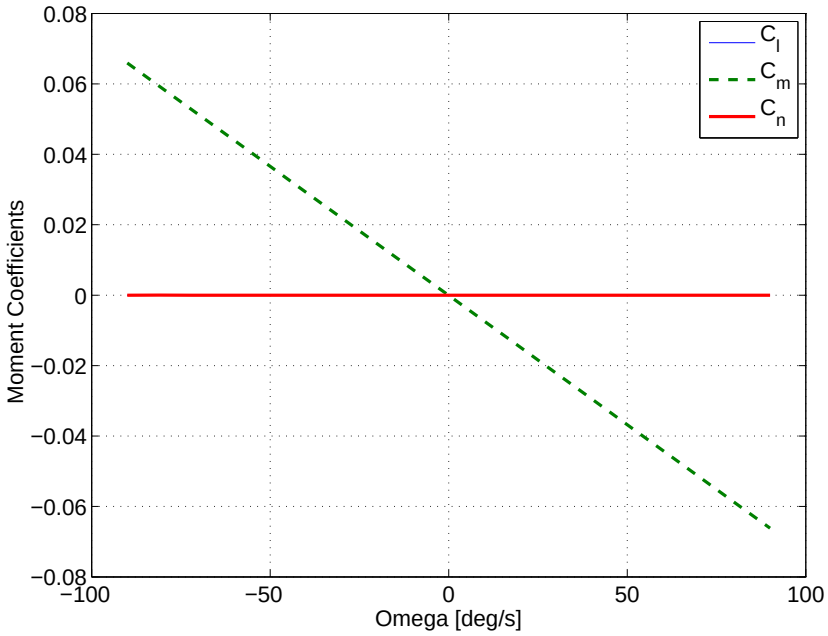

Figure 3.8. Moment coefficients as functions of the y-directed angular velocity.

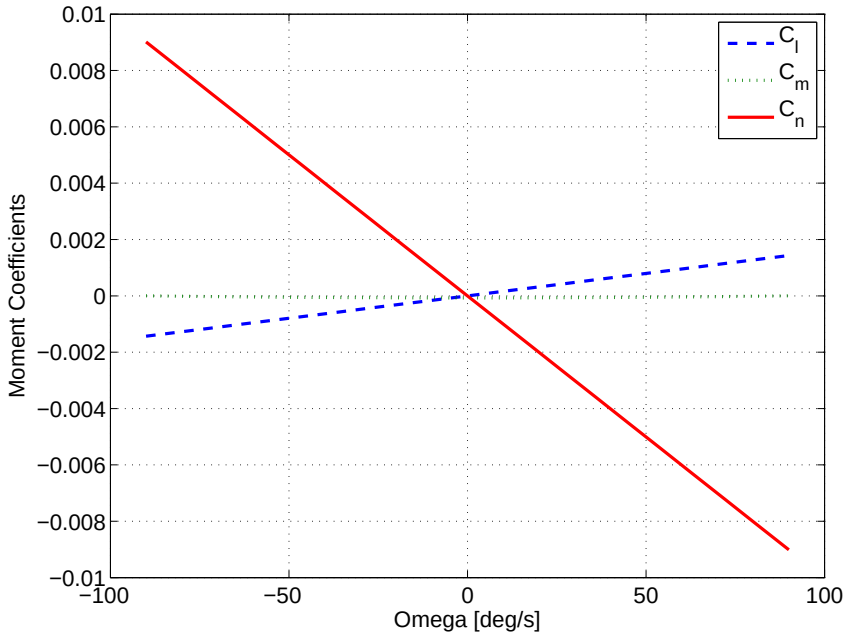

Figure 3.9. Moment coefficients as functions of the z-directed angular velocity.

and drag. The flat-wing configuration provides the optimal L/D ratio. For this particular case, the ruddervons were adjusted to provide pitch trim at 0° gull angle. From the $C_L - C_D$ polar, it is evident that the gull-wing and inverted gull-wing configurations are not symmetric. This is a result of the asymmetry (airfoil with camber, rotated by 2° to provide $0-\alpha$ lift) of the wing itself , as well as the interaction with the ruddervons, since the ruddervons also produce lift and drag.

The conditions illustrated in Figs. 3.5 and 3.6 describe relatively small deviations around a single trim point. It is also of interest to investigate the behavior of the aircraft for various trim point conditions. The dependence of the required wing configuration on the desired cruise velocity is investigated next. The aircraft model is trimmed to a given flight condition by adjusting the wing-fold angle, the ruddervon angle, and the engine thrust. The flight condition is level flight ($\theta = \alpha$), with a small angle-of-attack α ($0° - 3°$), and airspeeds ranging from 60 m/s to 120 m/s.

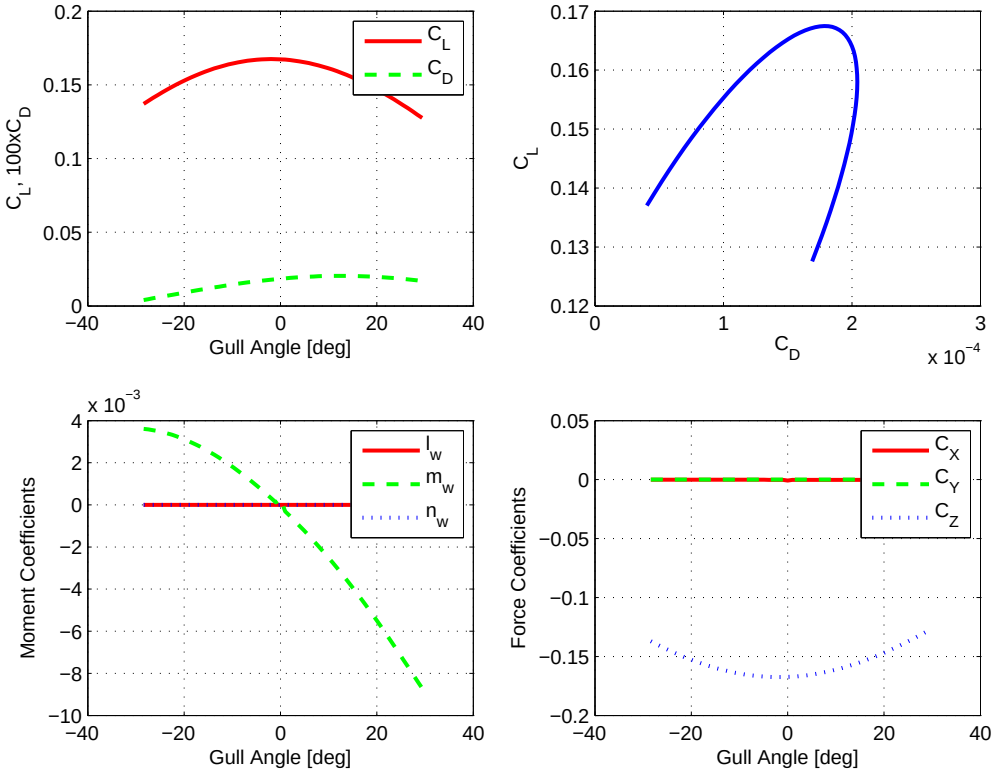

Figure 3.10. Impact of gull angle on aircraft aerodynamics.

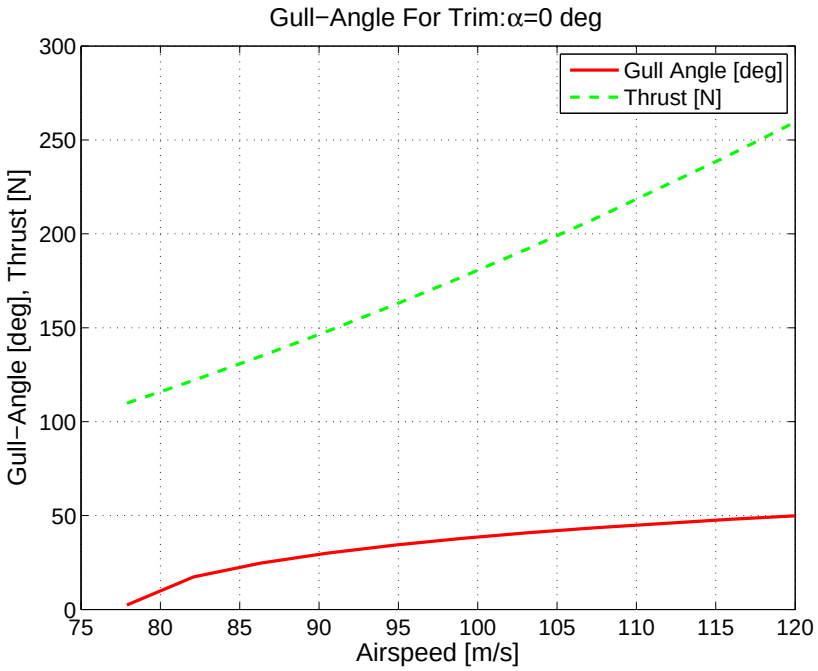

Figure 3.11. Gull-angle for trim at $\alpha = 0°$.

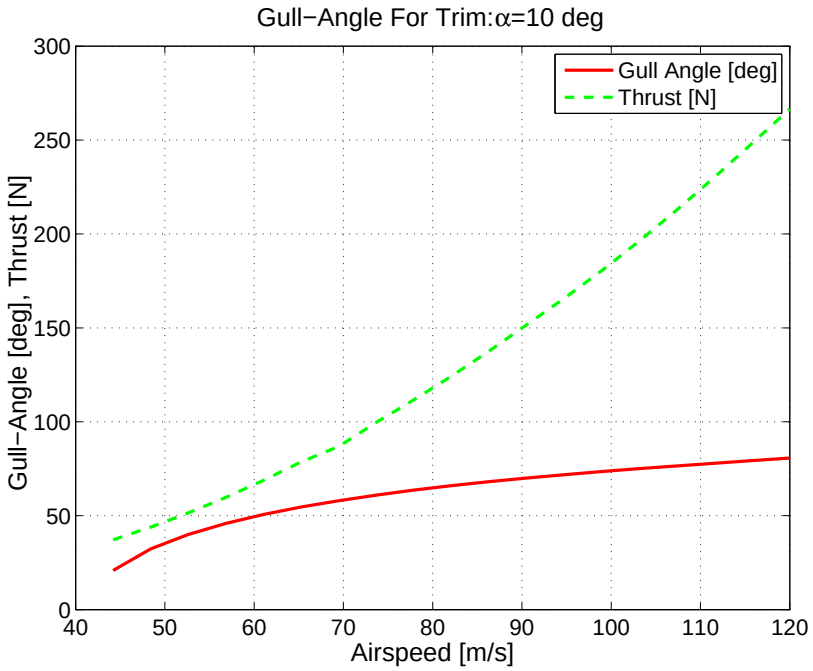

Figure 3.12. Gull-angle for trim at $\alpha = 10°$.

From Figs. 3.11 and 3.12, it is evident that for any desired angle of attack, the aircraft can cruise across a finite range of speeds. In order to achieve the required lift, the wing-fold angle is optimized. At low speeds, the wings are nearly flat, as maximum lift is required. As the airspeed increases, the required amount of lift is decreased, and the wing-fold angle is increased (i.e., the aircraft becomes more "gull-shaped"). While the drag coefficient does drop with increasing wing-fold angle (as illustrated in Fig. 3.13), the overall drag nevertheless increases (due to the quadratic rise in the dynamic pressure with increasing airspeed). Finally, we can observe that this aircraft is not capable of independent takeoff and landing, since the stall speed with fully unfurled wings and a 10° flare angle is ≈ 40 m/s. Thus, the aircraft requires catapult launch and capture recovery, which is not unusual for small UAVs.

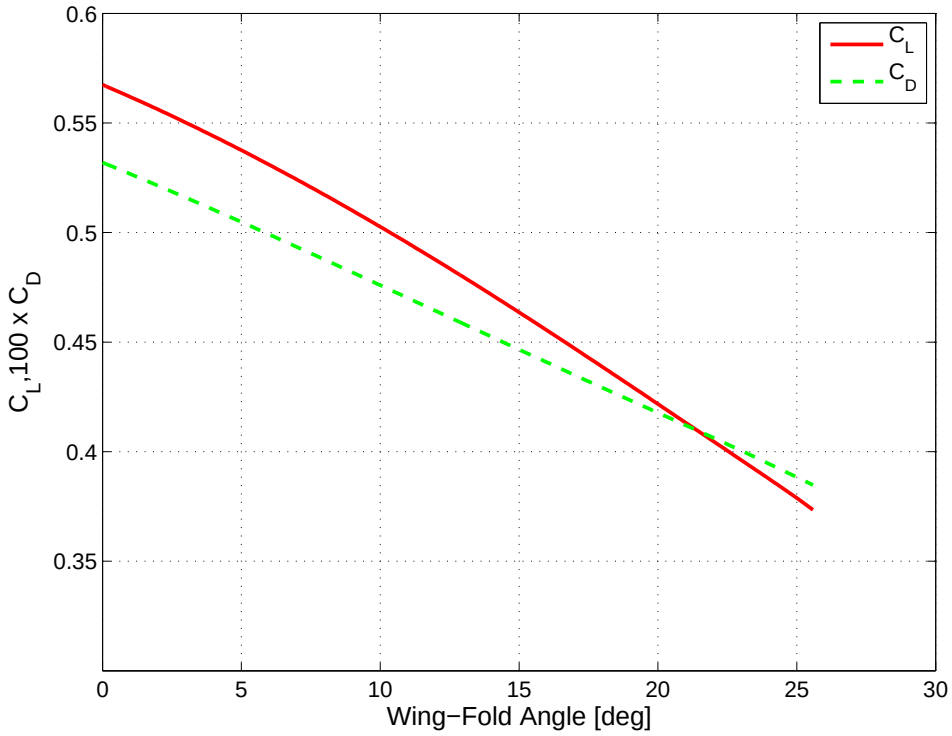

Figure 3.13. Behavior of C_L and C_D with gull-angle variation.

CHAPTER 4

MODELING OF FLIGHT DYNAMICS

4.1 Equations of Motion of Morphing Aircraft

The standard approach to modeling aircraft dynamics is that of rigid-body motion. In this approach, the aircraft is considered rigid (with a constant inertia tensor), and the Euler-Newton equations of motion are derived. This results in three equations for rotational dynamics, three equations for translational dynamics, and an additional set of equations for rotational and translational kinematics (the exact number depends on the choice of parameterization of rotations). For a morphing aircraft, however, the rigid body dynamics approach is insufficient. By definition, the subject of investigation is the class of aircraft which are significantly modified by morphing, and whose inertia tensor cannot be treated as constant. Furthermore, the morphing motion itself induces dynamics which are not modeled by the rigid-body equations. Thus, a more detailed approach is required, enabling the modeling of morphing effects.

Several approaches could be used to remedy the situation. One possibility is to apply the methods of Multi-Body Dynamics [5, 6], treating each moving part of the aircraft as a separate rigid body. Depending on the choice of sub-method, this results in either a large system of loosely coupled Ordinary Differential Equations (ODEs) and a set of algebraic constraint equations, or a tightly coupled, highly non-linear set of ODEs. Either possibility entails a significantly greater computational effort than that required for rigid body dynamics.

Another approach is to continue to treat the morphing aircraft as a single body but relax the condition of "rigidity" - hereafter referred to as extended rigid-body dynamics. The inertia tensor becomes an explicit function of time, since it will depend on the displacements and rotations of the various components of the aircraft. Additionally, the CM of the aircraft will generally not be fixed in the body frame.

Choosing to fix the body frame coordinate system at a reference point (which is most conveniently the unperturbed CM) in the aircraft, the CM coordinates also become explicit functions of time. In spite of this complication, the computational effort is considerably smaller than with either flavor of Multi-Body Dynamics. Therefore, relaxing the rigidity is the method of choice in this work. It must be pointed out, however, that by making the aircraft configuration an explicit function of time, we have neglected the detailed actuator dynamics as well as the constraint and actuator forces and moments required to produce the desired aircraft configuration. We simply assume that the aircraft is able to achieve the desired configuration. The actual magnitudes of the moments and required power can be post-processed and even used in designing a control system for the aircraft.

In this work, we adopt the extended rigid-body dynamics approach and derive the rotational and translation equations of motion for a morphing body. Additionally, we derive the required actuator forces, moments, and power.

4.1.1 Rotational Equations of Motion

In order to derive the appropriate equations of motion (EOM), we start with rotational dynamics in the inertial frame. We then have the well-known result [26]:

$$\boldsymbol{\tau_{ext}} = \dot{\mathbf{h}} + m\boldsymbol{\Delta}\tilde{\mathbf{r}}_{\mathbf{cm}}\dot{\mathbf{V}}_{\mathbf{f}} \tag{4.1}$$

In Eq. (4.1), M denotes the total applied moment, m is the total mass of the aircraft, $\mathbf{\Delta\tilde{r}_{cm}}$ is the displacement of the center of mass from the origin of the body frame (in skew-symmetric matrix form), and $\dot{V}_F$ is the inertial-frame velocity of the body frame origin. The angular momentum in the body frame can be expressed as:

$$\mathbf{h} = \int \tilde{\mathbf{r}}([\tilde{\boldsymbol{\omega}}]\mathbf{r} + \mathbf{v}')dm = [\mathbf{J}]\omega + \int \tilde{\mathbf{r}}\mathbf{v}'dm \tag{4.2}$$

The integration is taken over the entire mass of the aircraft. The term $\tilde{r}$ is the skew-symmetric representation of the position of the mass element dm, $\tilde{\omega}$ is the skew-symmetric representation of the body frame angular velocity, and v' is the body frame morphing-induced velocity of the mass element dm. The final velocity term is unique to the morphing aircraft, and it results in the integral on the right-hand side of Eq. (4.2). The term $J\omega$ is simply the standard expression for angular momentum of a rigid body. The rate of change of the body frame angular momentum can then be expressed as:

$$\begin{aligned} [\mathbf{J}]\dot{\boldsymbol{\omega}} + [\dot{\mathbf{J}}]\boldsymbol{\omega} + \int ([\dot{\tilde{\mathbf{r}}}]\mathbf{v}' + [\tilde{\mathbf{r}}]\dot{\mathbf{v}}')dm \quad &+ \quad [\tilde{\boldsymbol{\omega}}][\mathbf{J}]\boldsymbol{\omega} + [\tilde{\boldsymbol{\omega}}]\int [\tilde{\mathbf{r}}]\mathbf{v}'dm \\ &= \quad \boldsymbol{\tau_{ext}} - m\Delta[\tilde{\mathbf{r}}_{\mathbf{cm}}]\left(\dot{\mathbf{V}}_{\mathbf{f}} + [\tilde{\boldsymbol{\omega}}]\mathbf{V}_{\mathbf{f}}\right) \end{aligned} \tag{4.3}$$

The first term in the left-most integral vanishes, and we are left with the rotational equation of motion of the morphing aircraft in the body frame:

$$\begin{aligned} [\mathbf{J}]\dot{\omega} = \boldsymbol{\tau_{ext}} - [\tilde{\boldsymbol{\omega}}][\mathbf{J}]\boldsymbol{\omega} - \Bigg([\dot{\mathbf{J}}]\boldsymbol{\omega} + m[\mathbf{\Delta\tilde{r}_{cm}}]\left(\dot{\mathbf{V}}_{\mathbf{f}} + [\tilde{\boldsymbol{\omega}}]\mathbf{V}_{\mathbf{f}}\right) \quad &+ \quad [\tilde{\boldsymbol{\omega}}]\int [\tilde{\mathbf{r}}]\mathbf{v}'dm \\ &+ \quad \int [\tilde{\mathbf{r}}]\dot{\mathbf{v}}'dm\Bigg) \end{aligned} \tag{4.4}$$

The terms in parentheses on the RHS of Eq. (4.4) are moments (referred to as "morphing moments" in this work) that are not present in the standard Euler equations for rigid body motion. Explicitly, they arise from the displacement of the CM from the

body frame origin, the rate of change of the inertia tensor, and the body frame motion of mass within the aircraft. For the sake of notational compactness in subsequent sections, the morphing moments will be labelled as follows:

$$\mathbf{M_1} = -[\dot{\mathbf{J}}]\boldsymbol{\omega} \tag{4.5}$$

$$\mathbf{M_2} = -m\Delta[\tilde{\mathbf{r}}_{\mathbf{cm}}] \cdot \left(\dot{\mathbf{V}}_{\mathbf{f}} + [\tilde{\boldsymbol{\omega}}]\mathbf{V_f}\right) \tag{4.6}$$

$$\mathbf{M_3} = -[\tilde{\boldsymbol{\omega}}] \int [\tilde{\mathbf{r}}]\mathbf{v}' dm \tag{4.7}$$

$$\mathbf{M_4} = -\int [\tilde{\mathbf{r}}]\dot{\mathbf{v}}' dm \tag{4.8}$$

For the special case of the rigid body, the morphing moments vanish, the inertia tensor is constant, and the rotational dynamics revert to the Euler equations. The final two terms involve non-trivial integrals and must be treated numerically (described in subsequent section). The relative importance of the various morphing moments will naturally depend on the aircraft as well as the flight conditions. This is studied in more detail on several morphing-induced turns in chapter 5.

4.1.2 Translational Equations of Motion

The translational dynamics are handled similarly to the rotational dynamics. The CM is not fixed at the body frame origin. The position, velocity, and acceleration of the CM in the inertial frame can be then be written as:

$$\mathbf{R_{cm}} = \mathbf{R_f} + \boldsymbol{\Delta}\mathbf{r_{cm}} \tag{4.9}$$

$$\mathbf{V_{cm}} = \mathbf{V_f} + \boldsymbol{\Delta}\dot{\mathbf{r}}_{\mathbf{cm}} + [\tilde{\boldsymbol{\omega}}]\mathbf{r_{cm}} \tag{4.10}$$

$$\dot{\mathbf{V}}_{\mathbf{cm}} = \frac{\mathbf{F_{ext}}}{m} + \mathbf{g} \tag{4.11}$$

$$\dot{\mathbf{V}}_{\mathbf{cm}} = \dot{\mathbf{V}}_{\mathbf{f}} + [\tilde{\boldsymbol{\omega}}]\mathbf{V_f} + \boldsymbol{\Delta}\ddot{\mathbf{r}}_{\mathbf{cm}} + 2[\tilde{\boldsymbol{\omega}}]\dot{\mathbf{r}}_{\mathbf{cm}} + [\dot{\tilde{\boldsymbol{\omega}}}]\boldsymbol{\Delta}\mathbf{r_{cm}} + [\tilde{\boldsymbol{\omega}}][\tilde{\boldsymbol{\omega}}]\boldsymbol{\Delta}\mathbf{r_{cm}} \tag{4.12}$$

The equation of motion for the origin of the body frame then reads:

$$\begin{aligned} m\dot{\mathbf{V}}_{\mathbf{f}} &= \mathbf{F}_{\mathbf{ext}} + m\mathbf{g} - m[\tilde{\boldsymbol{\omega}}]\mathbf{V}_{\mathbf{f}} \\ &- \left(m\boldsymbol{\Delta}\ddot{\mathbf{r}}_{\mathbf{cm}} + 2m[\tilde{\boldsymbol{\omega}}]\dot{\mathbf{r}}_{\mathbf{cm}} + m[\dot{\tilde{\boldsymbol{\omega}}}]\boldsymbol{\Delta}\mathbf{r}_{\mathbf{cm}} + m[\tilde{\boldsymbol{\omega}}][\tilde{\boldsymbol{\omega}}]\boldsymbol{\Delta}\mathbf{r}_{\mathbf{cm}} \right) \end{aligned} \tag{4.13}$$

As was the case with rotational dynamics, the translational dynamics exhibit additional terms (in parentheses of Eq. (4.13)), as compared to the standard rigid body equations. The additional terms depend on the displacement of the CM (relative to the origin of the body frame), as well as on its 1^{st} and 2^{nd} derivatives. As in the case of the morphing moments, we define the morphing forces as:

$$\mathbf{F}_{\mathbf{acm}} = -m\boldsymbol{\Delta}\ddot{\mathbf{r}}_{\mathbf{cm}} \tag{4.14}$$

$$\mathbf{F}_{\mathbf{vcm}} = -2m[\tilde{\boldsymbol{\omega}}]\boldsymbol{\Delta}\dot{\mathbf{r}}_{\mathbf{cm}} \tag{4.15}$$

$$\mathbf{F}_{\dot{\omega}} = -m[\dot{\tilde{\boldsymbol{\omega}}}]\boldsymbol{\Delta}\mathbf{r}_{\mathbf{cm}} \tag{4.16}$$

$$\mathbf{F}_{\omega\omega} = -m[\tilde{\boldsymbol{\omega}}][\tilde{\boldsymbol{\omega}}]\boldsymbol{\Delta}\mathbf{r}_{\mathbf{cm}} \tag{4.17}$$

4.2 Modeling of Morphing

Since the aircraft undergoes morphing, various dynamic properties must change in the body frame. For example, the $\boldsymbol{\Delta}\mathbf{r}_{\mathbf{cm}}$ term is a function of the applied configuration q; rotations and displacements $\{q_1, q_2, ...q_n\}$ of wing sections (or other parts of the aircraft) result in changes of $\boldsymbol{\Delta}\mathbf{r}_{\mathbf{cm}}$, and the same is true for the inertia tensor. In reality, however, these deflections cannot occur instantaneously. Had we modeled the aircraft using a Multi-Body Dynamics approach, this would have arisen naturally. In the present formulation, however, the dynamics of the actuation have to be introduced separately. In addition, we must use a model for the dynamics, since the deflections are not handled explicitly. Thus, we introduce state variables for the displacements $\{q_1, q_2, ..., q_n\}$. Since the equations of translational dynamics involve

the 2^{nd} derivative of the CM displacement (itself a function of the configuration variables), we need a 2^{nd} order system to describe the dynamics of each configuration variable. Thus, we also define the state variables $\{p_1, p_2, ..., p_n\}$, with $p_i = \dot{q}_i$. The desired or control input set is then $\{q_{c1}, q_{c2}, ..., q_{cn}\}$. A suitable 2^{nd} order system is simply:

$$\dot{p}_i = -2\xi_i\omega_i p_i - \omega_i^2 \left(q_i - q_{ci}\right) \tag{4.18}$$

$$\dot{q}_i = p_i \tag{4.19}$$

with the parameters ξ_i and ω_i chosen to model an appropriate delay in the particular deflection. Once the dynamics of the actuators have been defined, it becomes possible to compute the instantaneous positions of the planforms, the CM and the inertia tensor, as well as the derivatives of all the body frame quantities. The instantaneous coordinates of the CM are simply obtained as:

$$\mathbf{r_{cm}} = \frac{1}{m}\sum_i \mathbf{r_i} m_i \tag{4.20}$$

where r_i is the position of the CM of the i-th planform of which the aircraft is comprised (also including the fuselage). The position of the CM of each planform is updated as the panel is rotated, translated, or stretched. The instantaneous moment of inertia tensor is computed as:

$$[\mathbf{J'}] = \sum_i \left[[\mathbf{R_i}]^\mathbf{T} [\mathbf{J_i}][\mathbf{R_i}] + m_i [\mathbf{\Delta \tilde{r}_i}][\mathbf{\Delta \tilde{r}_i}]^\mathbf{T} \right] \tag{4.21}$$

where J' is the instantaneous moment of inertia in the body frame, J_i is the moment of inertia of the i-th planform in the reference position (prior to rotation or translation), m_i is the mass of the i-th planform, R_i is the rotation matrix of the i-th planform relative to the inertial frame, and $\Delta\tilde{r}_i$ is the position of the CM of the i-th planform.

The equations of motion require the computation of the 1^{st} and 2^{nd} derivatives of the CM as well as the 1^{st} derivative of the inertia tensor. Since the aircraft can be

arbitrarily complex, an analytical solution is not practical. Instead, the derivatives are computed numerically. However, it is important to avoid using finite differencing in time to obtain the derivatives. This would introduce a timestep-dependent truncation error into the derivatives. Doing so would increase the truncation error of the ODE step. Instead, the derivatives are computed as follows (where $\mathbf{x_i}$ represents a panel coordinate vector or the CM vector):

$$\mathbf{x_i} = \mathbf{x_i}(q_1, q_2, ..., q_n) \tag{4.22}$$

$$\dot{\mathbf{x}}_\mathbf{i} = \sum_k \frac{\partial \mathbf{x_i}}{\partial q_k} \dot{q}_k \tag{4.23}$$

$$\ddot{\mathbf{x}}_\mathbf{i} = \dot{\mathbf{q}}^\mathbf{T} [\mathbf{H_i}] \dot{\mathbf{q}} + \sum_k \frac{\partial \mathbf{x_i}}{\partial q_k} \ddot{q}_k \tag{4.24}$$

where the Hessian term $[\mathbf{H_i}]$ is defined as:

$$[\mathbf{H_i}]_\mathbf{jk} = \frac{\partial^2 \mathbf{x_i}}{\partial q_j \partial q_k} \tag{4.25}$$

Note that each element of the matrix $[\mathbf{H_i}]$ in Eq. (4.47) and Eq. (4.24) is a three-dimensional vector. Similarly, the time derivatives of the inertia tensor can be expressed as:

$$\frac{d[\mathbf{J}]}{dt} = \sum_n \frac{\partial [\mathbf{J}]}{\partial q_n} \dot{q}_n \tag{4.26}$$

Thus, the temporal derivatives of panel coordinates, planform and aircraft CM, as well as inertia tensor components, are computed using numerical differentiation w.r.t. actuator positional variables only. This effectively computes the virtual displacements of the independent coordinates q. Time derivatives are included implicitly in the state variables $\dot{q}_i$. Since the accuracy of the numerical derivatives w.r.t. the actuator kinematic variables is independent of the local ODE integration timestep Δt, the order of the local truncation error w.r.t. Δt does not change. The actual computation of the jacobians w.r.t. the actuator positions is carried out by performing a set of

virtual displacements of the actuator positions at every timestep and using central differences to compute the derivative values. Only a minimal computational overhead is incurred. Numerical integration is required for the final two morphing moments. These are:

$$\mathbf{M_3} = [\tilde{\boldsymbol{\omega}}] \int [\tilde{\mathbf{r}}]\mathbf{v}' dm \approx [\tilde{\boldsymbol{\omega}}] \sum_i [\tilde{\mathbf{r}}]_\mathbf{i} \mathbf{v}'_\mathbf{i} m_i \tag{4.27}$$

and

$$\mathbf{M_4} = \int [\tilde{\mathbf{r}}]\dot{\mathbf{v}}' dm \approx \sum [\tilde{\mathbf{r}}_\mathbf{i}]\dot{\mathbf{v}}'_\mathbf{i} m_i \tag{4.28}$$

The terms inside the integrals are the positions and velocities of the mass elements of the aircraft. Since there is no closed-form solution to the integrals for an arbitrary aircraft, the values of M_3 and M_4 are obtained numerically at each timestep. A natural discretization of the moving planforms is already available for the Vortex-Lattice mesh. However, this potentially represents a large number of points for velocity and acceleration calculations, so the Vortex-Lattice panels are grouped into a smaller number of larger, non-trapezoidal panels. The positions, velocities, and accelerations of the CM of these shapes is then used for the computation of M_3 and M_4. Testing indicates that the values of M_3 and M_4 are converged with as few as 6-8 panels per planform. The velocities and accelerations are computed based on the positions using Eqs. (4.23) and (4.24).

4.3 Dynamic Loads

In the scheme presented, actuator dynamics are modeled by a simple 2^{nd} order system, the details of which are not subject to external loading. Physically, this corresponds to a controlled actuator, in which a model-following control system is used for each actuator. The control system then insures that the actuator behaves according to the equations of the 2^{nd} order system, in spite of the presence of aerodynamic,

inertial, and morphing moments. The question naturally arises whether the actuators for such a control system are feasible. The primary constraints are the required joint moments, peak power, and total energy consumption. Furthermore, knowledge of the actuator moments and power is useful in the design of an "optimal" aircraft control system, where it would be used to penalize actuator deflections. We thus seek the generalized force on each actuator, required to follow the 2^{nd} order actuator dynamics. The result is necessarily approximate, but is suitable for comparisons of moments and power-required for different morphing schemes, as well as for the design of control systems and optimal maneuver trajectories which need to take power into account.

The equations of motion are constructed using Lagrange's equations. Each actuator variable ("morphing" coordinates) is assigned to a generalized coordinate q^j. The overall Lagrangian includes additional generalized coordinates, but the morphing coordinates are of interest for actuator dynamics. Lagrange's equation for the j-th actuator can then be written as:

$$\frac{dP^j}{dt} = \frac{\partial T}{\partial q} + Q^j + Q^j_{aero} \tag{4.29}$$

where Q^j is the generalized force associated with the j-th generalized coordinate (one of the morphing state variables), and P^j is the associated generalized momentum. The generalized force Q^j_{aero} represents the aerodynamic portion of the load (including gravity), and it is computed explicitly from the Vortex-Lattice solution. Since the dynamics of the problem are known (the generalized forces are post-processed after the dynamics at each timestep), the term $\frac{dP^j}{dt}$ can be computed at runtime from the state vector. Thus, Eq. (4.29) can be simply rearranged to yield an expression for the generalized actuator force in terms of known (computable) quantities:

$$Q^j = \frac{dP^j}{dt} - \frac{\partial T}{\partial q} - Q^j_{aero} \tag{4.30}$$

In order to use Eq. (4.30), expressions for $\frac{dP^j}{dt}$ and $\frac{\partial T}{\partial q^j}$ are required. Using the definition of generalized momentum, we have:

$$\frac{dP^j}{dt} = \frac{d}{dt}\left(\frac{\partial T}{\partial \dot{q^j}}\right) \tag{4.31}$$

The kinetic energy part of the Lagrangian is obtained as:

$$T = T_f + \frac{1}{2}\boldsymbol{\omega}^{\boldsymbol{T}}[\boldsymbol{J}]\boldsymbol{\omega} + T_{morph}(q, \dot{q}) \tag{4.32}$$

where T_f is the kinetic energy of the translational velocity of the body frame, $\frac{1}{2}\omega^T J\omega$ is the rotational energy of the body frame, and T_{morph} is the kinetic energy of the intra-body-frame motion of the morphing aircraft components. Specifically, we have:

$$T = \int \frac{1}{2}||\mathbf{V_f} + \mathbf{v}||^2 dm = \int \frac{1}{2}\left(||\mathbf{V_f}||^2 + ||\mathbf{v}||^2 + 2\mathbf{V_f}\cdot\mathbf{v}\right) dm \tag{4.33}$$

$$T = T_f + \int \left(\frac{1}{2}||\mathbf{v}||^2 + \mathbf{V_f}\cdot\mathbf{v}\right) dm \tag{4.34}$$

The term v in Eq. (4.34) represents the velocity of a mass element of the aircraft, including both the rotational velocity of the body frame and the intra-body-frame morphing velocity. The first term (T_f) is the kinetic energy due to the translational motion of the body frame, and it does not explicitly depend on any morphing state variables. Thus, it will not contribute directly to the generalized force. The second term in Eq. (4.34) is further expanded as follows:

$$\begin{aligned}
\int \frac{1}{2}||\mathbf{v}||^2 dm &= \int \frac{1}{2}||[\tilde{\boldsymbol{\omega}}]\boldsymbol{r} + \mathbf{v}'||^2 dm \\
&= \int \frac{1}{2}\left[||[\tilde{\boldsymbol{\omega}}]\boldsymbol{r}||^2 + ||\mathbf{v}'||^2 + 2[\tilde{\boldsymbol{\omega}}]\boldsymbol{r}\cdot\mathbf{v}'\right] dm \\
&= \frac{1}{2}\boldsymbol{\omega}^T[\mathbf{J}]\boldsymbol{\omega} + \frac{1}{2}\int ||\mathbf{v}'||^2 dm + \int ([\tilde{\boldsymbol{\omega}}]\boldsymbol{r})\cdot\mathbf{v}' dm
\end{aligned} \tag{4.35}$$

The third and final term of Eq. (4.34) can be further expressed as:

$$\begin{aligned}\mathbf{V_f} \cdot \int \mathbf{v} dm &= \mathbf{V_f} \cdot \int \left([\tilde{\boldsymbol{\omega}}]\boldsymbol{r} + \mathbf{v}' \right) dm \\ &= \mathbf{V_f} \cdot \int \left([\tilde{\boldsymbol{\omega}}]\boldsymbol{r} \right) dm + \mathbf{V_f} \cdot \int \mathbf{v}' dm \\ &= \mathbf{V_f} \cdot m[\tilde{\boldsymbol{\omega}}]\boldsymbol{\Delta r_{cm}} + m\mathbf{V_f} \cdot \boldsymbol{\Delta \dot{r}_{cm}} \end{aligned} \tag{4.36}$$

Thus, the complete kinetic energy of the morphing aircraft can then be summarized as:

$$\begin{aligned} T &= T_f + \frac{1}{2}\omega^{\mathbf{T}}[\mathbf{J}]\omega + \frac{1}{2}\int ||\mathbf{v}'||^2 dm + \int \left([\tilde{\boldsymbol{\omega}}]\boldsymbol{r} \right) \mathbf{v}' dm \\ &+ \mathbf{V_f} \cdot m[\tilde{\boldsymbol{\omega}}]\boldsymbol{\Delta r_{cm}} + m\mathbf{V_f} \cdot \boldsymbol{\Delta \dot{r}_{cm}} \end{aligned} \tag{4.37}$$

The first two terms in Eq. (4.37) are recognized as the translational kinetic energy of the body frame motion and the rotational kinetic energy of the body frame motion. The remaining terms arise due to morphing.

The generalized momentum associated with the j-th state variable can then be expressed as:

$$P^j = \frac{\partial T}{\partial \dot{q}^j} = m\mathbf{V_f} \cdot \frac{\partial \boldsymbol{\Delta \dot{r}_{cm}}}{\partial \dot{q}^j} + \int \left([\tilde{\boldsymbol{\omega}}]\boldsymbol{r} \right) \frac{\partial \mathbf{v}'}{\partial \dot{q}^j} dm + \int \mathbf{v}' \frac{\partial \mathbf{v}'}{\partial \dot{q}^j} dm \tag{4.38}$$

where only terms that are explicit functions of the morphing state variable derivatives are included. Noting that the term $\mathbf{v}'$ is the body-frame temporal derivative of the position vector $\mathbf{r}$ and simplifying, we have:

$$P^j = m\mathbf{V_f} \cdot \frac{\partial \boldsymbol{\Delta \dot{r}_{cm}}}{\partial \dot{q}^j} + [\tilde{\boldsymbol{\omega}}] \int \mathbf{r} \frac{\partial \dot{\mathbf{r}}}{\partial \dot{q}^j} dm + \int \mathbf{v}' \frac{\partial \dot{\mathbf{r}}}{\partial \dot{q}^j} dm \tag{4.39}$$

The joints are assumed to enforce holonomic constrains only. Therefore, applying "cancellation of dots", we have:

$$P^j = m\mathbf{V_f} \cdot \frac{\partial \boldsymbol{\Delta r_{cm}}}{\partial q^j} + \int \left([\tilde{\boldsymbol{\omega}}]\boldsymbol{r} + \mathbf{v}' \right) \frac{\partial \mathbf{r}}{\partial q^j} dm \tag{4.40}$$

Finally, in order to obtain the generalized force in Equation 4.29, the time derivative of Eq. (4.40) is performed. The obtained result is:

$$\begin{aligned}
\dot{P}^j &= m\left(\dot{\mathbf{V}}_\mathbf{f} + [\tilde{\boldsymbol{\omega}}]\boldsymbol{V_f}\right)\cdot\frac{\partial\boldsymbol{\Delta}\mathbf{r_{cm}}}{\partial q^j} + m\mathbf{V_f}\cdot\left(\frac{\partial\boldsymbol{\Delta}\dot{\mathbf{r}}_\mathbf{cm}}{\partial q^j} + [\tilde{\boldsymbol{\omega}}]\frac{\partial\boldsymbol{\Delta}\mathbf{r_{cm}}}{\partial q^j}\right) \\
&+ \int\left([\tilde{\boldsymbol{\omega}}][\tilde{\boldsymbol{\omega}}]\boldsymbol{r} + 2[\tilde{\boldsymbol{\omega}}]\boldsymbol{v'} + [\dot{\tilde{\boldsymbol{\omega}}}]\boldsymbol{r} + \dot{\mathbf{v}}'\right)\frac{\partial\mathbf{r}}{\partial q^j}dm \\
&+ \int\left([\tilde{\boldsymbol{\omega}}]\boldsymbol{r} + \mathbf{v}'\right)\left(\frac{d}{dt}\frac{\partial\mathbf{r}}{\partial q^j} + [\tilde{\boldsymbol{\omega}}]\frac{\partial\boldsymbol{\Delta}\mathbf{r_{cm}}}{\partial q^j}\right)dm \qquad (4.41)
\end{aligned}$$

From a computational standpoint w.r.t. geometrical derivatives, the various terms in Eq. (4.41) can be grouped into five categories: terms which depend on the geometrical derivatives of the CM, the time derivative of the geometrical derivatives of the CM, the geometrical derivatives of panel coordinates, the time derivative of the geometrical derivatives of panel coordinates, and finally, a mixed term which combines panel derivatives and CM derivatives. As will be demonstrated in section 5.2.3, the terms involving time derivatives of the geometric derivatives (i.e. $\frac{d}{dt}\frac{\partial\Delta r_{cm}}{\partial q^j}$) are negligible (but they are included here for completeness).

In order to finalize the computation of the generalized force, the partial derivative of the kinetic energy (second term on RHS of Eq. (4.30)) is derived next:

$$\begin{aligned}
\frac{\partial T}{\partial q^j} &= \int\mathbf{v}'\frac{\partial\mathbf{v}'}{\partial q^j}dm + \int[\tilde{\boldsymbol{\omega}}]\frac{\partial\mathbf{r}}{\partial q^j}\mathbf{v}'dm + \int[\tilde{\boldsymbol{\omega}}]\boldsymbol{r}\frac{\partial\mathbf{v}'}{\partial q^j}dm \\
&+ m\mathbf{V_f}\cdot[\tilde{\boldsymbol{\omega}}]\frac{\partial\boldsymbol{\Delta}\mathbf{r_{cm}}}{\partial q^j} + m\mathbf{V_f}\cdot\frac{\partial\boldsymbol{\Delta}\dot{\mathbf{r}}_\mathbf{cm}}{\partial q^j} \qquad (4.42)
\end{aligned}$$

In Eq. (4.42), the first, third, and last terms on the RHS prove to be negligible (section 5.2.3), since they represent mixed temporal and geometrical derivatives. The third term of Eq. (4.41) cancels the fourth term of Eq. (4.42). Likewise, the 2^{nd} term of Eq. (4.41) cancels the last term of Eq. (4.42). The 2^{nd} term of Eq. (4.42) is identical to the "Coriolis" term of Eq. (4.41) to within a prefactor, and converts the

Coriolis prefactor of two to three. Collecting the terms of Eqs. (4.41) and (4.42) and dropping the negligible and canceled terms, the various components of the generalized actuator force are summarized as:

$$Q_{CM} = m\frac{\partial \mathbf{\Delta r_{cm}}}{\partial q^j} \cdot \left(\dot{\mathbf{V}}_\mathbf{f} + [\tilde{\boldsymbol{\omega}}]\boldsymbol{V_f}\right) \tag{4.43}$$

$$Q_{Panel} = \int \left([\tilde{\boldsymbol{\omega}}][\tilde{\boldsymbol{\omega}}]\boldsymbol{r} + 3[\tilde{\boldsymbol{\omega}}]\boldsymbol{v'} + [\dot{\tilde{\boldsymbol{\omega}}}]\boldsymbol{r} + \dot{\mathbf{v}}'\right)\frac{\partial \mathbf{r}}{\partial q^j}dm \tag{4.44}$$

$$Q_{Panel-Rate} = \int \left([\tilde{\boldsymbol{\omega}}]\boldsymbol{r} + \mathbf{v}'\right)\left(\frac{d}{dt}\frac{\partial \mathbf{r}}{\partial q^j}\right)dm \tag{4.45}$$

$$Q_{Mixed} = \int \left([\tilde{\boldsymbol{\omega}}]\boldsymbol{r} + \mathbf{v}'\right)[\tilde{\boldsymbol{\omega}}]\frac{\partial \mathbf{\Delta r_{cm}}}{\partial q^j}dm \tag{4.46}$$

From a physical standpoint, Eqs. (4.43) through (4.46) contain two types of terms: those induced by morphing, and those that are purely inertial in nature. Terms which depend explicitly on morphing velocities or accelerations are present only in morphing aircraft. Inertial terms, which do not depend on the derivatives of morphing terms, exist in any aircraft type. Note that the term $m\dot{\mathbf{V}}_\mathbf{f}\frac{\partial \mathbf{\Delta r_{cm}}}{\partial q^j}$ is not actually a purely morphing term. The partial derivative of the CM w.r.t. joint angles is non-vanishing even when the CM is never displaced from its original position. The geometrical derivative $\frac{\partial \mathbf{\Delta r_{cm}}}{\partial q^j}$ represents a sensitivity parameter which determines the degree of coupling of the CM motion to virtual displacements of the wing actuators. Thus, even for non-morphing aircraft, this formalism is useful for studying the induced joint moments, as the first step in an flexibility analysis. The morphing and inertial contributions of the various Q-terms is summarized in Table 4.1

Three types of derivatives appear in Eqs. (4.41) and (4.42): temporal derivatives of panel coordinates (or CM) such as $\dot{\mathbf{r}}_i$, purely geometrical derivatives such as $\frac{\partial \mathbf{r}_i}{\partial q^j}$, and time derivatives of the geometric derivatives, such as $\frac{d}{dt}\left(\frac{\partial \mathbf{r}_i}{\partial q^j}\right)$. The first two

Table 4.1. Summary of actuator generalized force properties

Term Type	Q_{CM}	Q_{Panel}	$Q_{Panel-Rate}$	Q_{Mixed}
Morphing	Yes	Yes	Yes	Yes
Inertial	Yes	Yes	No	Yes

derivative types are handled in a straightforward manner; the last is computed as follows:

$$\frac{d}{dt}\left(\frac{\partial \mathbf{X}}{\partial q^j}\right) = \sum_k \frac{\partial}{\partial q^k}\frac{\partial \mathbf{X}}{\partial q^j}\dot{q}^k = \sum_k = [\mathbf{H}]_{kj}\dot{q}^k \tag{4.47}$$

where the elements of the Hessian matrix $[\mathbf{H}]$ in Eq. (4.47) are the purely geometric 2^{nd} order partial derivatives given by:

$$[\mathbf{H}]_{kj} = \frac{\partial^2 \mathbf{X}}{\partial q^k \partial q^j} \tag{4.48}$$

and X is a placeholder for a panel coordinate, or the CM. Similarly, mixed temporal and geometrical derivatives appear in terms such as:

$$\frac{\partial \dot{\mathbf{\Delta r}}_{\mathbf{cm}}}{\partial q^j} = \sum_k \frac{\partial^2 \mathbf{\Delta r}_{\mathbf{cm}}}{\partial q^j \partial q^k}\dot{q}^k \tag{4.49}$$

also requiring the computation of Hessian terms. It can be anticipated that terms which include the Hessian will be of lesser importance (this is verified by explicit simulation in section 5.2.3). These expressions represent the 2^{nd} order terms in the Taylor expansion of the functional dependence of panel coordinates (or the CM) on the morphing coordinates. Thus, we can write for a panel coordinate r_i:

$$\begin{aligned} \mathbf{r}_i(q_1, q_2, ..., q_n) &= \mathbf{r}_i(q_{01}, q_{02}, ..., q_{0n}) + \nabla_q \mathbf{r}_i \cdot (dq_1, dq_2, ..., dq_n) \\ &+ \sum_k \sum_j \frac{\partial^2 \mathbf{r}_i}{\partial q^j \partial q^k} dq^k dq^j + O(dq^3) \end{aligned} \tag{4.50}$$

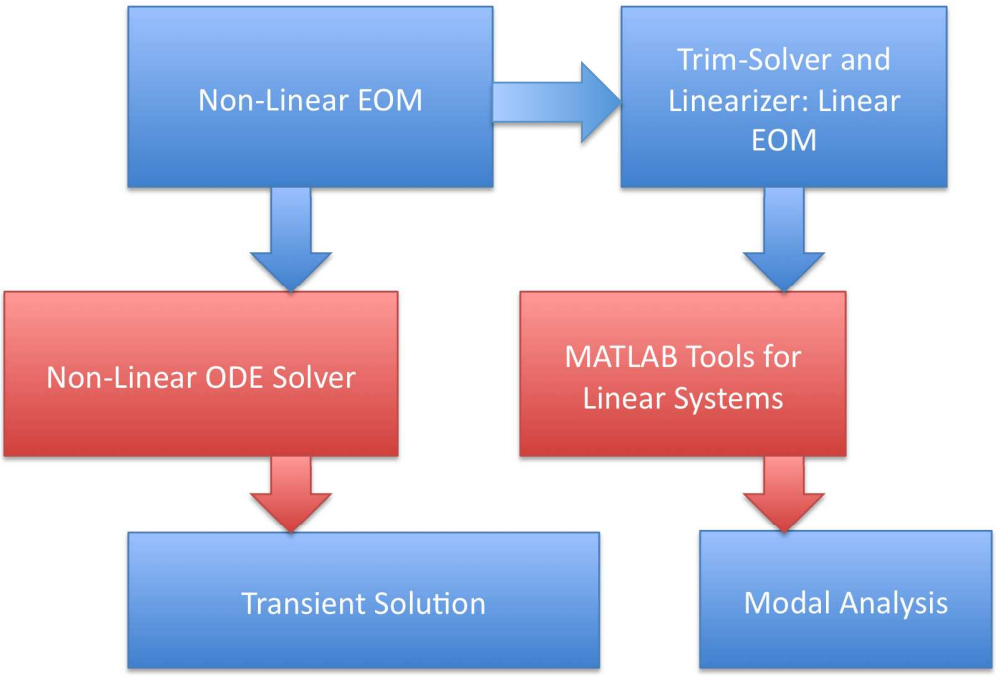

Figure 4.1. Relationship of the various solvers and types of solution.

The mixed derivatives appearing with the 2^{nd} order terms in Eq. (4.50) are just the Hessians of Eq. (4.47). Thus, dropping terms with Hessians is equivalent to a 1^{st} order Taylor expansion of the transformation between body-frame Cartesian coordinates and morphing coordinates. When the aircraft is operating close to a trim point, we can expect the 2^{nd} order contributions to be small. This is investigated and found to be true in section 5.2.3.

4.4 Simulation of Flight Dynamics

The simulation framework provides two modes of flight simulation: non-linear integration of the equations of motion, and linearization of the equations around a trim point. In the latter case, standard methods of linear system simulation are employed. The relationship between the various simulation methods is illustrated in Fig. 4.1.

The translational and rotational equations of motion are described in sections 4.1.2 and 4.4. The full set of equations to be solved includes the translational and rotational dynamics, translational and rotational kinematics, as well as the actuator and thrust equations. Together, they comprise a non-linear, first-order system of differential equations, described by a state-space system as follows:

$$\dot{\mathbf{x}} = \mathbf{F}(\mathbf{x}, \mathbf{u}(t)) \tag{4.51}$$

The vector F in Eq. (4.51) consists of the following components:

$$\begin{pmatrix} \dot{\mathbf{V}}_\mathbf{f} \\ [\dot{\boldsymbol{\omega}}] \\ [\dot{\mathbf{C}}_\mathbf{x}] \\ [\dot{\mathbf{C}}_\mathbf{y}] \\ [\dot{\mathbf{C}}_\mathbf{z}] \\ \dot{\mathbf{X}} \\ \dot{p}_{act1} \\ \dot{q}_{qct1} \\ \dot{p}_{act2} \\ \dot{q}_{act2} \\ . \\ . \\ . \end{pmatrix} = \begin{pmatrix} \frac{\mathbf{F_{ext}}}{m} + \mathbf{g} - [\tilde{\omega}]\mathbf{V}_\mathbf{f} - \frac{1}{m}\left(\mathbf{F_1} + \mathbf{F_2} + \mathbf{F_3} + \mathbf{F_4}\right) \\ [\mathbf{J}]^{-1}\left(\tau - [\tilde{\boldsymbol{\omega}}]^{\boldsymbol{T}}[\boldsymbol{J}]\boldsymbol{\omega} - \mathbf{M_1} - \mathbf{M_2} - \mathbf{M_3} - \mathbf{M_4}\right) \\ -[\tilde{\boldsymbol{\omega}}]\boldsymbol{C_x} \\ -[\tilde{\boldsymbol{\omega}}]\boldsymbol{C_y} \\ -[\tilde{\boldsymbol{\omega}}]\boldsymbol{C_z} \\ \mathbf{V}_\mathbf{f} \\ -2\xi_1\omega_1 p_{act1} - \omega_1^2\left(q_1 - q_{c1}\right) \\ p_{act1} \\ -2\xi_2\omega_2 p_{act2} - \omega_2^2\left(q_2 - q_{c2}\right) \\ p_{act2} \\ . \\ . \\ . \end{pmatrix} \tag{4.52}$$

In Eq. (4.52), V_f and ω are the velocities (translational and angular) of the body frame, C_x, C_y, and C_z are the columns of the rotation matrix, X is the origin of the body frame, and q_i and p_i are the displacements and rate of displacements of the various actuators. The commanded actuator states $\{q_{ci}\}$ are represented by the

control input vector u. The Poisson Kinematic Equation (PKE) is used for rotational kinematics. As a consequence, no singularities are introduced. A small CPU time penalty is incurred, however. The number of actuator equation pairs is variable, and it depends on the specific aircraft. Finally, thrust dynamics are handled as an actuator (one per engine).

4.4.1 Integration of the Non-Linear ODE System

The equations of motion (Eq. (4.52)) are integrated using a Runge-Kutta Merson (RKM) algorithm [27]. The RKM algorithm provides a truncation error of integration that scales with the Δt^4 (as does the standard Runge-Kutta algorithm), but it also computes an error estimate for the truncation error. The error estimate is used for the adaptive timestep algorithm (illustrated in Fig. 4.2). The timestep is adjusted to keep the truncation error in each step below a user-specified threshold. If the estimated error on a given time point exceeds the tolerance parameter, the time point is rejected and repeated with a smaller timestep. On the other hand, if the error is significantly smaller than the user-defined tolerance threshold, the timestep is increased. This results in greatly improved CPU efficiency, since large time steps can be used during portions of the trajectory with gradual changes to the state vector. The variation in the truncation error and timestep is illustrated in Fig. 4.3. It is evident from Fig. 4.3 that the timestep changes by nearly two orders of magnitude over the course of the trajectory. Thus, if a fixed timestep had been used instead, the simulation runtime would increase by two orders of magnitude as well, if the truncation error tolerance were unchanged.

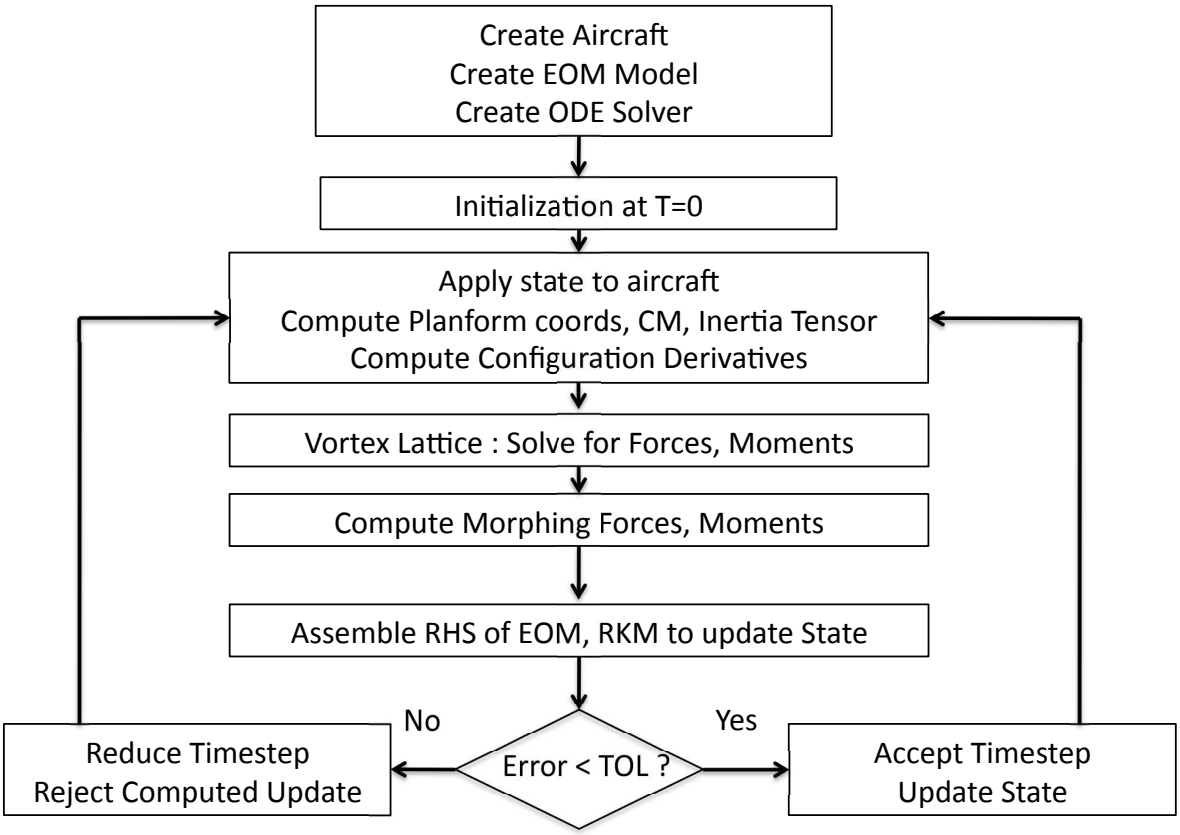

Figure 4.2. Overall simulation flow with error estimation.

4.4.2 Trim-Point and Linearization

A key method in the analysis of the flight dynamics is the linearization of the system around a given trimpoint. The simulation framework provides this capability through the TrimSolver and Linearizer classes. The starting point for the analysis is the nonlinear system of equations for the state evolution, and the observed quantities:

$$\dot{\mathbf{x}} = \mathbf{F}(\mathbf{x}, \mathbf{u}(t)) \tag{4.53}$$

$$\mathbf{y} = \mathbf{H}(\mathbf{x}, \mathbf{u}(t)) \tag{4.54}$$

The trimpoint is defined as a point in state space where the dynamics portion of the RHS vector of Eq. (4.53) vanishes. Thus, the body frame linear and angular velocity vectors are constant. Therefore, trimming can be represented as a minimization

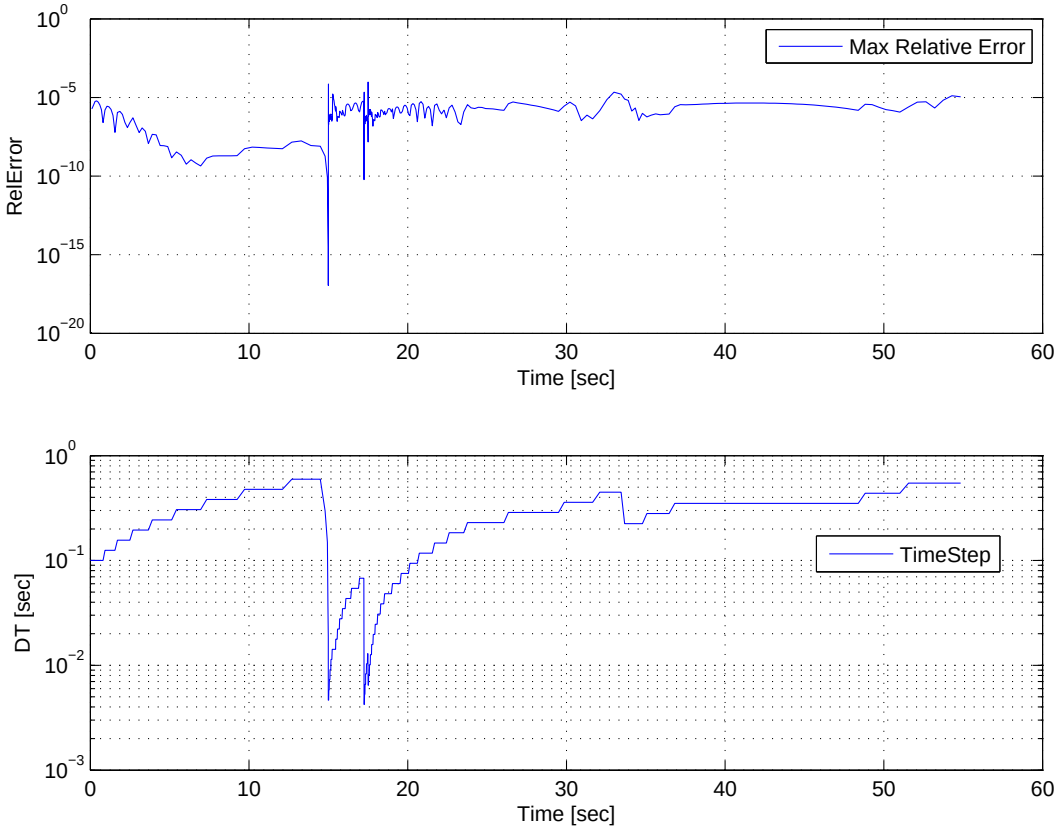

Figure 4.3. Relative error and Δt at each time step.

problem in which the six dynamic quantities are driven to zero, while the kinematic variables are set to desired values. The inputs to the minimization problem are then the target actuator states. If the number of inputs is equal to or greater than the number of free outputs, the minimization results in an exact solution (assuming the desired trim point is physically consistent), and linearization can proceed.

Linearlization is performed on Eq. (4.53) around a computed trimpoint x^* by performing a Taylor expansion of the RHS of (4.53) around the trimpoint. Thus, we have:

$$\begin{aligned} \boldsymbol{\Delta}\dot{\mathbf{x}} &= \mathbf{F}(\mathbf{x}^* + \boldsymbol{\Delta}\mathbf{x}, \mathbf{u}^* + \boldsymbol{\Delta}\mathbf{u}) \\ &\approx \mathbf{F}(\mathbf{x}^*, \mathbf{u}^*) + \nabla_x \mathbf{F}(\mathbf{x}, \mathbf{u})|_{\mathbf{x}^*, \mathbf{u}^*} \cdot \boldsymbol{\Delta}\mathbf{x} + \nabla_u \mathbf{F}(\mathbf{x}, \mathbf{u})|_{\mathbf{x}^*, \mathbf{u}^*} \cdot \boldsymbol{\Delta}\mathbf{u} \end{aligned} \tag{4.55}$$

Since the RHS of Eq. (4.53) vanishes, the linearized system is obtained:

$$\boldsymbol{\Delta}\dot{\mathbf{x}} = [\mathbf{A}]\boldsymbol{\Delta}\mathbf{x} + [\mathbf{B}]\boldsymbol{\Delta}\mathbf{u} \tag{4.56}$$

where the matrices $[\mathbf{A}]$ and $[\mathbf{B}]$ in Eq. (4.56) are obtained as:

$$[\mathbf{A}]_{ij} = \frac{\partial \mathbf{F}_i}{\partial x_j} \ , \ [\mathbf{B}]_{ij} = \frac{\partial \mathbf{F}_i}{\partial u_j} \tag{4.57}$$

Likewise, the linearized output response is obtained from the Taylor expansion of Eq. (4.54) as:

$$\mathbf{y} = [\mathbf{C}]\boldsymbol{\Delta}\mathbf{x} + [\mathbf{D}]\boldsymbol{\Delta}\mathbf{u} \tag{4.58}$$

where the matrices $[\mathbf{C}]$ and $[\mathbf{D}]$ in Eq. (4.58) are computed as:

$$[\mathbf{C}]_{ij} = \frac{\partial \mathbf{H}_i}{\partial x_j} \ , \ [\mathbf{D}]_{ij} = \frac{\partial \mathbf{H}_i}{\partial u_j} \tag{4.59}$$

The Linearizer class performs the numerical differentiation of Eq. (4.57) using adaptive-step central differencing. The step size used in the finite differencing for each state or input is reduced by a factor of two at each iteration, until the resulting matrix column changes by less than a pre-defined tolerance. The algorithm then proceeds to the next state / column. Once the matrices A and B of Eq. (4.56) and C and D of Eq. (4.58) have been obtained, the standard tools of linear system analysis can be applied.

4.4.2.1 Example: Linearization of Symmetric Gull-Wing at Cruise

As an example of linearization, the full step-response of the open-loop system is illustrated in Fig. 4.4. The inputs are the desired actuator changes (i.e., Δu for the full set of actuators - wing morphing angles, ruddervon angles, and thrust). The outputs are the standard body frame variables: body frame linear and angular velocities and the Euler angles. Note that the latter are not part of the state vector but are instead computed by an OutputFunctor object.

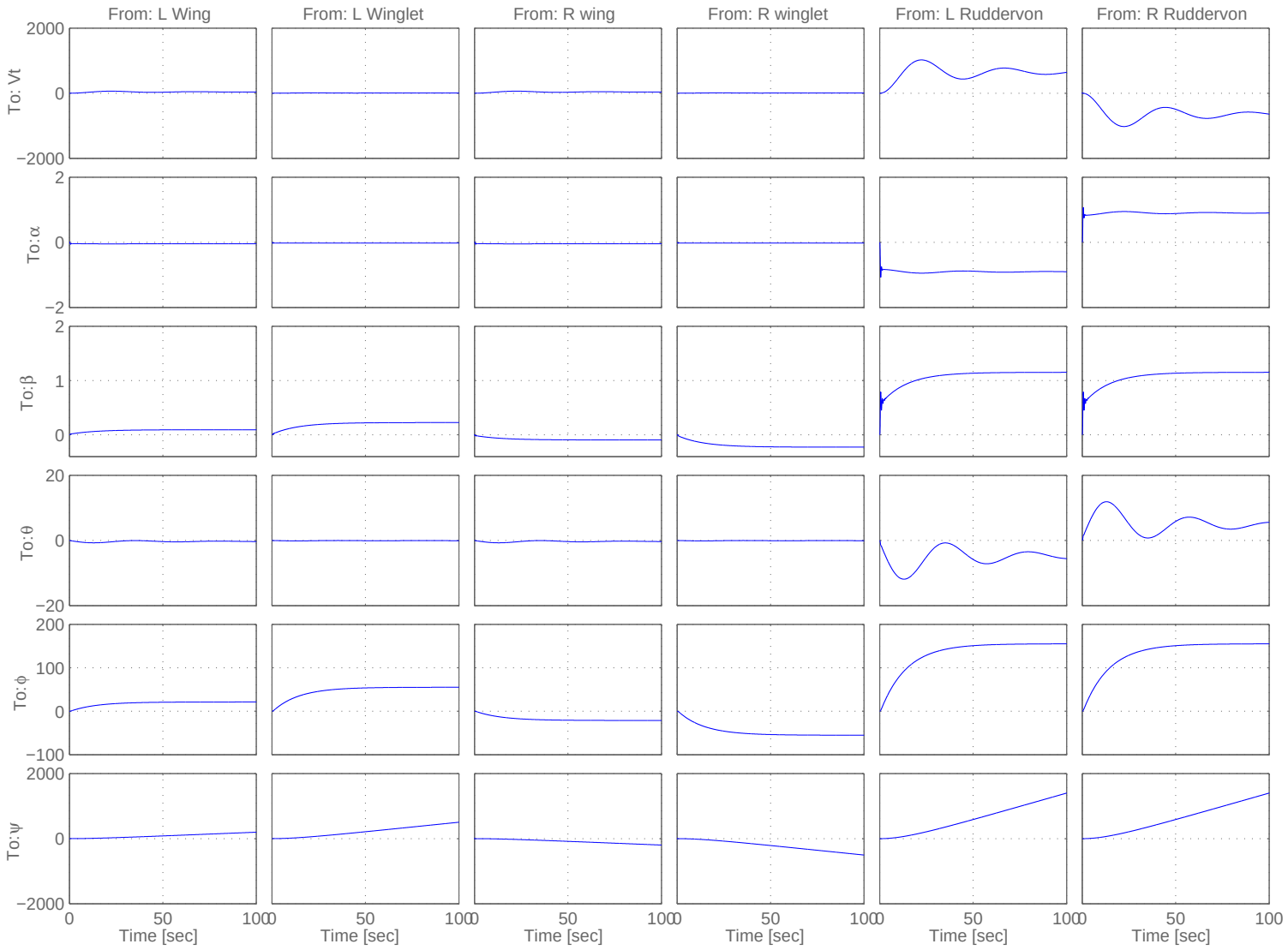

Figure 4.4. Open-loop, linearized step response of the gull-wing aircraft

Table 4.2. Open-loop modes of the gull-wing aircraft

Type	Name	$Re\{\omega\}$ rad/sec	$Im\{\omega\}$ rad/sec
Longitudinal	Short-Period	-2.595	7.68
	Phugoid	-0.025	0.141
Lateral	Dutch-Roll	-1.44	7.78
	Roll Subs.	-2.66	
	Spiral	-0.072	

Analysis of the eigenvalues of the open-loop system leads to the classification of modes summarized in Table 4.2.

4.4.3 LQR Controller for Linearized Dynamics

A simple LQR-based controller is designed next to augment the aircraft stability, and to control the outputs $\{V_T, \alpha, \beta, \theta, \phi, \psi\}$ to a commanded value. This is accomplished by creating an OutputFunctor object which computes the non-linear output based on the state vector:

$$\mathbf{X_{output}} = \mathbf{H}(x) \tag{4.60}$$

where $H(x)$ computes the desired output variables. The C matrix is then derived from the output functor as per Eq. (4.59). The Q matrix for the LQR performance index is (for this example) created using:

$$[\mathbf{Q}] = q_{sc}[\mathbf{C}]^{\mathbf{T}}[\mathbf{C}] \tag{4.61}$$

where q_{sc} in Eq. (4.61) is a scaling factor, adjusted to give reasonable results. The R matrix in the LQR performance index is chosen as:

$$[\mathbf{R}] = \begin{pmatrix} r_w[\mathbf{I}]_{4\times4} & \\ & r_r[\mathbf{I}]_{2\times2} \end{pmatrix} \tag{4.62}$$

where r_w and r_r in Eq. (4.62) are scaling factors for wing angle and ruddervon angle penalization, respectively. The resulting behavior of the controlled system (after some adjusting of the scaling values) is illustrated in Fig. 4.5.

As can be seen from Fig. 4.5, the LQR controller is indeed able to achieve the steady-state target kinematic states. It is to be noted, however, that the time history of the angles such as α, β, and θ shows considerable oscillation prior to settling at the steady-state value. In fact, the initial motion of these states is opposite to that commanded by the inputs. This is not an artifact of the control system, but is in fact a consequence of the morphing forces and moments, discussed in 4.4 and 4.1.2. The complete effect of the morphing forces and moments is described in detail in chapter 5.

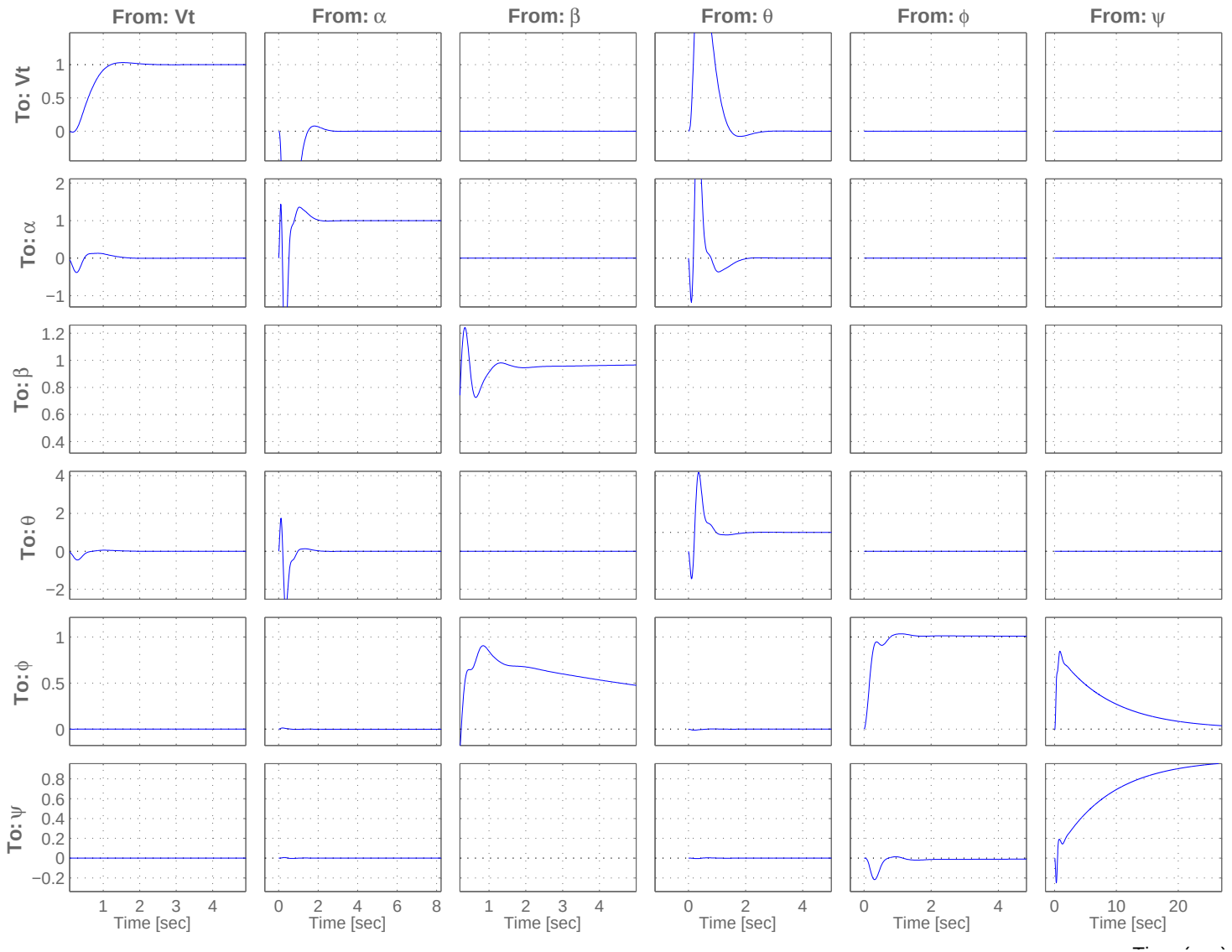

Figure 4.5. Step-response of an LQR-controlled linearized aircraft system

CHAPTER 5

SIMULATION RESULTS

5.1 Overview

The full set of tools provided by the framework is brought to bear on simulating the behavior of the gull-wing aircraft. Specifically, the dynamic behavior during morphing-induced turn is studied. The analysis begins with static ("wind-tunnel") simulation to anticipate the aerodynamic forces and moments during the turn. The frequencies of the aircraft longitudinal and lateral modes are next analyzed (near the trim point), as functions of the morphing state. Finally, full non-linear simulation of the turns is performed. Two types of morphing turns are studied: asymmetric and anti-symmetric. The reference (initial) configuration of the aircraft is illustrated in Fig. 5.1. Two rotational joints are used for each half of the main wing, with the wings raised above the fuselage ($\approx 30^\circ$ angle at the wing root, set by trim condition at desired airspeed). This is the high-speed cruise configuration. Both lift and drag are reduced relative to the flat wing state. The upward-V ruddervons are used for both longitudinal and yaw stability. The downward-pointing vertical stabilizer is fixed. In Fig. 5.1, the blue streamlines indicate the flowfield around the aircraft, while the red arrows on the planforms illustrate the local aerodynamic forces. Force magnitudes are normalized, but the relative magnitudes are preserved.

5.2 Asymmetric Turn

The asymmetric turn begins with the aircraft in the symmetric-gull-wing configuration, as shown in Fig. 5.1 (for high-speed cruise). One of the wings is then

partially or fully "flattened" (as illustrated in Fig. 5.2). This asymmetry induces roll and yaw moments (as discussed in section 5.2.1) which induce a turn.

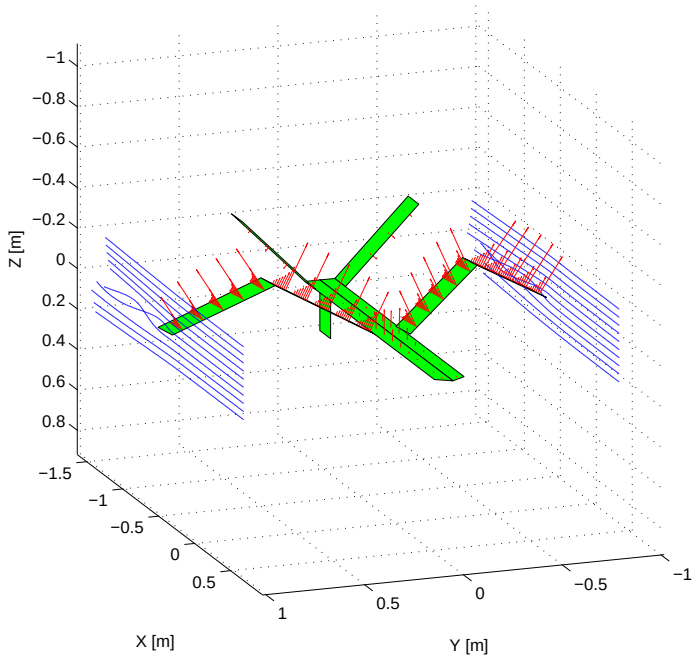

Figure 5.1. Reference gull-wing configuration.

5.2.1 Static Analysis

It is evident from the forces illustrated in Fig. 5.2 that the asymmetry in the aerodynamic forces will result in a roll moment. The aerodynamic moments are illustrated in Fig. 5.3. This is simply due to the reduction of the vertical component of the aerodynamic forces on the gull-wing, which is not present in the flat wing. In addition to the roll moment, Fig. 5.2 also indicates the presence of a yaw moment. The yaw moment arises due to a combination of morphing and wing sweep. The right wing, which remains "V" shaped, has Y-directed force components, as can be seen from Fig. 5.2. The two portions of the wing thus contribute oppositely directed

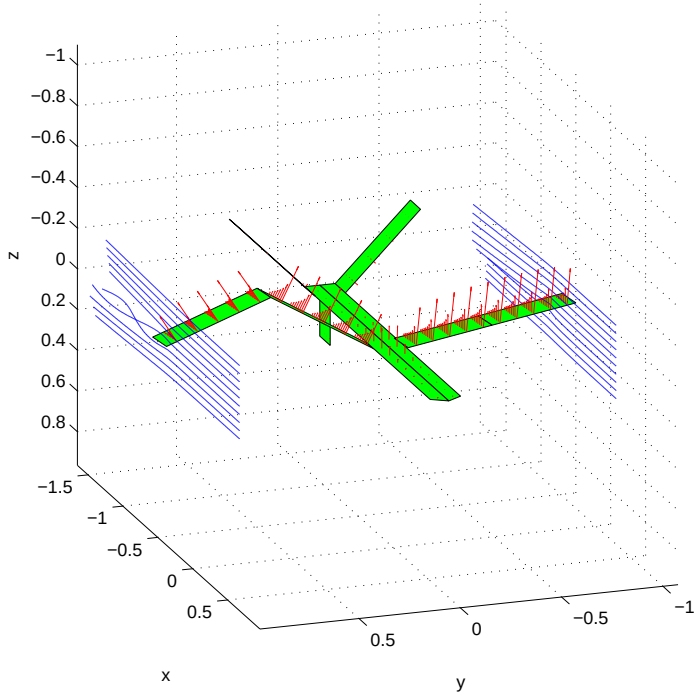

Figure 5.2. Asymmetric gull-wing configuration.

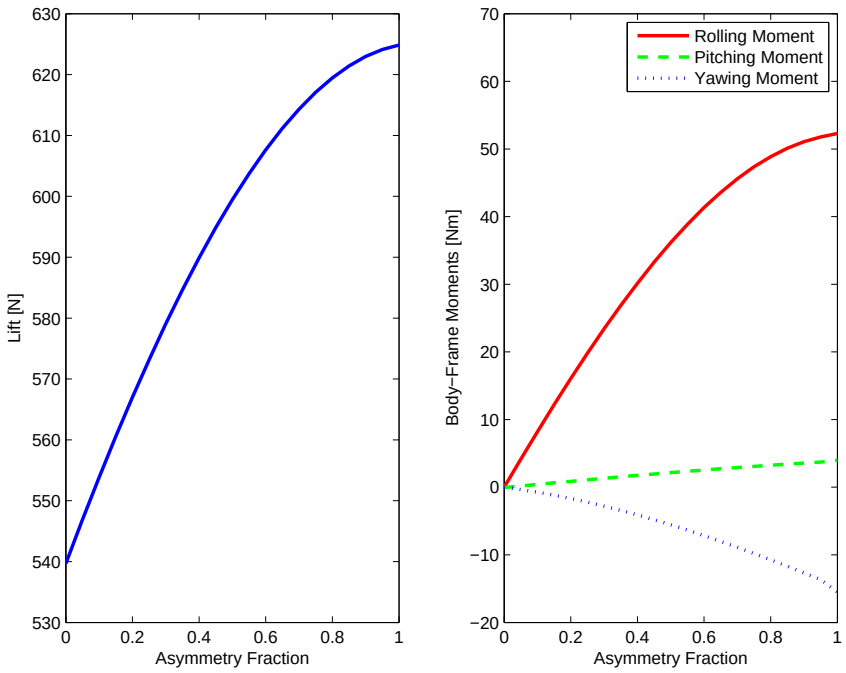

Figure 5.3. Behavior of lift and moments as a function of the wing asymmetry.

yaw moments around the CM, but the outer wing has a larger moment arm (due to wing sweep), and the overall yawing moment is therefore negative. The yawing moment tends to turn the aircraft counter to the induced roll, which creates a positive slip angle. Thus, without ruddervon inputs, we expect the initial yaw motion of the aircraft to be "nose-left," while the roll is to the right. As the slip angle β becomes positive, however, a stabilizing yawing moment from the ruddervons and the vertical tail is expected to keep the sideslip angle in check. Finally, the increased lift of the left wing also leads to a positive pitching moment, since the ruddervons were trimmed to compensate for the lift of the symmetric gull-wing. Thus, an initial pitch-up tendency is expected as well.

5.2.2 Flight Simulation

Having established the expectations for the aerodynamic forces on the asymmetric gull-wing in the previous section, we now turn to the full, non-linear flight simulation of a morphing-induced turn. The starting configuration in this maneuver is the symmetric gull-wing, shown in Fig. 5.1. The gull-wing angle, ruddervon angle, and thrust are trimmed to provide level flight at 90 m/s. At this airspeed, the wings provide sufficient lift at a gull-wing angle of $\approx 30°$. At t=15s, the turn maneuver is initiated by "flattening" the left wing; the left gull-wing angle is reduced to $0°$. The time dependence of the wing angles is shown in Fig. 5.5. This is driven puerly by the actuator response to the commanded inputs, as are the CM motion and inertia tensor (as shown in Figs. 5.6 and 5.7). As discussed in the previous section, rolling, yawing, and pitching aerodynamic moments are all induced by this maneuver. Additionally, morphing moments M_1 through M_4 must be considered in the analysis.

The overall behavior of the aircraft during the turn is illustrated in Figs. 5.4 and 5.9. The angular velocity exhibits the expected spike in roll, induced largely by

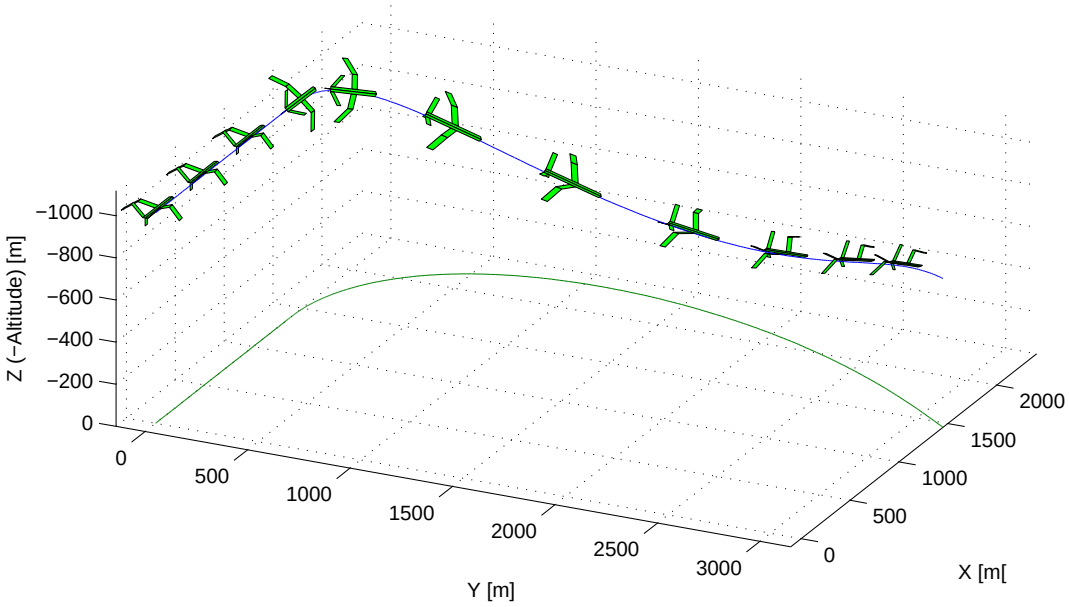

Figure 5.4. Turning trajectory induced by asymmetric wing morphing.

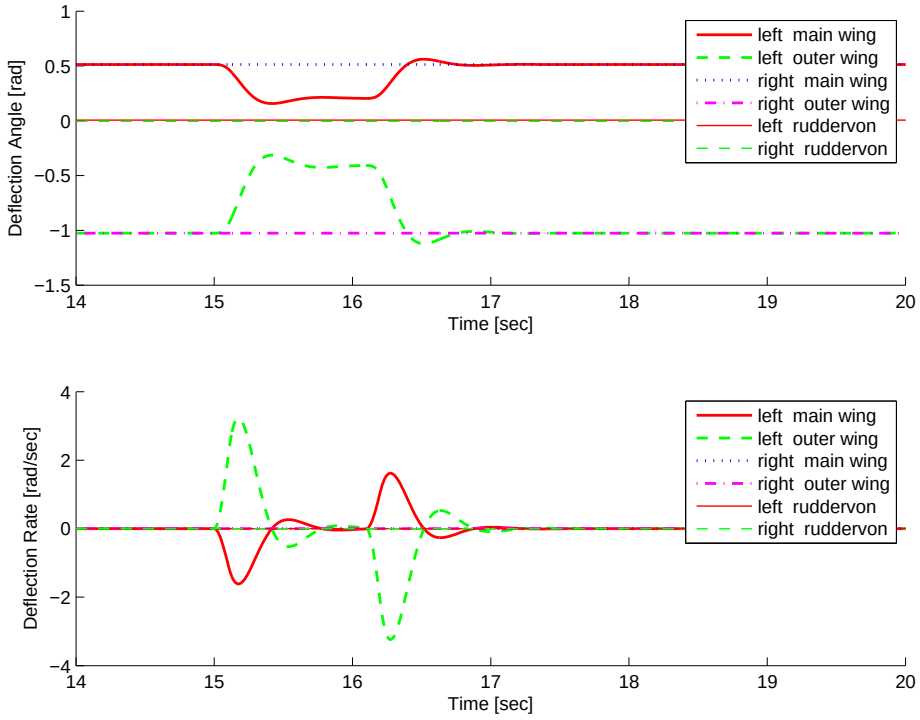

Figure 5.5. Time dependence of the morphing angles.

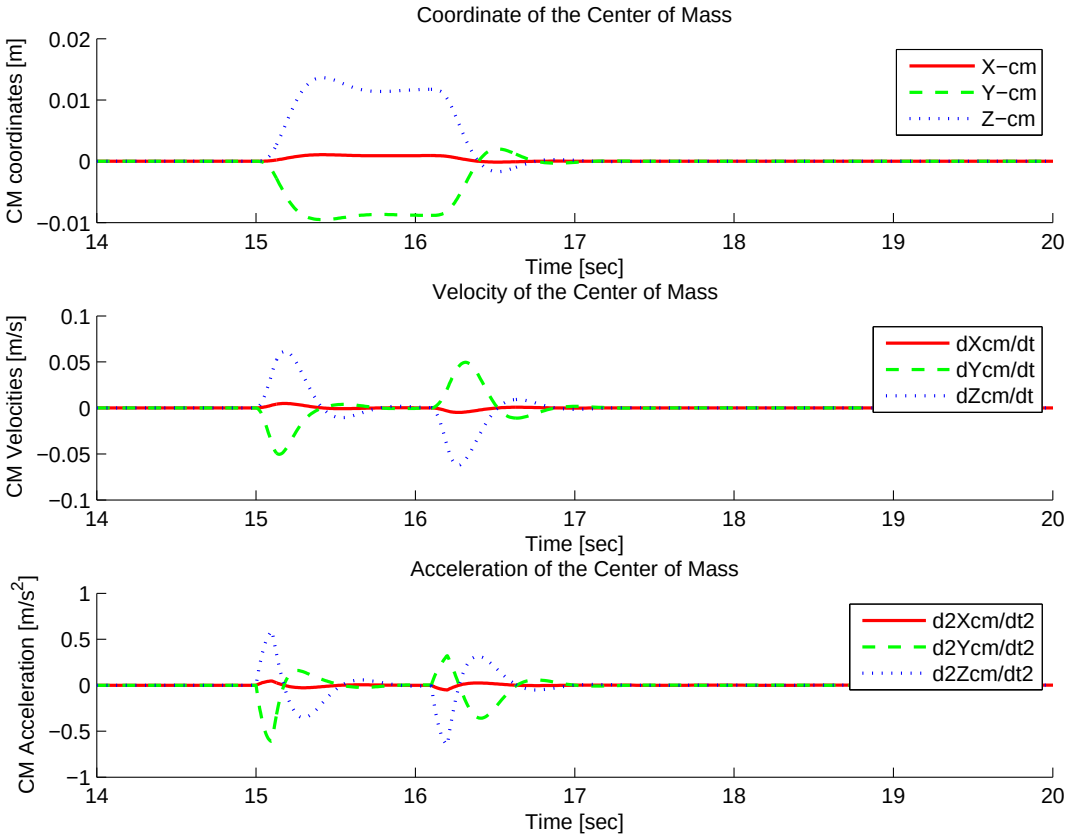

Figure 5.6. Position, velocity, and acceleration of the CM.

aerodynamic moments. Additionally, the α and β angles both increase, as expected, due to the aerodynamic pitch and yaw moments. However, the fine detail of the motion hints at additional contributions. Indeed, the morphing moments for this configuration are non-negligible, as evidenced in Fig. 5.8. While the pitch and yaw moments are dominated by the aerodynamic contributions, a significant contribution to the roll moment comes from the morphing moments themselves. We can see that the M_4 moment, in particular, is quite significant. Since the M_4 moment is governed by the acceleration of the morphing mass elements in the body frame, it is not surprising that the moment is greatest at the beginning and end of morphing. While the peak moment magnitude is large, the overall effect is somewhat muted by

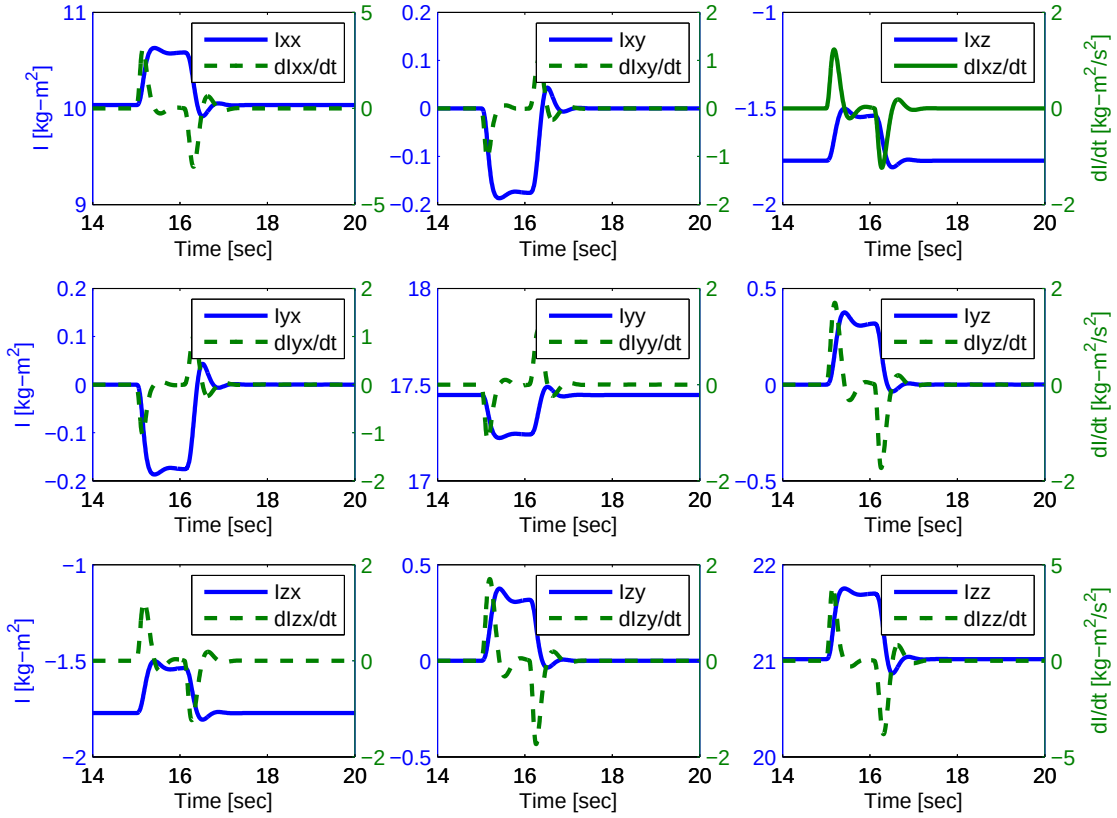

Figure 5.7. Inertia tensor and its temporal derivative.

the fact that a positive moment spike at the onset of morphing is immediately followed by a negative spike at the conclusion of morphing. Thus, the overall behavior of the aircraft in the asymmetric turn is primarily determined by the aerodynamic forces and moments in the hold time between morphing events.

The qualitative behavior of the M_1 and M_4 moments is seen to be in agreement with expectation. As the left wing begins to flatten, it is "rolling down" in the body frame. This produces an instantaneous moment opposing the motion so as to conserve angular momentum, M_4. However, opposing the roll-down of the left wing means rolling the body frame to the right, so that the initial M_4 rolling moment actually aids the turn. It will counter the turn as the morphing comes to an end, helping to stop the roll. The M_1 moment is preserving the angular momentum of a

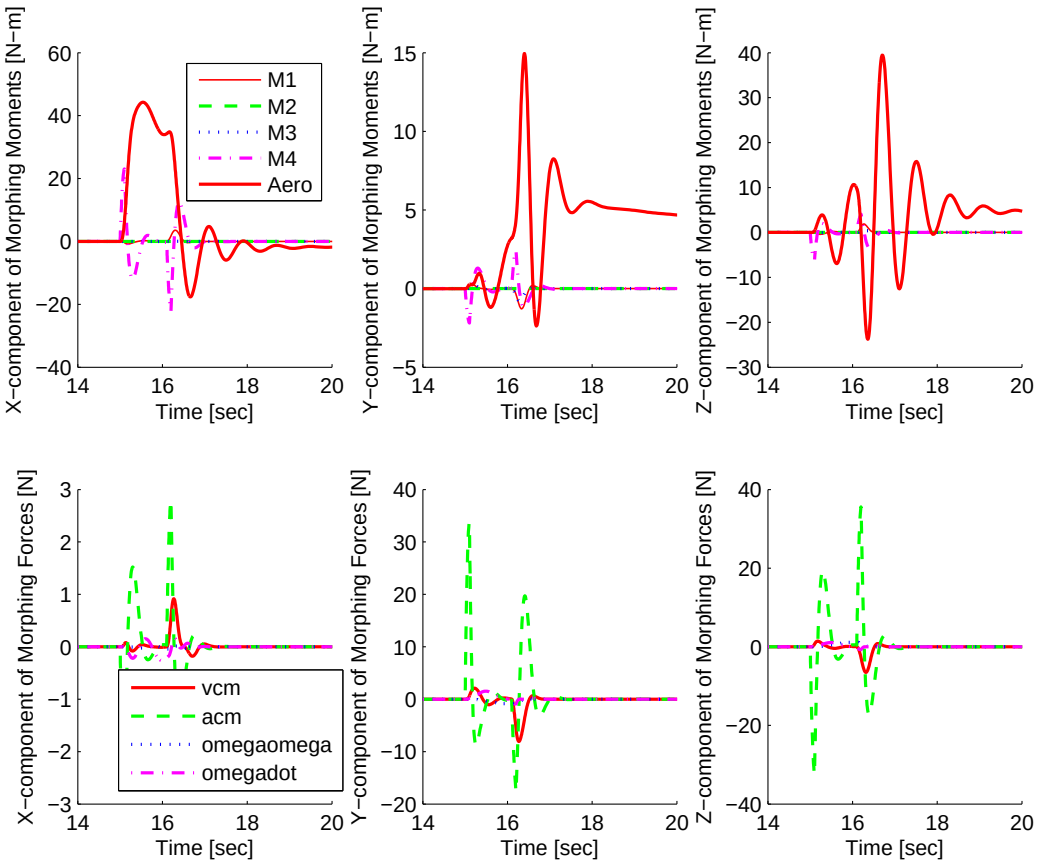

Figure 5.8. Comparison of the morphing and aerodynamic moments.

rotating body whose inertia around the rotation axis is changing. Thus, it somewhat lags behind M_4, since the initial angular velocity is zero, and it is governed by the 1^{st} (but not 2^{nd}) derivative of morphing. M_1 acts in a direction that initially opposes the turn, then tries to continue it as the morphing ends. Thus, M_1 is at all times countering the control inputs. For this aircraft and maneuver, M_1 is quite small, and its influence is barely perceptible. These relative magnitudes of M_1 and M_4 are to be expected for a small UAV aircraft; the inertia tensor is small, but the accelerations of the morphing components are large. Morphing of a large aircraft would likely result in opposite behavior: a large inertia tensor and small accelerations.

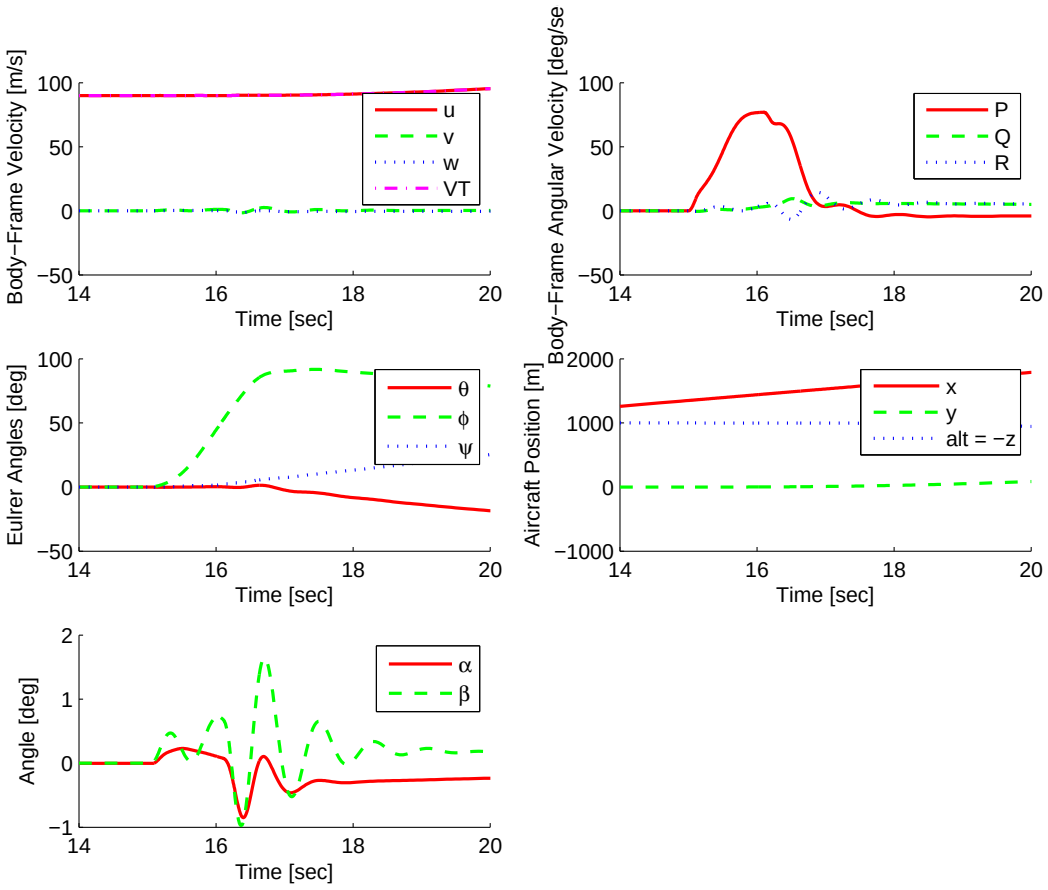

Figure 5.9. Full state of the aircraft during morphing.

The morphing forces, shown in Fig. 5.8, are also quite significant, primarily in the Y and Z directions. This is to be expected, since portions of the aircraft mass are accelerating within the body frame during morphing, resulting in the acceleration of the CM within the body frame. In order to preserve the instantaneous acceleration of the CM in the inertial frame, morphing forces are induced, as described by Eq. (4.15). Thus, we can see that as the left wing accelerates down and left in the body frame, the induced morphing forces are right and up (in the negative Z direction). The magnitudes are not negligible, being $\approx$ 10% of the aircraft weight. The X component of the morphing forces is much smaller, due to the minimal X-motion of the CM within the body frame. Finally, the morphing force induced by the velocity

of the CM (described by Eq. (4.16)), is considerably smaller than that induced by the acceleration of the CM. This is in part due to the fact that the angular velocity in Eq. (4.16) is small during the initial part of the turn but is more pronounced at the end of morphing.

It should also be noted that the magnitude of the morphing forces and moments is in large part determined by the morphing rates. The most significant moments and forces are governed by the 1^{st} and 2^{nd} derivatives of the mass displacements, and we should therefore expect that actuator frequencies play a crucial role in determining the impact of the morphing moments and forces. This is illustrated in Figs. 5.10 and 5.11.

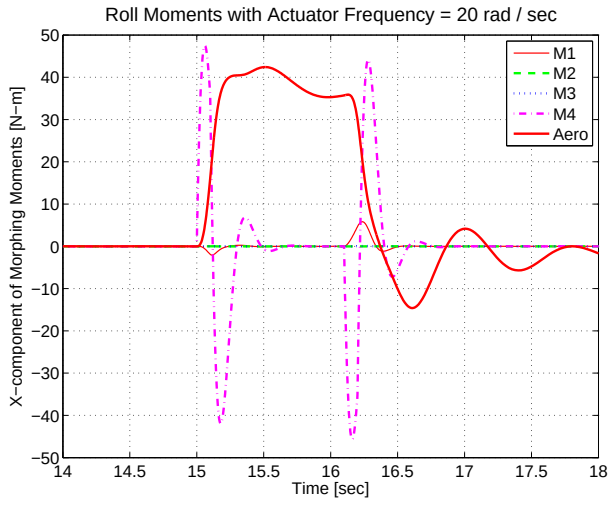

Figure 5.10. Morphing moments with actuator frequency $\omega = 20\ rad/s$.

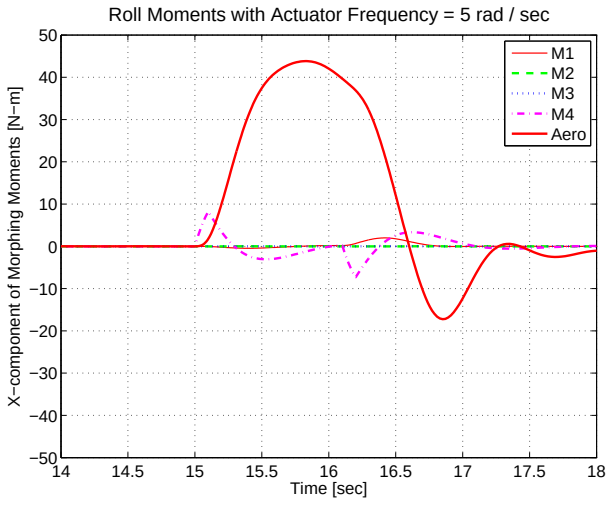

Figure 5.11. Morphing moments with actuator frequency $\omega = 5\ rad/s$.

The actuator frequencies of this aircraft are nominally set to $\omega = 20\ rad/s$ for modeling a "fast" actuator of a small UAV. The morphing (roll) moments for the fast actuator are shown in Fig. 5.10. If the actuator frequency is reduced to $\omega = 5\ rad/s$,

the simulation results (shown in Fig. 5.11) indicate a much smaller peak value of the morphing moments. The aerodynamic moment is only slightly changed, since it depends primarily on the instantaneous position, and to a lesser extent, on the velocity. In both cases, the commanded input was to transition from the symmetric to the asymmetric state in 0.1s. The actual rate is thus determined by the actuator response times.

5.2.3 Dynamic Loads and Power

The behavior of the joint moments is best analyzed in three separate time epochs: the first 15 seconds before morphing, the 1.5 seconds of morphing, and the after-morphing remainder of the flight. Fig. 5.12 illustrates all three epochs, while Fig. 5.13 provides a closer view of the morphing epoch. From Fig. 5.12, it is evident that during the first 15 seconds (trimmed, level flight), aerodynamic forces are the only source of joint moments. The joint moments are symmetric, and the wing-fuselage moments are $\approx 4x$ larger than the wing-winglet moments (the aerodynamic loads and moment arm are each $\approx 2x$ at the wing root).

During the morphing epoch, the aerodynamic moments change dramatically. As the left wing flattens, the lift on it increases, resulting in a sharp rise in the left wing root moment (and to a lesser extent in the left wing-winglet moment). During this period, morphing-induced moments appear as well. While all terms from Eq. (4.41) contribute, the most significant are the terms involving the panel body frame accelerations (Q_{Panels}) and the acceleration of the body frame origin (Q_{CM}). The various joint moments are illustrated in Figs. 5.12 to 5.13. The abbreviations stand for Left and Right Wing-Winglet and Wing-Fuselage joints. The moment required to flatten the left wing is evident in Fig. 5.13 (most evident in Q_{Panels}). An initially negative moment is required to initiate the flattening, followed by a positive moment

to stop it. At the end of the morphing state, the opposite sequence takes place, with a positive moment initiating the return to the symmetric gull-wing configuration and a negative moment ending it (also most clearly seen in Fig. 5.13, Q_{Panels}). The dominant term in Eq. (4.41) driving this effect is the panel acceleration term. Also, we see in Fig. 5.13 the influence of inertial moments (Q_{CM}) on the right wing as well, in spite of the fact that it is not morphing. Particularly significant are the transverse acceleration (as the roll initiates) and the Y-direction motion of the CM (induced by the flattening of the left wing). Note that the effect is actually stronger on the right wing (which remains folded) than the left wing (which flattens). This is caused by the larger coupling of the folded wing into the lateral motion of the CM (by the time the Q_{CM} moment peaks, the left wing is fully flattened. Finally, as the morphing epoch ends and the wings are returned to the symmetric gull-wing configuration, the influence of the inertial moments becomes more significant (in Fig. 5.13 Q_{CM}) than at the onset of morphing; this is simply due to the increased velocity and (particularly) acceleration of the aircraft at this point in the trajectory (Figs. 5.9). Both V_f and $\dot{V}_f$ are increased, due to the post-morphing dive.

After the completion of morphing, only aerodynamic and inertial forces contribute to the joint moments. As can be seen in Fig. 5.12, the aerodynamic moments increase (become more positive, turning the wings upward). The actuator moments preventing the wing motion are negative for both wings as the aircraft velocity increases, as evidenced by the plot of "Total Joint Moments" (Fig. 5.12). The actuator moments during this epcoh can be understood intuitively; the aircraft is still executing a turn (even though morphing has ceased), the aerodynamic moments are pushing the wings toward the center of the turn (requiring a negative actuator moment to prevent that motion), while the inertial acceleration of the body frame (Q_{CM}) is bending the wings downward (requiring a positive actuator moment). Thus, the required actuator

moment during the non-morphing part of the turn is a balance between aerodynamic and inertial terms. The aerodynamic moment is dominant, but the net moment is significantly reduced during the turn relative to what would have been predicted by aerodynamic loading alone.

The inertial moments on the various joints Q_{CM} are evidently (Fig. 5.12) quite different during the post-morphing epoch, in spite of the fact that the acceleration of the body frame is a common term for all of them. Mathematically, the difference is caused by the coupling coefficients to the CM motion, or more specifically, how it projects onto the acceleration of the body frame origin. Physically, the behavior is clearly understood from the aircraft state during the turn. The bank angle remains large for most of the turn, while the wings are folded in the symmetric gull-wing configuration. This means the right wing and the left winglet are essentially parallel to the body-frame acceleration vector. Conversely, the left wing and right winglet are almost perpendicular to the acceleration vector (this is an exaggeration for the purpose of illustration; the actual difference in angles is not so pronounced). As a consequence, the moments required by the left winglet and right wing joint are reduced, relative to those of the left wing and right winglet.

Overall, the actuator moments are dominated by the requirement to counter aerodynamic forces, although morphing-induced moments during a turn are non-negligible. The analysis presented does not distinguish between moments provided by actuators vs. the structure itself. During non-morphing phases of flight, the aerodynamic and structural loads would likely be balanced by structural moments, not actuators. However, the goal in this work is to be able to compute the power requirement during morphing maneuvers. The power required for each joint can then be computed simply as:

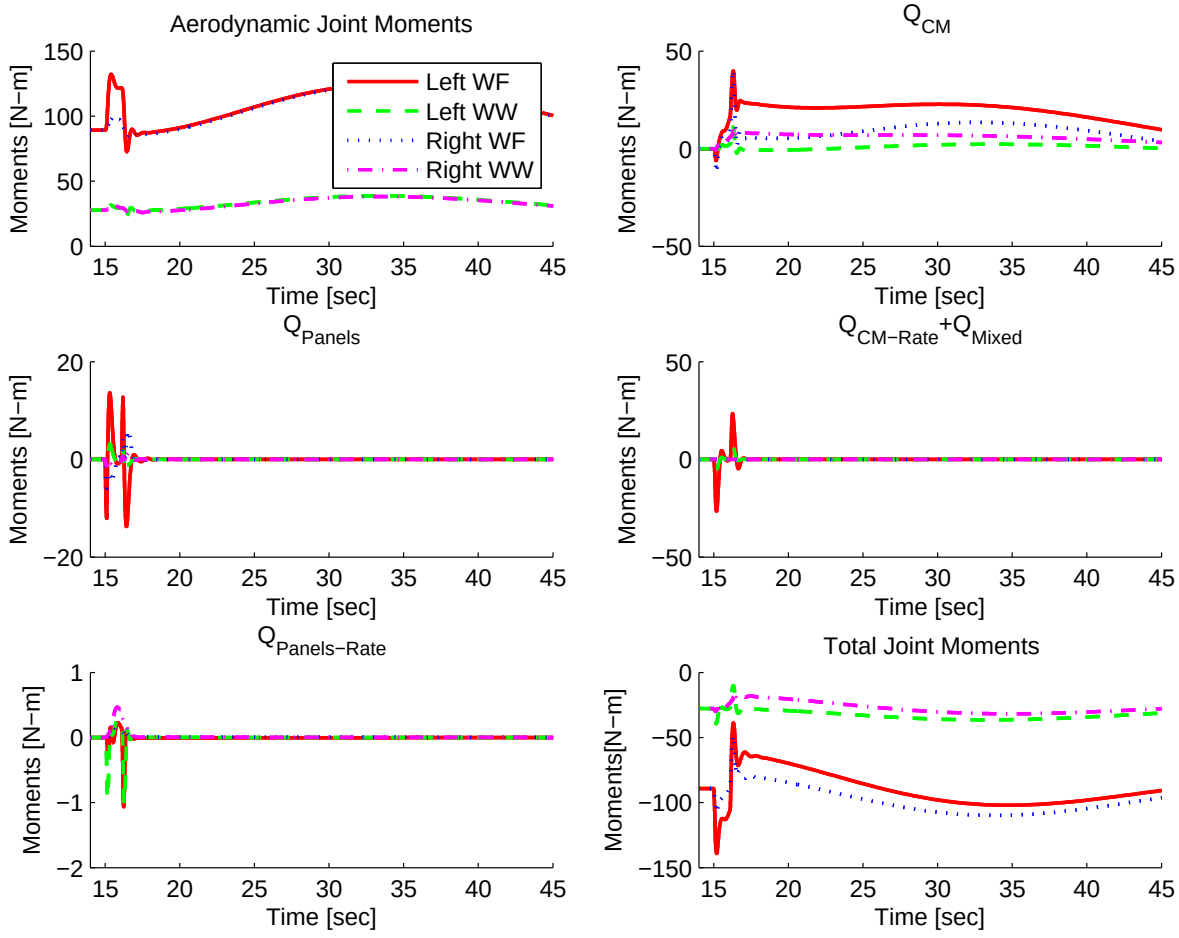

Figure 5.12. Joint moments during the first 45 seconds of the trajectory.

$$\frac{dW_i}{dt} = Q_i \dot{\theta}_i \tag{5.1}$$

where W_i is the energy expended by the i-th actuator. The actuator power required as computed in Eq. (5.1) is illustrated for the asymmetric turn in Fig. 5.14.

As can be seen from Fig. 5.14, only morphing joints do work. This is evident from Eq. (5.1). Also evident from Eq. (5.1) is that the power required will be negative when the joint moments are aligned in the same direction as the morphing displacement. However, special "regenerative" actuators would have to be devised

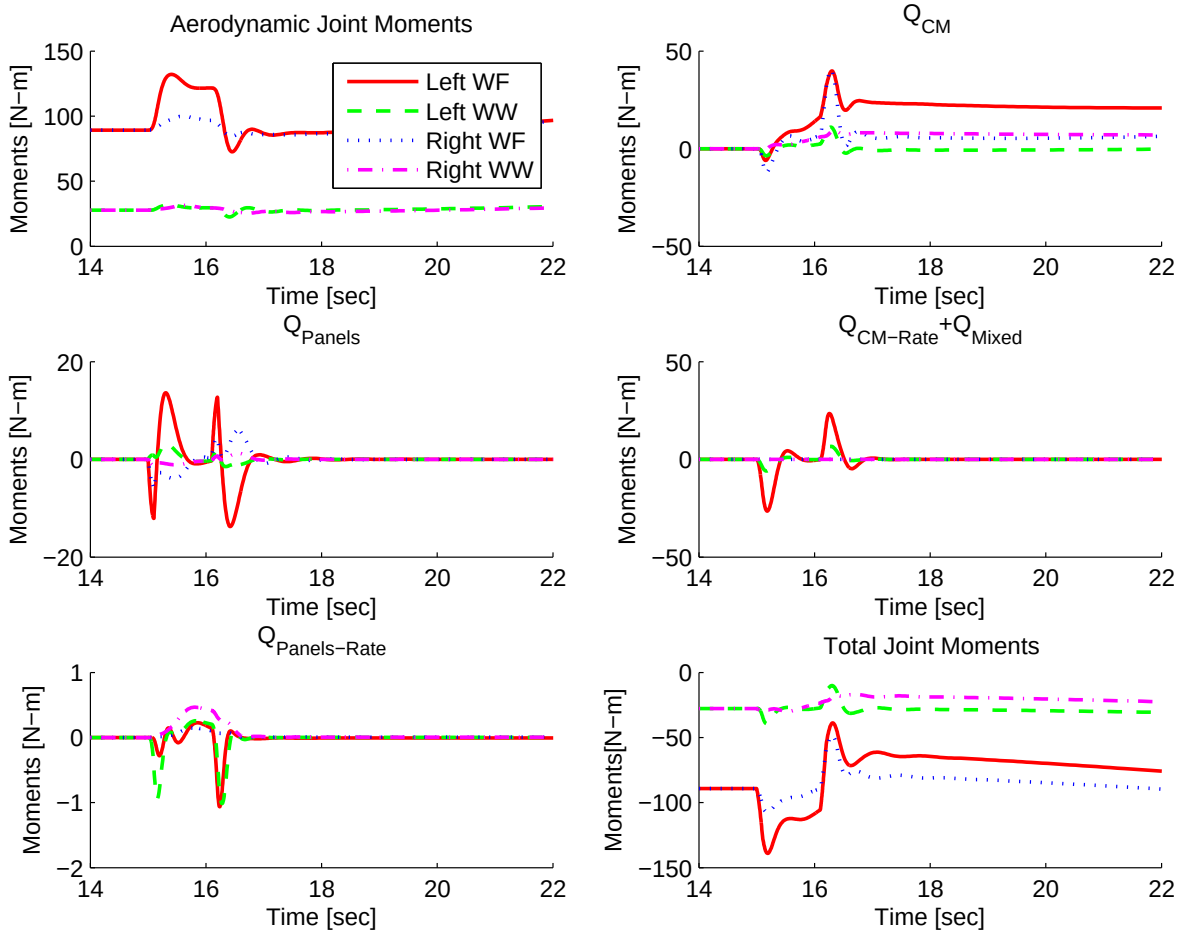

Figure 5.13. Joint moments during the morphing phase.

to harvest this energy. Thus, for typical joints, the energy consumed by the joints to perform the turn should be calculated by integrating the > 0 part of the power-required curve in Fig. 5.14.

Finally, it should be noted that the required joint power is clearly a function of the actuator frequencies. Higher frequencies result in higher morphing velocities which, in turn, result in larger joint moments. Additionally, the $\dot{\theta}$ term in Eq. (5.1) scales linearly with the actuator frequency. Thus, we can expect the aerodynamic contribution to the joint power required to scale with the actuator frequency, while

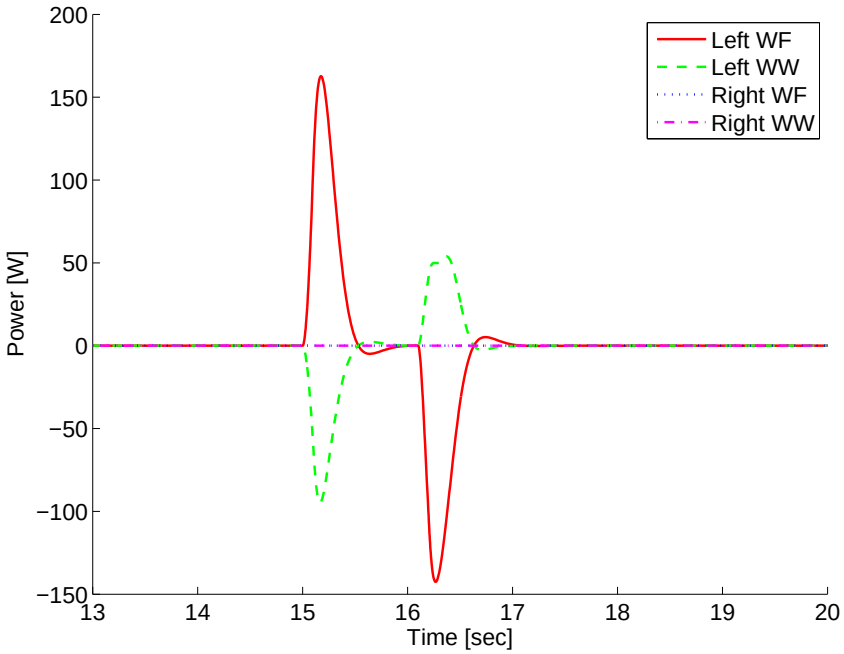

Figure 5.14. Required power for each of the wing joints.

the inertial and morphing terms scale with the 2^{nd} (velocity-dependent moments) and 3^{rd} (acceleration-dependent moments) power of the actuator frequency. The strong dependence of the required power is clearly visible in simulation, as illustrated in Figs. 5.15 and 5.16. Comparing the peak power required at 5, 10, and 20 rad/s in Figs 5.15, 5.1, and 5.16 respectively, it is clear that the power increase is super-linear. The departure from linearity is not stronger only because the dominant moment is the aerodynamic moment, which is independent of actuator frequency.

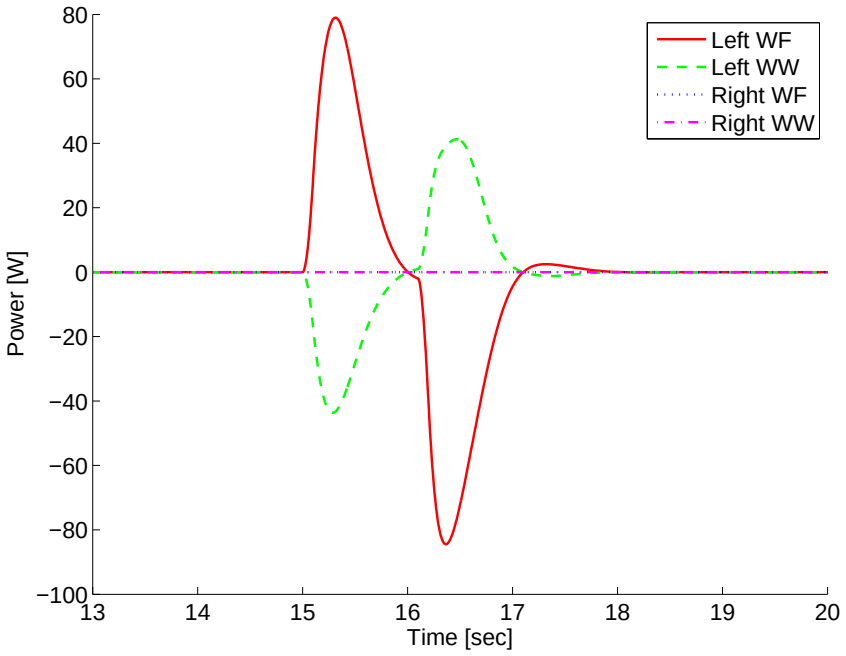

Figure 5.15. Required power for each joint with a joint frequency of 5 rad/s.

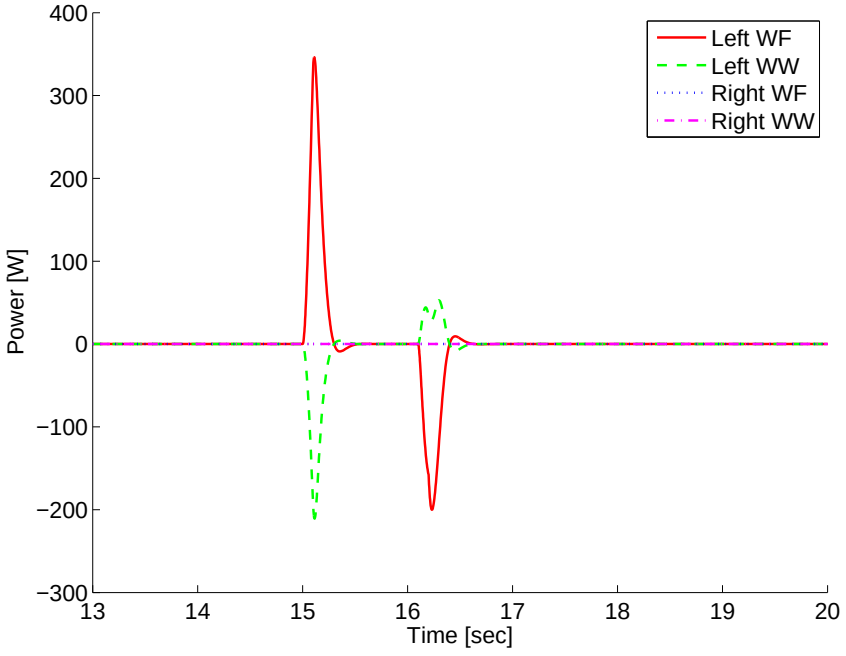

Figure 5.16. Required power for each joint with a joint frequency of 20 rad/s.

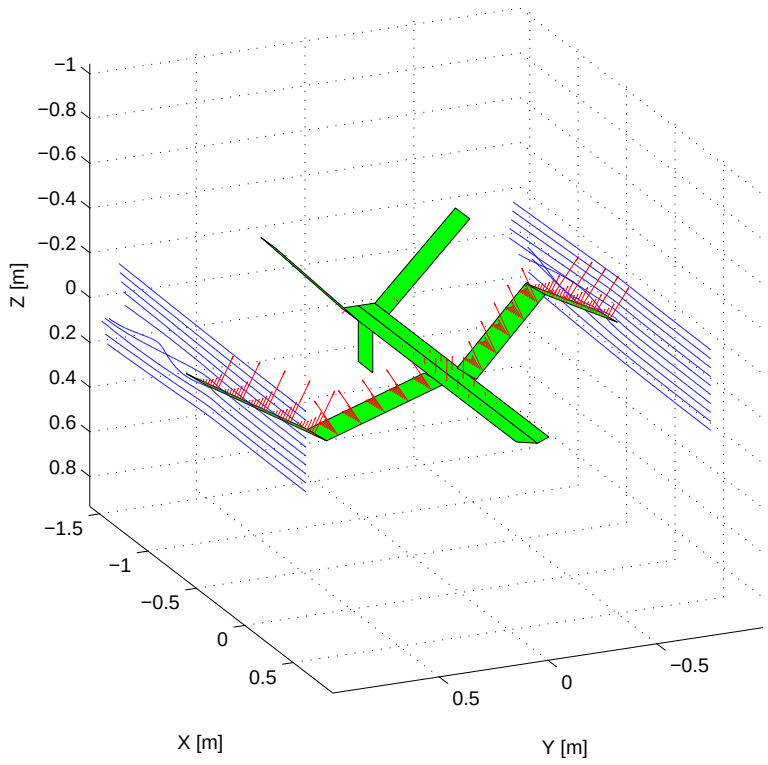

Figure 5.17. Anti-symmetric gull-wing configuration.

5.3 Anti-Symmetric Turn

Another interesting possibility for inducing a turn using morphing is the anti-symmetric wing morphing. The aircraft is assumed to start the maneuver in a flat-wing configuration, which is useful in a low-speed cruise. The right wing then morphs into a "V" shape, while the left morphs into an inverted "V." This results in an anti-symmetric wing arrangement, as shown in Fig. 5.17.

5.3.1 Static Analysis

Figure 5.17 illustrates the aerodynamic forces in the anti-symmetric wing configuration. The resulting lift and moments are shown in Figs. 5.18 and 5.19. The aircraft experiences a significant yawing moment and a smaller rolling moment. The yawing moment arises due to a combination of the wing sweep, anti-symmetric wing

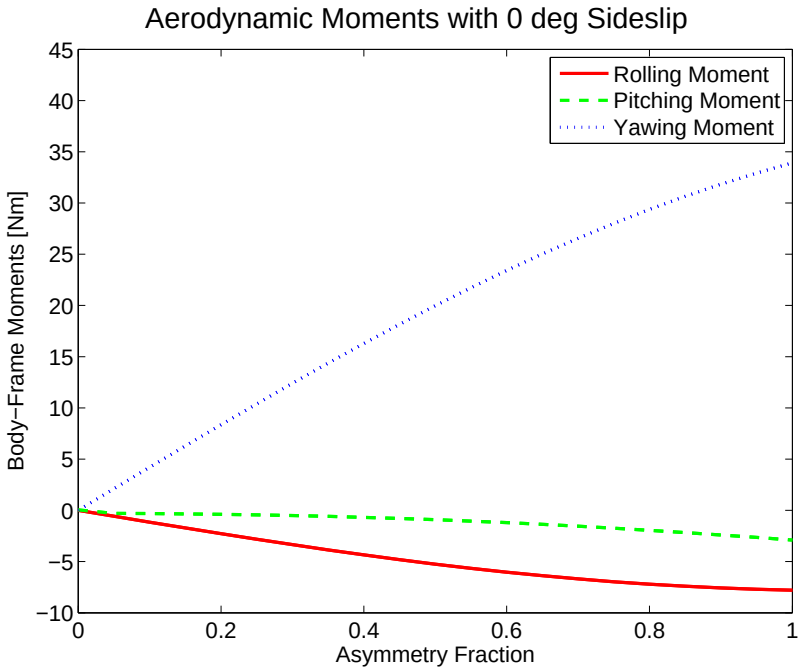

Figure 5.18. Aerodynamic moments as a function of the anti-symmetry.

folding, and position of the CM. From Fig. 5.17, it can be seen that the forces acting on the outer wing surfaces have a positive Y component, whereas the inner panels have a negative Y component. Furthermore, the resultant of the inner panels is in front of the CM, while the resultant of the outer panels is behind it. Thus, a moment is generated around the CM. We can therefore expect the initial yaw moment during the turn to induce a negative sideslip angle. With negative sideslip, the positive yaw moment of the anti-symmetric wing is competing with the negative yaw moment induced by the tail.

In addition to the yaw moment, a roll moment is induced. The roll moment arises due to the asymmetric placement of the CM w.r.t the wings in the anti-symmetric configuration. The CM is located at the midpoint of the wing planforms, slightly below the center of the fuselage planform. The resultants of the forces on each wing segment are approximately at the center of each segment. Due to this

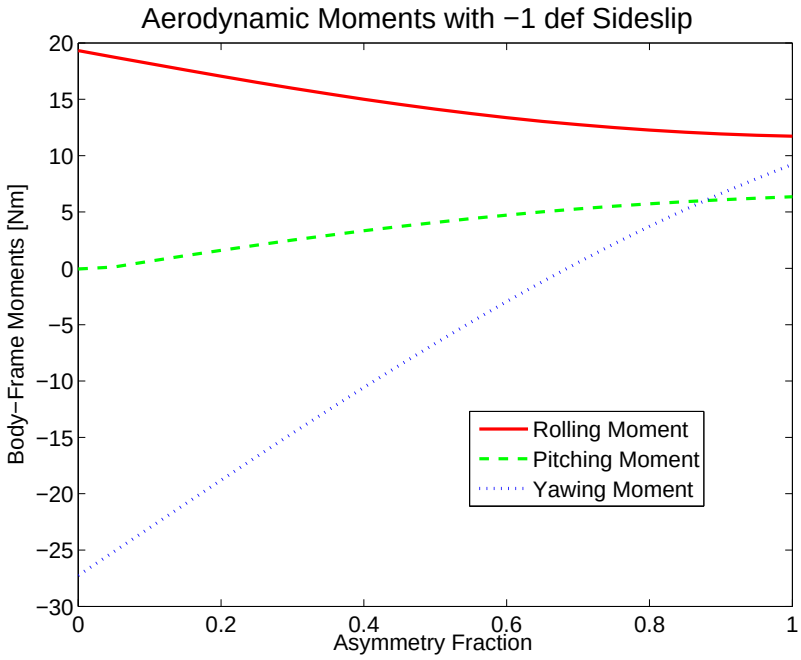

Figure 5.19. Aerodynamic moments with $\beta = -1°$.

arrangement, the moment arm from the CM to the right outer wing section is slightly smaller than the moment arm to the left outer wing section. With the forces being equal, a slight negative roll moment results. However, the roll moment is actually negative only for very small slip angles. As the sideslip angle increases to $-1°$ or more (negative), the roll moment becomes positive. This is simply the swept-wing effect, with the lift of the leading wing increasing.

5.3.2 Flight Simulation

The flight trajectory induced by the anti-symmetric turn is illustrated in Fig. 5.20. The actuator displacements during the morphing portion of the trajectory are illustrated in Fig. 5.21. The behavior of the inertia tensor is shown in Fig. 5.22. As in the case of the asymmetric turn, we expect that morphing moments will play a significant role in the behavior of the aircraft. Indeed, we can see from Fig. 5.23

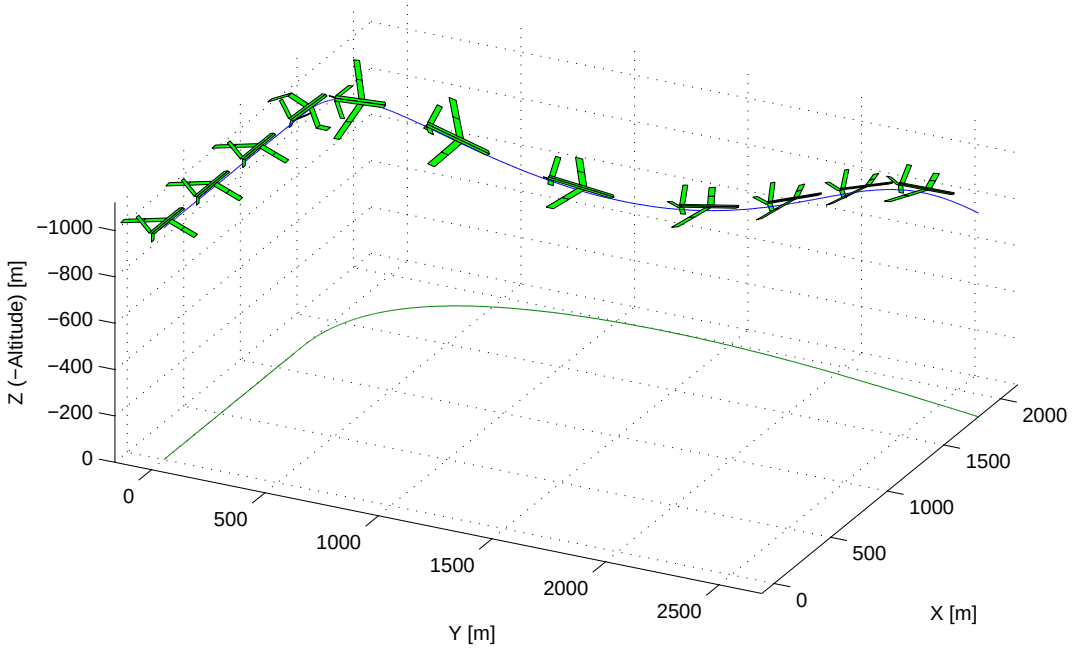

Figure 5.20. Trajectory of the aircraft performing an anti-symmetric turn.

that morphing moments M_4 and M_1 are non-negligible. M_4, in particular, is very significant, actually peaking above the aerodynamic moment. As expected, however, the morphing moments are present only during morphing. As in the asymmetric case, the morphing moments primarily impact the roll; the pitch and yaw morphing moments are almost negligible.

The behavior of the morphing roll moment can be understood intuitively as follows: as the wings fold from the flat configuration into the anti-symmetric gull-wing, they induce an intra-body frame angular momentum. In order to conserve the instantaneous inertial-frame angular momentum, the body frame must roll in the opposite direction. This conservation of angular momentum manifests as the M_4 moment. Note that the initial M_4 moment is actually directed opposite to the subsequently induced aerodynamic moment. Thus, the body frame actually initially rolls away from the desired turn, as can be seen in Fig. 5.24. The roll angle initially

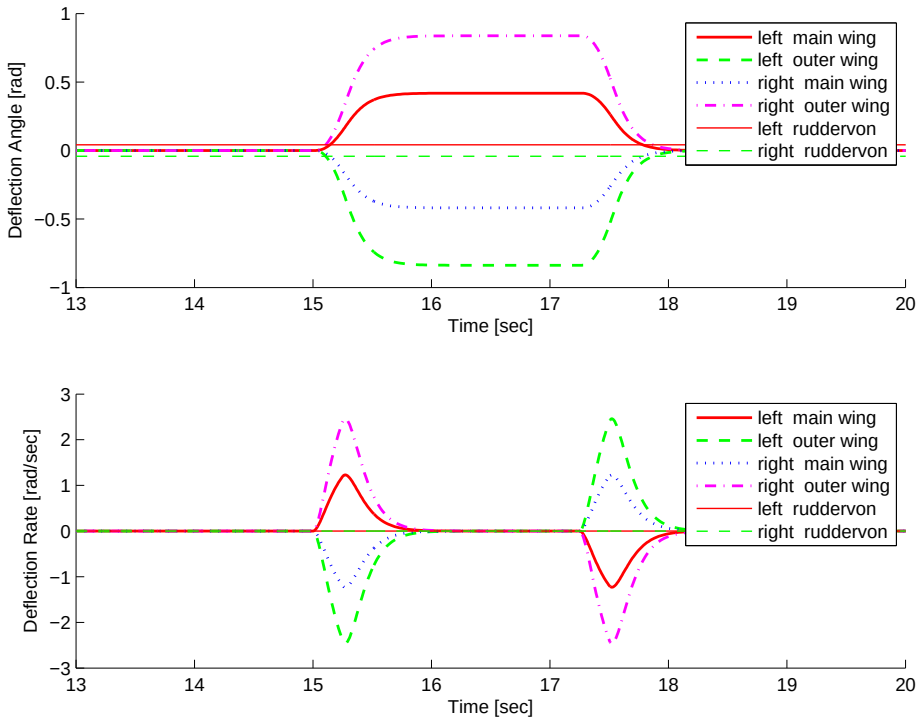

Figure 5.21. Wing angles angles during anti-symmetric morphing.

dips to $\approx -20^\circ$ before the aerodynamic moment takes over and takes the aircraft into a positive roll. As in the case of the asymmetric roll, the morphing moments tend to act only briefly, so that it is generally the aerodynamic moments and forces that determine the overall behavior of the aircraft. Nevertheless, the initial influence of morphing moments is quite significant in this case. Since the initial roll is actually away from the commanded direction, a feedback control system which monitors the body frame roll would have to take this "anomalous" motion into account. Finally, the morphing forces during the anti-symmetric turn are identically 0 due to anti-symmetry; there is no intra-body-frame motion of the CM, and the expressions in Eqs. (4.15) through (4.17) vanish identically.

As can be expected from the behavior of the aerodynamic and morphing moments, the anti-symmetric turning maneuver is somewhat complex. Due to the mor-

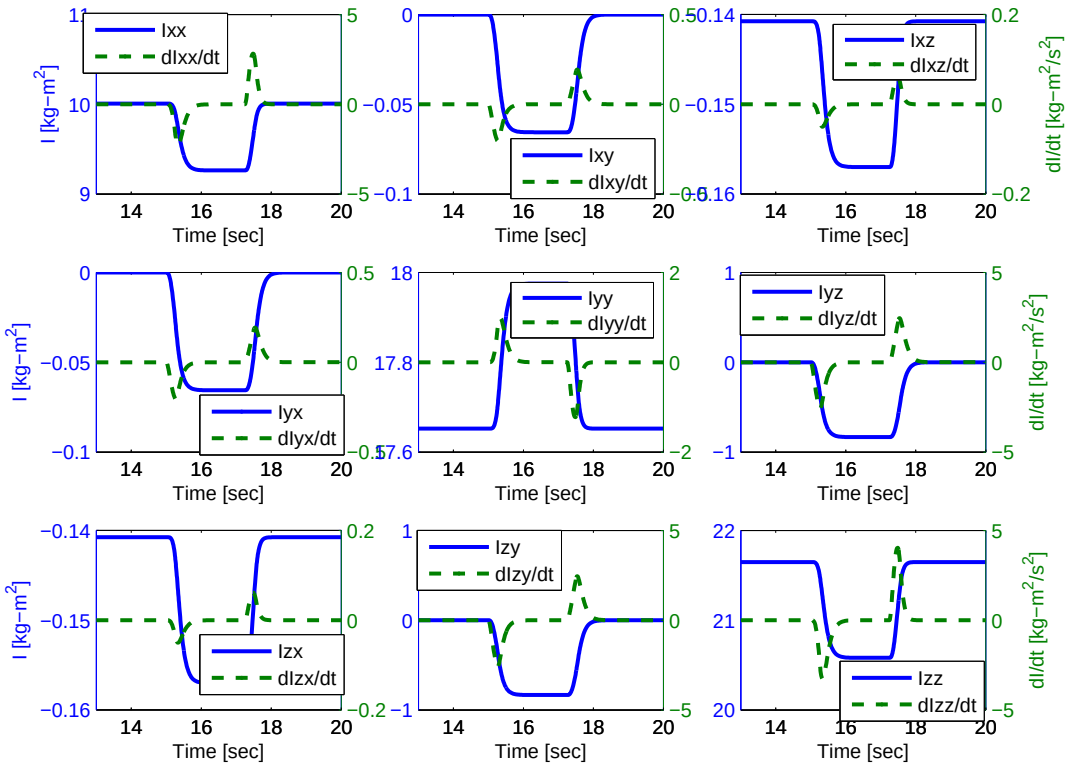

Figure 5.22. Inertia tensor during the morphing part of the trajectory.

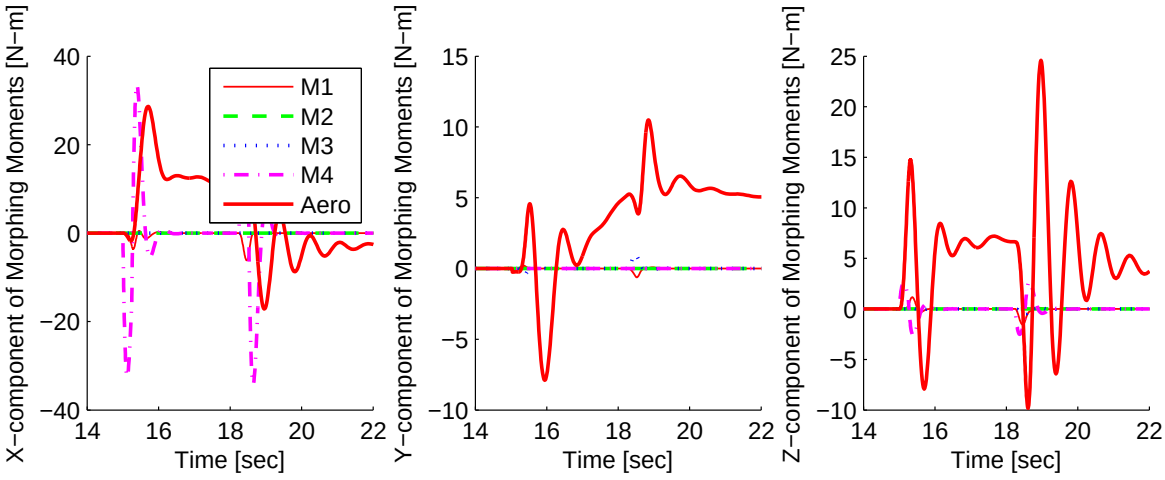

Figure 5.23. Aerodynamic and morphing moments in anti-symmetric turn.

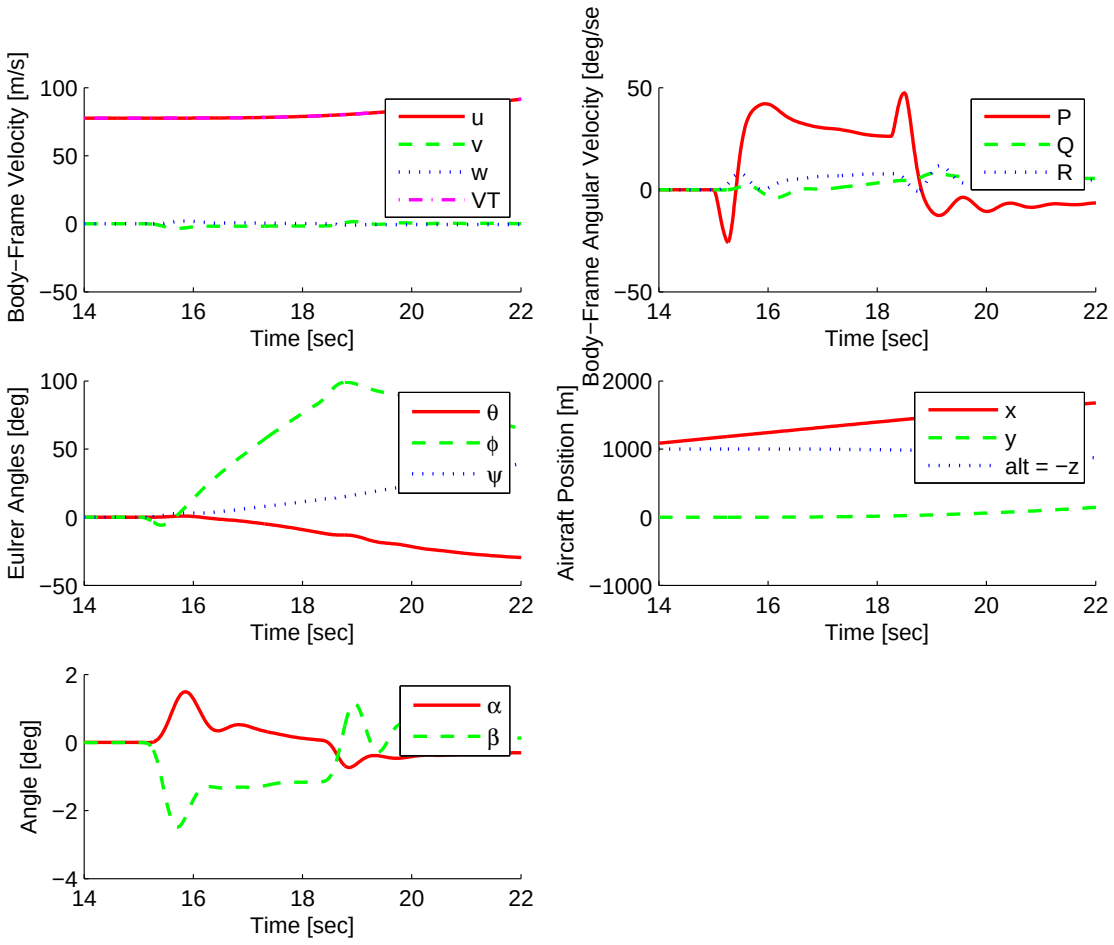

Figure 5.24. State variables of the aircraft during the anti-symmetric turn.

phing moment M_4, the initial roll is indeed away from the desired turn direction, rolling to the left by more than 10°. As the wings approach the anti-symmetric configuration and begin to slow down, the M_4 moment becomes aligned with the aerodynamic moment, sharply rolling the aircraft to the right. This results in a $\approx 90°$ turn to the right.

At the same time, the aerodynamic yaw moment is turning the nose of the aircraft to the right, inducing a negative sideslip. Some oscillation in the sideslip ensues, resulting from the balance of the positive wing yaw moment and negative tail yaw. Finally, as the morphing maneuver ends and the wings are restored to the flat

configuration, the aircraft returns to nearly level flight, having completed a $\approx 90°$ turn.

5.3.3 Dynamic Loads and Power

As in the case of the asymmetric turn, the dynamic actuator moments for the anti-symmetric turn are analyzed in three epochs: just prior to morphing, during morphing, and post-morphing. The complete history of actuator moments for all epochs is shown in Fig. 5.26, while a close-up of the morphing epoch is illustrated in Fig. 5.25. As described in section 4.3, the required actuator power can be computed. As expected, all actuators contribute, since all actuators are involved in morphing. This is illustrated in Fig. 5.27.

As is to be expected, the power required by the various wing actuators is symmetric (or rather, anti-symmetric). During the latter part of morphing, where the wings are restored to the flat configuration, the required joint moments are somewhat reduced. This is simply due to the fact that the aerodynamic load is reduced during this part of the trajectory, as seen in Fig. 5.25. It is interesting to note the finite (and significant) value of the CM-related moments. The CM-related moments are present in spite of the fact that the CM does not actually shift during the anti-symmetric maneuver. As previously noted, the Q_{CM} moments are purely inertial in nature and do not depend on morphing directly. The geometrical derivatives $\left(\frac{\partial \Delta r_{CM}}{\partial q_i}\right)$ on which both Q_{CM} and $Q_{CM-Rate}$ depend are simply sensitivity coefficients which determine how strongly virtual displacements in the q_i variable couple into virtual motion of the CM. As in the case of the asymmetric turn, the Q_{CM} moments during the non-morphing portion of the trajectory are positive, indicating that inertial forces are bending the wing downward (out of the turn), in opposition to the aerodynamic loading.

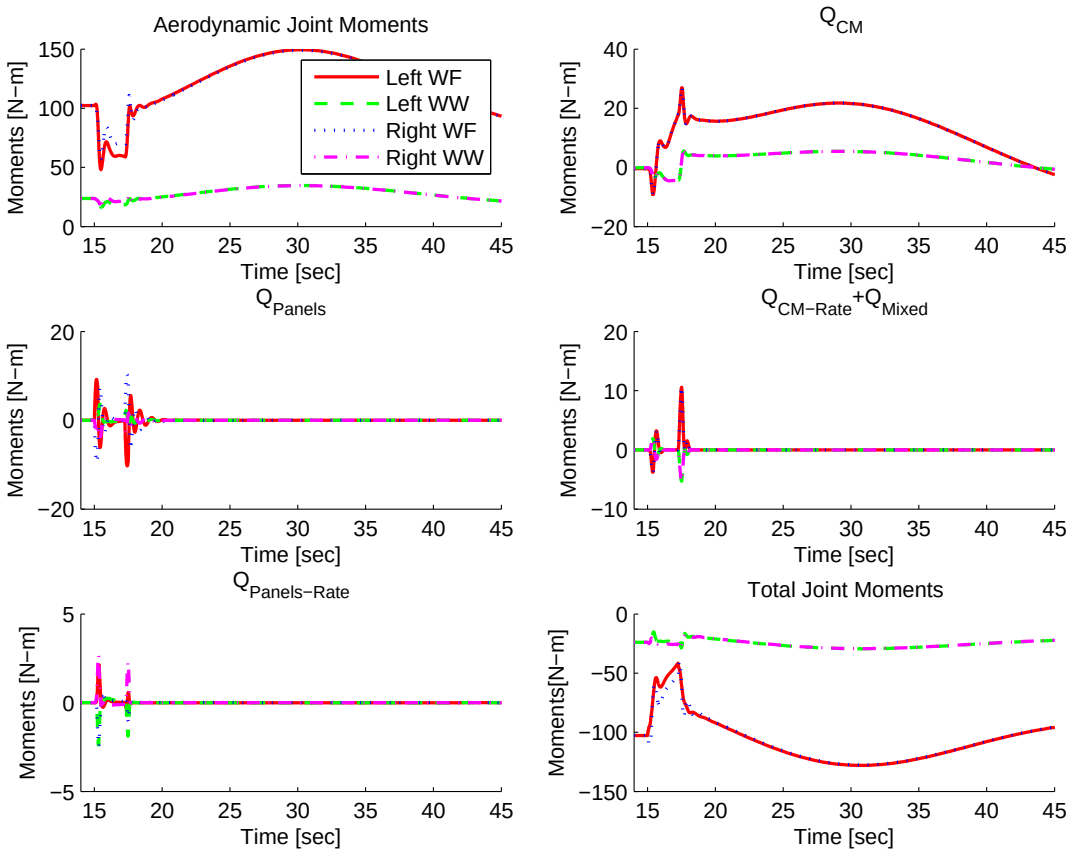

Figure 5.25. Full set of actuator moments for all three epochs .

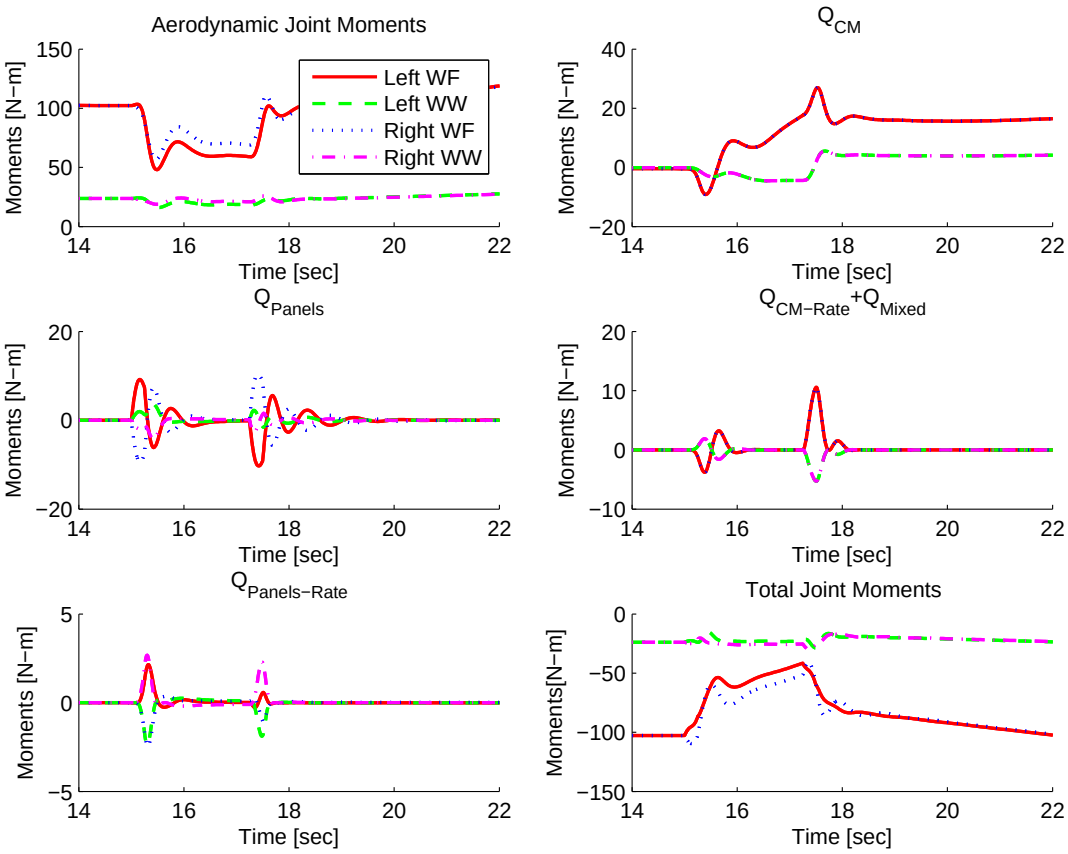

Figure 5.26. Full set of actuator moments is shown for the morphing epoch.

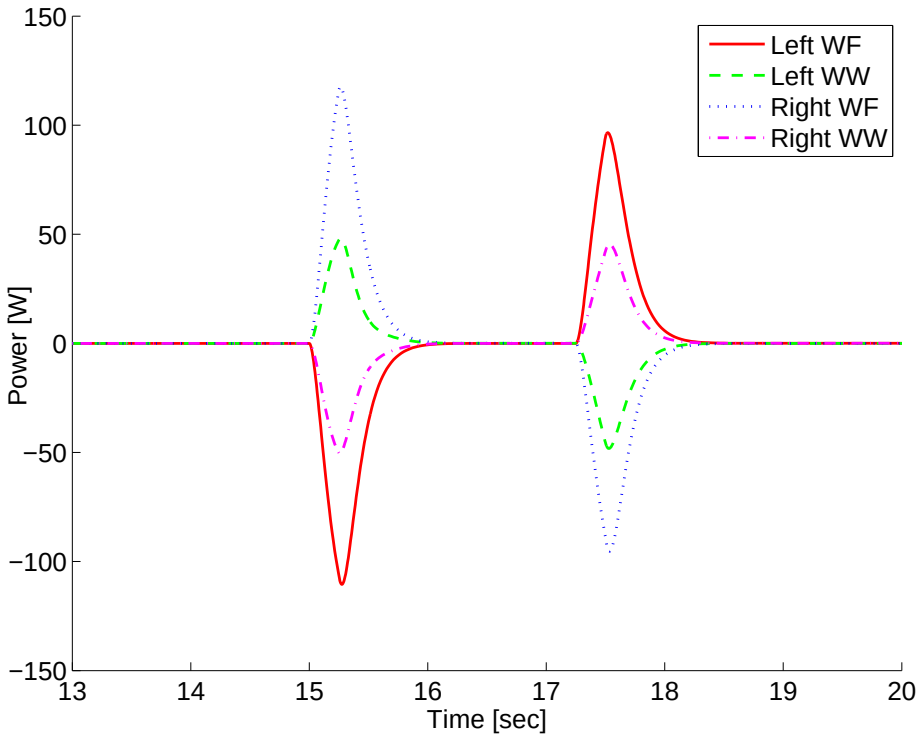

Figure 5.27. Required power for the morphing actuators during morphing.

CHAPTER 6

CONCLUSIONS AND FUTURE WORK

6.1 Summary and Conclusions

A versatile software framework for simulation of morphing aircraft has been developed. The framwork consists of a MATLAB class library and a compiled C++ MEX-library, for best balance of of flexibility and CPU efficiency. The core provided capabilities are:

1. **Aircraft structure generation from a set of planforms and non-planform masses.** Creating a new aircraft requires deriving a new class from the Aircraft base class and providing the constructor function, which defines the planforms and actuators of which the aircraft is comprised.
2. **Vortex Lattice-based aerodynamic calculation of forces and moments.** Aerodynamics of complex morphing aircraft can be accurately computed within limits of the Vortex-Lattice method ($M < 0.5$,$Re > 10000$,$\alpha < 10°$).
3. **Morphing structure flight dynamics, using the Extended Rigid Body approach.** A set of equations of motion for morphing aircraft has been developed, accounting for the intra-body-frame motion of mass during morphing. Compared to the standard Newton-Euler equations, Extended Rigid Body equations feature four additional moments and four additional forces. The forces and moments depend on the velocity and acceleration of the CM in the body frame, the time dependence of the inertia tensor, and the velocity and acceleration of distributed mass elements in the body frame.

4. **Adaptive time-step integration of the non-linear EOM is provided using a Runge-Kutta-Merson solver.**
5. **The actuator moments and power are computed, accounting for aerodynamic, inertial, and morphing loads.**
6. **A Trim-solver is provided, facilitating the computation of user-defined trim points.** Additionally, a Linearizer is also available, computing the A,B,C, and D matrices of the linearized system. Numerical differentiation is used, and no user input is required.
7. **The front-end, time-integration, and aircraft definition are all handled in MATLAB.** This makes it straightforward for users to create new aircraft types or add equations for control systems or observers.
8. **The CPU times are kept to reasonable values by careful choice of numerical algorithms.** Generally, full non-linear flight simulation takes place in better than real time on a 3.06 GHz Quad-Core CPU.
9. **The flight simulation core library is architected to require no modifications if new aircraft, controllers, observers, input or output functions are added.** Each new component is created as a derived class; a base class in the core with the requried interface is provided.

The above-listed features should be compared with the goals and requirements enumerated in section 2.1. Although all the stated goals have been met, significant work remains for future development.

6.2 Future Work

Future work for the morphing aircraft simulation framework is two-fold: extensions of core capabilities and specific applications. At present, the following are envisioned:

6.2.1 Extensions of Core Capabilities

1. **Multi-body dynamics**. The extended rigid body dynamics currently employed can be replaced by an implementation of full Multi-Body Dynamics, such as the Constrained Dynamics approach of [5], or the embedded approach of [6]. From a software standpoint, this would entail creating a new class (derived from the Model class) for the Aircraft EOM. It could exist in parallel with the Extended Rigid Body EOM, and the driver script would simply invoke the class of choice. Thus, all the machinery of the current approach is retained, including the Vortex-Lattice aerodynamics, the aircraft definition, ODE integration algorithm, as well as post-processing. The advantage of the Multi-Body Dynamics approach is that actuator dynamics could be handled more realistically. Furthermore (and more importantly), structural properties of the aircraft would be simulated explicitly. This is not possible with the current approach (although it is possible to deduce the dynamic loads).
2. **Non-quasi-static vortex wake**. The Vortex-Lattice aerodynamics employed support non-quasi-static effects of local freestream velocity, but the vortex wake is treated quasi-statically. This results in significant savings in CPU time, but it also places a limitation on morphing / rotation rate. For small aircraft with fast actuators, removing this restriction could be significant.
3. **Inclusion of viscous effects on aerodynamics**. Since one of the interesting applications of morphing-wing dynamics is in the area of micro-UAVs, the

low-speed, high Reynolds number regime should be comprehended. Standard Vortex-Lattice implementations (including the implementation in this work) handle laminar, non-separated flow only. The VLM would therefore have to be enhanced to be suitable for micro-UAVs.

6.2.2 Applications

1. **Various wing morphing schemes**. The wing morphing scheme considered in this work is the wing folding of the gull-wing aircraft. However, many other schemes are possible, and these would not require modifications or enhancements of the code. Other morphing schemes of interest include telescoping and "stretching" wings [1]. Additionally, "Batwings" [4] could also be simulated with no additional code development. An interesting feature of all the wing types listed is that their morphing consumes significantly less energy than that of gull-wings, since their motion is largely perpendicular to aerodynamic loads. Thus, they may actually present better candidates for morphing-induced maneuvering. Each aircraft type could be equipped with a simple LQR-based turn controller, penalized by the actuator power during the turn. This would facilitate a direct comparison of the turn characteristics for the different morphing configurations.
2. **Non-linear control system using morphing**. Wing morphing introduces non-linear dynamics even for relatively small actuator displacements. Thus, it may be prudent to design non-linear controllers, even if the intended application does not involve large-scale morphing. Furthermore, it may be possible to design non-linear controllers which exploit the non-linearities induced by morphing, as opposed to trying to remove them.

REFERENCES

[1] Weisshaar, T., "Morphing Aircraft Technology - New Shapes for Aircraft Design," *Unclassified NATO report RTO-MP-AVT-141*, 2006.

[2] J.B. Davidson, P. Chwalowski, B. L., "Flight Dynamic Simulation Assessment of a Morphable Hyper-Elliptic Cambered Span Winged Configuration," *AIAA-2003-5301*, August 2003.

[3] J. Bowman, B. Sanders, T. W., "Evaluating the Impact of Morphing Technologies on Aircraft Performance," *AIAA-2002-1631*, 2002.

[4] J. Manzo, E. G., "Evolutionary Flight and Enabling Smart Actuator Devices," *Active and Passive Smart Structures and Integrated Systems 2007, SPIE*, 2007.

[5] Shabana, A. A., *Dynamics of Multibody Systems*, Cambridge University Press, New York, NY 10011-4211, USA, 3rd ed., 2005.

[6] Wittenburg, J., *Dynamics of Multibody Systems*, Springer Verlag, 2nd ed., 2002.

[7] J. Katz, A. P., *Low-Speed Aerodynamics*, Cambridge University Press, New York, NY 1011-4211, USA, 2nd ed., 2001.

[8] D. Grant, A. Chakravarthy, R. L., "Modal Interpretation of Time-Varying Eigenvectors of Morphing Aircraft," *AIAA Atmospheric Flight Mechanics Conference*, August 2003.

[9] D. Grant, R. L., "Effects of Time-Varying Inertias on Flight Dynamics of an Asymmetric Variable-Sweep Morphing Aircraft," *AIAA Atmospheric Flight Mechanics Conference and Exhibit*, August 2007.

[10] D. Grant, M. Abdulrahim, R. L., "Flight Dynamics of a Morphing Aircraft Utilizing Independent Multiple-Joint Wing Sweep," *AIAA Atmospheric Flight Mechanics Conference and Exhibit*, August 2006.

[11] A. Chakravarthy, D. Grant, R. L., "Time-Varyinhg Dynamics of a Micro Air Vehicle with Variable-Sweep Morphing," *AIAA Guidance, Navigation, and Control Conference*, August 2009.

[12] T. Yue, L. W., "Multibody Dynamic Modeling and Simulation of a Tailless Folding Wing Morphing Aircraft," *AIAA Atmospheric Flight Mechanics Conference*, August 2009.

[13] J. Valasek, A. Lampton, M. M., "Morphing Unmanned Air Vehicle Intelligent Shape and Flight Control," *AIAA Infotech@Aerospace Conference, Seattle, Washington*, April 2009.

[14] J. N. Scarlett, R. A. Canfield, B. S., "Multibody Dynamic Aeroelastic Simulation of a Folding Wing Aircraft," *47th AIAA/ASME/ASCE/AHS/ASC Structures, Structural Dynamics, and Materials Conference*, May 2006.

[15] M. Blundell, D. H., *Multi-Body Systems Approach to Vehicle Dynamics*, Butterworth-Heinemann, 2004.

[16] C. J. Sequeira, D. Willis, J. P., "Comparing Aerodynamic Models for Numerical Simulation of Dynamics and Control of Aircraft," *AIAA Aerospace Sciences Meeting, AIAA-2006-1254*, 2006.

[17] Melin, T., *Tornado, a Vortex Lattice MATLAB Implementation for Linear Aerodynamic Wing Applications*, Master's thesis, Royal Institute of Technology (KTH), Sweden, 2000.

[18] E. Selitrnnik, M. K., "Generalized Approach to Aeroelastic CFD Time Simulations of Morphing Flight Vehicles," *50th AIAA/ASME/ASCE/AHS/ASC Structures, Structural Dynamics, and Materials Conference*, May 2009.

[19] H. Namgoong, W. A. Crossley, A. S. L., "Morphing Airfoild Design for Minimum Aerodynamic Drag and Actuation Energy Including Aerodynamic Work," *47ths AIAA/ASME/ACSE/AHS/ASC Structures, Structural Dynamics, and Materials Conference*, May 2006.

[20] D. Coutu, V. Brailovski, P. T., "Promising Benefits of an Active-Extrados Morphing Laminar Wing," *Engineering Notes, Journal of Aircraft*, Vol. 46, No. 2, March 2009.

[21] B. L. Stevens, F. L. L., *Aircraft Control and Simulation*, John Wiley and Sons, 2nd ed., 2003.

[22] T. R. Yechout, S. L. M., *Introduction to Aircraft Flight Mechanics: Performance, Static Stability, Dynamic Stability, and Classical Feedback Control*, AIAA Education Series, 2003.

[23] J.J. Bertin, M. S., *Aerodynamics for Engineers*, Prentice-Hall, Inc, Englewood Cliffs, New Jersey 07632, 1979.

[24] J. Weber, G. G. B., "Low-Speed Tests on 45-deg Swept-Back Wings, Part I. Pressure Measurements on Wings of Aspect Ratio 5," *Reports and Memoranda, Aeronautica Research Council*, 1958.

[25] Sivells, J. C., "Experimental and Calculated Characteristics of Three Wings of NACA 64-210 and 65-210 Airfoil Sections with and without Washout," *Technical Note 1422, NACA*, August 1947.

[26] Goldstein, H., *Classical Mechanics*, Addison Wesley, New York, NY, 2001.

[27] Merson, R. H., "An operational method for the study of integration processes," *Proc. Symp. Data Processing, Weapons Res. Establ. Salisbury*, 1957.

BIOGRAPHICAL STATEMENT

Borna Obradovic was born in Zagreb, Croatia, in 1970. He holds a B.Sc. in Physics, MS and Ph.D. degrees in Electrical Engineering from the University of Texas at Austin. He has worked in the area of modeling and simulation of processes, devices and system at Intel Corp. and Texas Instruments. He holds 14 patents in the area of process and device modeling.